Università degli Studi di Parma

DIPARTIMENTO DI DI SCIENZE MATEMATICHE FISICHE E INFORMATICHE

Corso di Laurea Magistrale in Fisica

Tesi di laurea magistrale

Turbulence Large Eddy Simulations in Abdominal Aortic Aneurysm

In collaborazione con
MOX, Dipartimento di Matematica "F. Brioschi",
Politecnico di Milano

Laureando:
Roberto PIERSANTI
Matricola 270433

Relatori Esterni:
Prof. Luca DEDÉ (MOX)
Prof. Lorenzo VALDETTARO (MOX)
Prof. Christian VERGARA (MOX)

Relatori Interni:
Prof.ssa Alessandra AIMI (UNIPR)
Prof.ssa Laura ROMANÓ (UNIPR)

Correlatore:
Dott. Simone STELLA(MOX)

Anno Accademico 2016–2017

Alla mia famiglia:
A coloro che sono stati (i miei nonni),
A coloro che sono (i miei genitori e mio fratello),
A coloro che saranno (la piccola Daphne, ...).

Abstract

Standard studies of the cardiovascular system are based on advanced experimental and imaging techniques. However, in the past few years, they are being complemented by computational fluid dynamics (CFD) simulations of blood flows with increasing level of details. Clinical measures as well as CFD studies revealed that the effects of transition to turbulence in abdominal aortic aneurysms (AAA) is related to the heart pulsatility and sudden change of diameter of the vessels.

In this thesis, we study the blood fluid dynamics using CFD simulations in which we discretized the Navier-Stokes equations by means of the Finite Element method in combination with different type of LES σ-models (static and dynamic) to accurately describe transition to turbulence in a realistic scenarios of AAA. We provide a reference numerical solution obtained at high resolution without any subgrid scale model, to be used to assess the accuracy of LES simulations. We post-process the obtained numerical solutions to assess hemodynamic significant quantities, such as the time average wall shear stress, and vortical structures educed via the so-called *Q-criterion*. Furthermore, a complete SUPG-PSPG stabilization technique procedure has been implemented in `LIFEV` C++ library.

The results demonstrate the suitability of the considered LES σ-models and show the presence of significant turbulence transitional effects inside the aneurysmatic sac during the mid-deceleration and diastolic phases.

Keywords : Computational Fluid Dynamics, CFD, Finite Element Method, FEM, Large Eddy Simulations, LES, Sigma Model, Abdominal Aortic Aneurysms, AAA, Hemodynamics, SUPG-PSPG, LIFEV

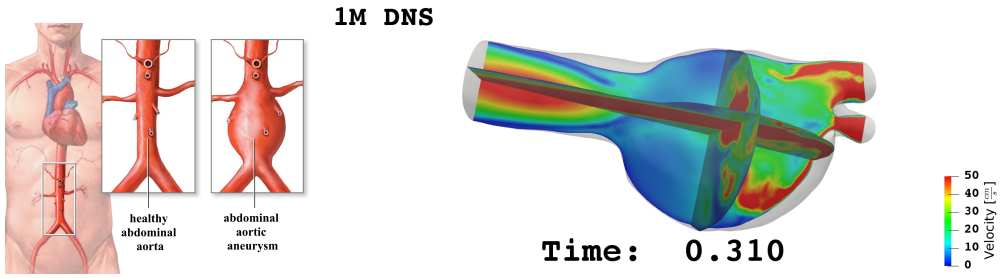

(a) AAA. (b) DNS.

Figure 0.1: (a) rappresentazione schematica dell'Aneurisma Addominale Aortico (AAA); (b) un istante della simulazione DNS.

Estratto in lingua italiana

Gli strumenti di indagine più usati per studiare il sistema cardiovascolare sono basati su avanzate tecniche di imaging. Soltanto negl'ultimi anni queste tecniche strumentali sono state affiancate da simulazioni di fluido dinamica computazionale (CFD) riguardanti il flusso del sangue nelle vene/arterie. Misure cliniche e studi di CFD hanno rivelato che la presenza di effetti di transizione alla turbolenza, nella patologia dell'Aneurisma Addominale Aortico (AAA), è legata al cambiamento improvviso del diametro dell'aorta e al fatto che il flusso del sangue nelle vene è pulsato (vedi Figura 0.1a).

In questa tesi abbiamo studiato la fluidodinamica del sangue in uno scenario reale di AAA, usando simulazioni di CFD per descrivere in modo accurato gli effetti di transizioni alla turbolenza in questa patologia. In particolare, si sono discretizzate le equazioni di Navier-Stokes con il metodo degli Elementi Finiti in combinazione con differenti modelli di turbolenza LES (Large Eddy Simulation) σ-models (statico e dinamico). Per poter stimare l'accuratezza delle diverse simulazioni LES, abbiamo costruito una soluzione numerica di riferimento, chiamata DNS (Direct Numerical Simulation), ottenuta con una griglia ad alta risoluzione e senza nessun modello di turbolenza (vedi Figura 0.1b). Le differenze principali tra le simulazioni LES e la DNS sono ben visibili intorno al picco diastolico. Queste discrepanze sono dovute a effetti di transizione che abbiamo ritrovato essere inglobati nella viscosità turbolenta caratteristica dei modelli di turbolenza σ-LES.

Le simulazioni σ-LES, statiche e dinamiche, mostrano caratteristiche molto simili in ogni quantità che abbiamo misurato (come il campo di velocità e di vorticità). Alcune differenze, rivelate intorno al picco diastolico, sono probabilmente dovute anche al fatto che il modello dinamico, a differenza del modello statico, riesce a riprodurre il fenomeno della cosiddetta Cascata In-

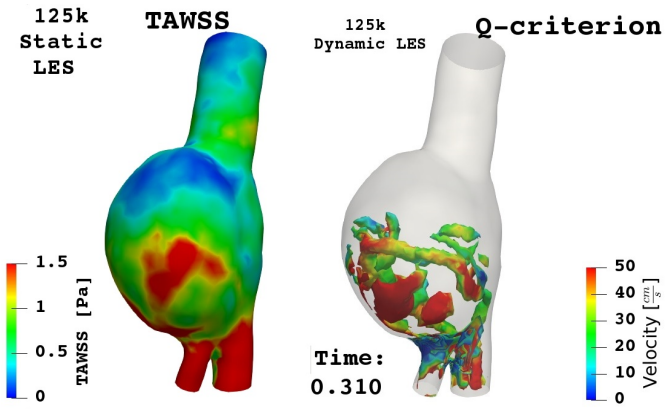

(a) TAWSS. (b) *Q-criterion*.

Figure 0.2: (a) stress a parete medio (TAWSS) nella simulazione σ-statica; (b) *Q-criterion* nella simulazione σ-dinamica.

versa (Backscatter). Di fatto, nella simulazione dinamica la percentuale di Backscatter misurata è circa il 45%.

Gli effetti di transizione alla turbolenza sono stati messi in luce misurando le media di insieme del campo di velocità, l'energia cinetica globale e lo stress a parete medio (TAWSS, Time Average Wall Shear Stress), vedi Figura (0.2a). Inoltre, abbiamo individuato nelle simulazioni numeriche le strutture vorticose tipiche della turbolenza tramite il *Q-criterion* (vedi Figura 0.2b).

Abbiamo analizzato quando e dove è presente la viscosità turbolenta del modello σ-LES all'interno della sacca aneurismatica, misurando il rapporto tra la viscosità turbolenta e quella molecolare. Da quest'ultima analisi si evince che i modelli di turbolenza σ-LES sono attivi soprattutto durante la fase di metà decelerazione e intorno al picco diastolico.

Infine, abbiamo condotto un'analisi per il modello σ-statico raffinando la griglia di calcolo in una geometria artificiale di AAA appositamente costruita. Si è osservato che il rapporto tra viscosità turbolenta e molecolare è più grande per griglie più lasche, mentre invece risulta più piccolo per mesh più fini.

Durante il lavoro di tesi si è implementata la procedura di stabilizzazione SUPG-PSPG fortemente consistente, nella libreria LIFEV C++. Questa nuova versione di SUPG-PSPG mostra meno dissipazione numerica rispetto alla versione precedente. Tutte le simulazioni numeriche sopracitate fanno uso di questa nuova versione di SUPG-PSPG.

I risultati hanno dimostrato che i modelli di turbolenza σ-LES sono adatti a descrivere gli effetti di transizione alla turbolenza nella patologia dell'AAA

Contents

Introduction

Mathematical and numerical modeling of the cardiovascular system is a research topic that has attracted a remarkable interest from the mathematical community. The driving motivation for such interest is the increasing impact of cardiovascular diseases (CVD) in our lives. According to [95], CVD are the major cause of death worldwide, leading to more than 17 million deaths per year, a number that is expected to grow to more than 23 million by 2030. In Europe, nowadays they correspond to nearly half of all deaths (47%).

There are many risk factors associated with CVD, like age, genetic factors, high blood pressure, high cholesterol, obesity, diabetes, cigarette smoking, high alcohol consumption, etc [96, 88].

In this thesis we focused on a specific category of these pathologies: the Abdominal Aortic Aneurysm (AAA). Aneurysms are localized permanent arterial dilatations due to disease or other complex processes that result in the weakening of the arterial walls [88]. Although this complex vascular disease forms in many blood vessels, it mainly appears in arteries, primarily in the abdominal and thoracic portions of the aorta. Among these, fusiform aneurysms[1] are most commonly found in the abdominal portion of the aorta, below the renal arteries and upstream of its bifurcation into the iliac arteries. These are known as Abdominal Aortic Aneurysms (see Figure 0.3).

Smoking is the risk factor most strongly associated with AAA, followed by age, hypertension, and atherosclerosis [98]. Sex and genetics also influence aneurysm formation [97].

Several diagnostic imaging modalities are now available for detecting and monitoring AAAs. Among these, there are computed tomography (CT) scanning, magnetic resonance (MR) angiography. The disadvantages of using this clinical technique are related to their cost and the use of ionizing radiation and intravenous contrast media.

A localized aortic dilatation is clinically considered an aneurysm when its maximal diameter is greater than 1.5 times the healthy diameter [87]. It

[1] Aneurysms are often classified according to their shape. Fusiform aneurysms are characterised by a bulge about the vessel centerline.

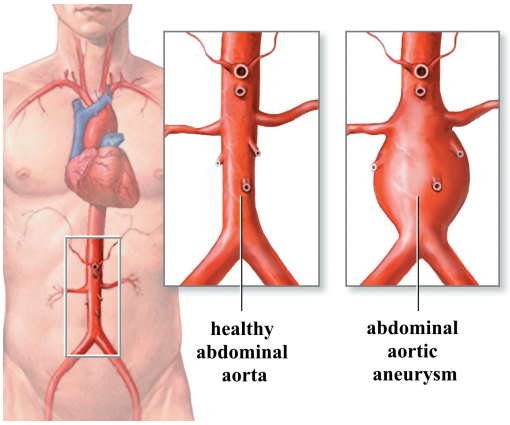

Figure 0.3: Simple representation of an abdominal aortic aneurysm (picture taken from *www.njveinandlasercenter.com*).

is important to note that generally only the maximum diameter is used as a criterion for risk of rupture associated with an AAA. The length (or the width) of an AAA, which is indicative of the size, is not taken into account.

The risk of complications resulting from surgery (in particular for old people) are very high. This characteristic imposes an accurate assessment of the risks versus benefits of an operation. Indeed, the various interventions to treat this pathology are put in place only when the estimation of the risk of aneurysm rupture exceed the risks associated with postoperative complications.

Clinical studies have underlined that fluid dynamics plays an important role in the determination of the causes of degradation and consequent deformation and weakening of the arterial wall. To determine the risk of rupture, the evaluation of how the effects of fluid dynamic phenomena affect the aortic wall is necessary.

For this purpose, in recent years there was a growing interest in developing mathematical and computational models applied to the cardiovascular system, mainly motivated by the fact that these computational models are less invasive than in-vivo investigations, often more accurate and flexible than in-vitro experiments and with no ethical and practical limitations. Indeed, the computational blood fluid dynamics could lead to significant advances in prevention, diagnosis, as in the assessment of CVD progression, and therapies, e.g. in surgical planning or in optimizing medical devices.

In this thesis we focus on the modeling and simulating blood flow dynamics on AAA, using clinical data on blood velocity and medical images provided by the Vascular Surgery Division, I.R.C.C.S. Ca' Granda Ospedale Maggiore, Policlinico di Milano, Italy.

Blood flow is normally laminar in healthy vascular vessels. A different situation occurs in pathological districts, where significant transition to turbulence effects could develop, often as a consequence of a change of the geometry (as in AAA). In particular, due to the sudden change of geometric shape and heart pulsatility, turbulence effects in AAA have been observed in-vivo by means of the Echo-Color Doppler (ECD) technique [99]. Also in-vitro experiments in idealized AAA have been set up to study the presence of turbulence [100, 101, 103].

The presence of turbulence effects in AAA carries a significant clinical impact. In the initial phases of AAA development, turbulence interferes with endothelial cells turnover, which is at the basis of atherosclerosis development [13]. In the more advanced stages of AAA development, turbulence produces increased wall shear stresses compared with laminar flows, which may be responsible for further aneurysm dilatation, since the abdominal aorta regulates its diameter to maintain the shear stress below a physiological value [103]. Moreover, the increased shear stresses together with aortic wall vibration due to the large fluctuations, could damage the vessel wall, with possible implications on aneurysm growth and rupture [91].

To date, there are several scientific studies with turbulence models on ideal aneurysm geometries [104, 100, 19], but only few studies on real geometries, especially with Large Eddy Simulation (LES) turbulence models [20].

The aim of this thesis is to asses the reliability of LES σ-models in a specific hemodynamic scenario that is the AAA, where transitional to turbulence should not be neglected. To achieve this result we compared different numerical simulations obtained by these LES models with a Direct Numerical Simulation[2]. This comparison will be done in a real geometry of AAA.

[2]Obtained at high resolution without any turbulence model.

Summary

The remaining part of this thesis is organized as follows:

I *Turbulent flows*: in Chapter 1 we introduce the basic concepts of turbulence, and we document the presence of turbulent flows in hemodynamics, focusing our attention on the AAA pathology.

II *Mathematical models*: in Chapter 2 we present the mathematical models used in this thesis. We discuss how we can model the blood flow dynamics and we present the Large Eddy Simulation turbulence models used in this work: the σ-models (static and dynamic).

III *Numerical methods*: in Chapter 3 we afford the numerical discretization of the equations with turbulence modeling, described in Chapter 2, using the Finite Element Formulation. We also detail the SUPG-PSPG stabilization related to the Finite Element formulation used.

IV *Pre-processing and meshes building*: in Chapter 4 we describe how we have build the meshes, in a real geometry of AAA, for the LES simulations. We present the method used to estimate the parameters to build a suitable DNS by means of a viscous, linear, incompressible and two-dimensional shear layer stability analysis.

V *Numerical results*: in Chapter 5 we validate the implemented LES framework and we present and discuss numerical results obtained. In particular we compare different LES models in the real geometry of AAA evaluating turbulent quantities and haemodynamic indexes. LES numerical results are also compared with the DNS ones.

Chapter 1

Turbulent flows

Turbulence is ubiquitous in nature and handles a key role in many applications of our life. It is a fact that most fluid flows are turbulent.

Turbulence appears almost everywhere: flows in rivers, oceans, atmosphere, solar wind, and interstellar medium (large scale examples); flows in pipes, pumps, turbines, combustion processes, in the wake of cars, airplanes and trains (some technical examples). Circulatory and respiratory systems show occasionally turbulent flows (carotids, aneurysms, ascending aorta, heart, pulmonary airway), too.

Despite the widespread occurrence of fluid flow, the turbulence remains one of the unsolved problems of classical mathematical physics. Turbulence has been studied by many of the greatest physicists and mathematicians of the 19th and 20th centuries, and yet we do not understand it in complete detail.

1.1 Basic concepts of turbulence

The first issue in dealing with turbulence is to provide an adequate definition. However, a turbulent flow is often characterized by the following features [1]:

- highly random fluctuating velocity both in space and time;
- three-dimensional rotational flow field, with complex vortical structures;
- large mixing capacity (both at large and small scales);
- strongly chaotic flow, very sensible to the initial and boundary conditions.

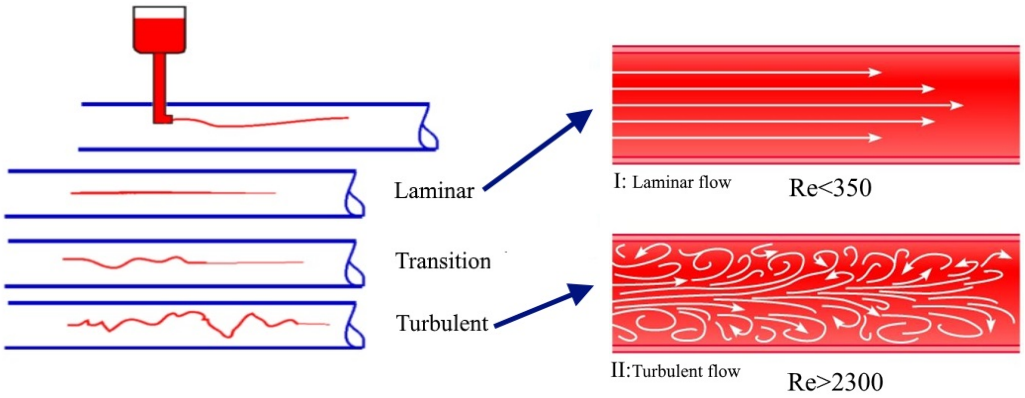

(a) Dyed water flow. (b) Laminar(I) vs Turbulent(II).

Figure 1.1: Transition from laminar to turbulent flow under different velocities using a small stream of dyed water introduced into the center of clear water flow in a larger pipe (pictures taken from *www.green-mechanic.com*).

A fluid that is not turbulent, i.e. such that the velocity varies smoothly in space and time, is known as a laminar flow. At a first level, the state of fluid motion can be described, introducing the dimensionless parameter, called Reynolds number, Re, defined as

$$Re = \frac{UL}{\nu},$$

where U is the flow velocity magnitude, L is the characteristic length, and ν is the fluid kinematic viscosity.

The Reynolds number is a measure of the ratio between the inertial forces, generated by the flow velocity, and the viscous forces of the fluid. Thus, Re can be used to discriminate between laminar and turbulent flow. Namely:

1. for "low" Re, viscous forces dominate and we are in the viscous fluid situation (Laminar Flow),

2. for "high" Re, inertial forces prevail and a slightly viscous fluid with high velocity emerges (Turbulent Flow),

where "high" and "low" depend on the physical situation. For example, in a pipe-flow experiments, for Re less than 350, the flow remain laminar, while for Re greater then ~ 2300, the flow becomes turbulent (Figure 1.1b).

When Re is increasing we have roughly three regimes: Laminar, Transition to Chaos, Turbulence (Figure 1.1a).

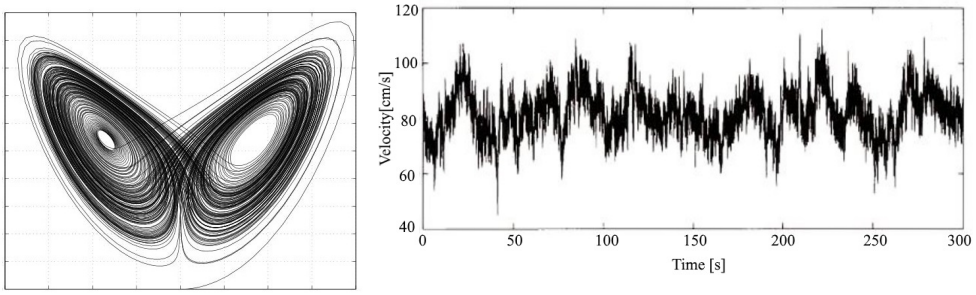

(a) Lorenz attractor (b) Turbulent signal

Figure 1.2: Chaotic features of turbulence (pictures taken from *www.umanot.com*, *www.vtchl.illinois.edu*).

For "low" Re we are in Laminar Regime, where the flow presents a very simple behavior in time and space. As Re increases, a second regime, named Transition to Chaos, may emerge. In this case, the flow begins to oscillate and becomes irregular (in space and time). For a critical Re, a Turbulence regime arises. In that regime the velocity field contains a wide spectrum of spatial and temporal frequencies.

In a turbulent fluid the velocity $\mathbf{u}(\mathbf{x}, t)$ at a fixed point shows random fluctuations with time (Figure 1.2b). On the other hand $\mathbf{u}(\mathbf{x}, t)$ at a fixed time presents random variations with space, too.

In 1960, Lorenz discovered the chaotic behavior of a simplified system of equations describing the two-dimensional flow of fluid (Figure 1.2a). Indeed, turbulence is a chaotic process: a small change in the initial conditions $\mathbf{u}(\mathbf{x}, t = 0)$ results in a large change in its time evolution, $\mathbf{u}(\mathbf{x}, t > 0)$ (Figure 1.2).

Another important feature of turbulence is the presence of irregular eddying motions when the vorticity, defined as

$$\boldsymbol{\omega} = \nabla \times \mathbf{u}$$

is not zero. Usually, a turbulent flow has a spectrum of eddy sizes and contains coherent vortical motions, eddies, which occur at random locations and at different length scales.

A first schematic view of turbulence is the so called Richardson Cascade [2] (due too Lewis Fry Richardson - R.F.L. - 1920). In this picture we can ideally subdivide our complex turbulent flow in "blobs", eddies, that decrease in size from Large Scale (L.S.) to Small Scale (S.S.), see Figure 1.3a. Only at

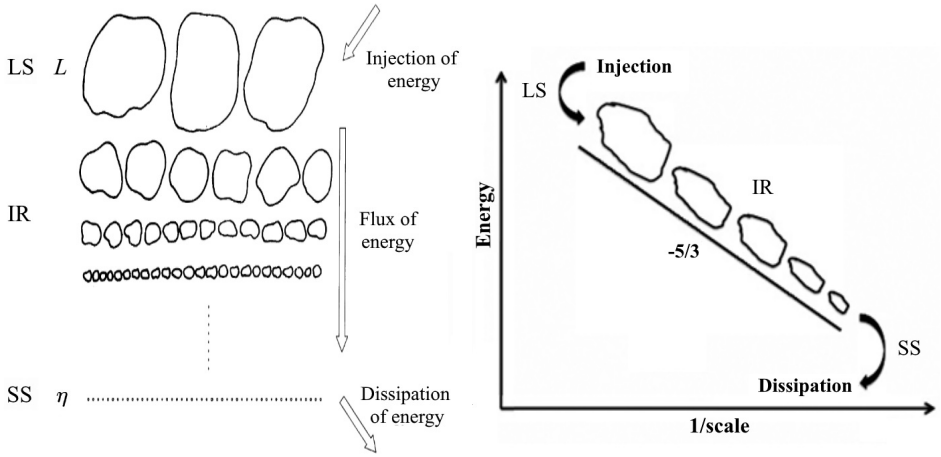

(a) Richardson cascade. (b) Energy cascade.

(c) Cantor Dust

Figure 1.3: (a) Richardson cascade, and (b) its representation as an energy cascade [2]; (c) the famous Cantor dust [80], a fractal that looks very similar to the Richardson cascade [3].

very short scale the viscosity can act and the dissipation (by molecular viscosity) takes place. From this simple picture we can observe how turbulence is a multiscale phenomena.

"Big whirls have little whirls
which feed on their velocity,
and little whirls have lesser whirls
and so on to viscosity."
cit. R.F.L.

In the last thirty years, there have been a lot of work focused on how fractal geometries[1] might be used to descrivbe turbulent flows [3]. Indeed, turbulent flow can be viewed as an ensemble of fractal geometries [4]. Thus, turbulence can be represented as a collection of a number of fractals each of which is slightly different (see, for example, 1.3c).

[1] A fractal is a geometric object with internal homothety: it repeats itself in the same form on different scales.

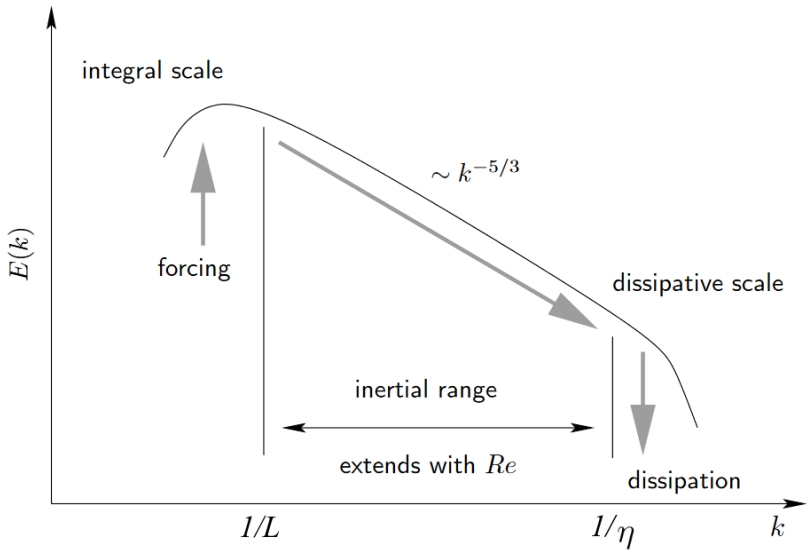

Figure 1.4: K41 energy spectrum, $E(k)$.

A first formal way to describe turbulence has been given by Kolmogorov in 1941 [5], whose theory (named K41) is based on four fundamental hypotheses:

1) the flow is statistically stationary, homogeneous and isotropic[2];

2) the dissipation rate ϵ does not tend to zero when $Re \to \infty$ (there will always be some dissipation due to ν - kinematic viscosity);

3) the existence of three energetic bands in consequence of Richardson Cascade, where two scales are well separated by an intermediate one (Figure 1.3b):

   L.S. the integral scale (the Large Scale region) where the energy is produced. This scale (with a typical scale length indicated by L) is coupled with the mean field,

   I.R. the intermediate scales (the Inertial Region) in which the energy is transferred to the small scales by non-linear interactions and without the action of viscosity or production of energy,

   S.S. the dissipation region (the Small Scale) where the kinetic energy is dissipated by the viscous effects. Furthermore, η is the Kolmogorov length scale which is associated to the smallest dissipative eddies;

[2]Stationary, homogeneous and isotropic flows mean temporal, translational and rotational (in space) symmetry, respectively.

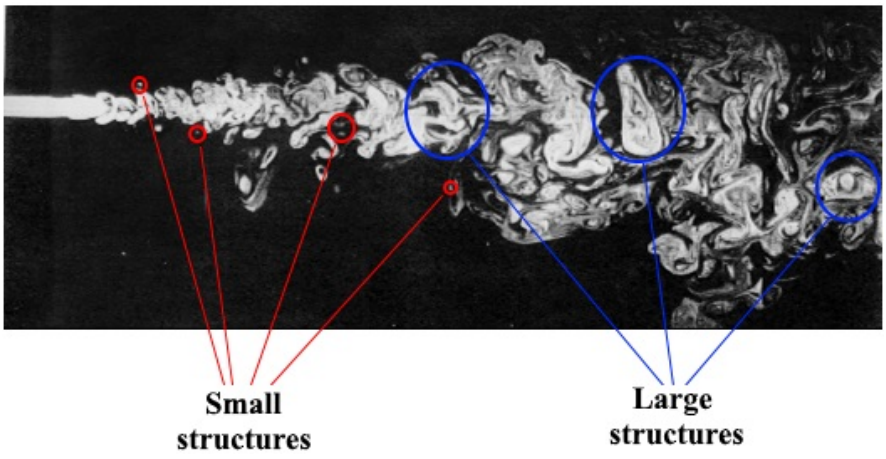

Figure 1.5: Jet of water initially axial symmetric, at $Re = 2300$. Note the loss of stability and the rapid transition to turbulence. We can observe the presence of large and small eddies [4].

4) All the statistical quantities depend on the dissipation rate, ϵ, on the kinematic viscosity, ν, and on the separation distance between two points in the flow field, r (or k, if we are dealing with a quantity described in the Fourier space[3]). Moreover, for sufficiently large scale the statistical moments do not depend on ν.

Using these hypothesies we can derive one of the most important features of K41: the kinetic energy, E, is transferred from large scales of motion to the smaller ones (direct energy cascade, as shown in Figure 1.4):

$$E(\epsilon, k) \sim k^{-\frac{5}{3}} \epsilon^{\frac{2}{3}}.$$

As a result of K41 theory, the separation between L.S. and S.S. (see, for example, Figure 1.5) is

$$\frac{L}{\eta} \sim O(Re^{\frac{3}{4}}). \tag{1.1}$$

The fundamental flaw in Kolmogorov's theory lies in the fact that a turbulent signal is intermittent ([4]). For example, the phenomena called Backscatter, in which energy goes form small scales to larger scales (inverse cascade of energy), was not mentioned in K41 and was discovered later on, observing that a turbulent signal is an intermittent one ([4]).

[3]In the Fourier space the variable r is replaced by $k \sim \frac{1}{r}$, as in the kinetic energy $E(k, \epsilon)$.

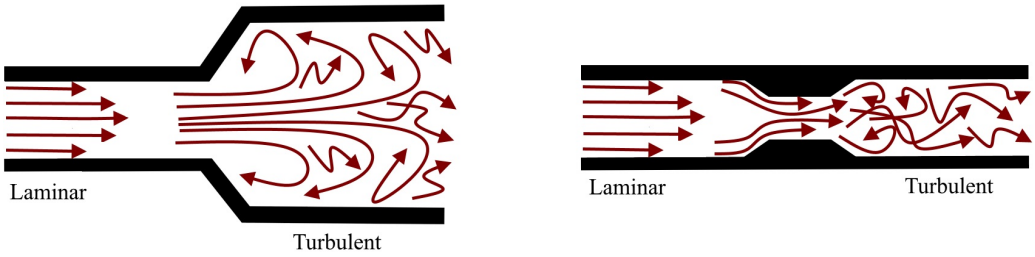

Figure 1.6: Simplified schematization of aneurysm (on the left) and of stenosis (on the right).

1.2 Turbulence in Hemodynamics

The study of blood flow is called Hemodynamics. In the human cardiovascular system the blood flow is usually laminar. Nonetheless, in [12] it has been investigated the turbulence of blood flow in glass models, which simulated arterial bifurcations and the carotid siphon. The critical Reynold's numbers for these models were found to be considerably below the generally accepted value of pipe-flow critical value, $Re \sim 2300$.

Some cardiovascular districts in pathological conditions are characterized by complex geometries (bends, stenosis, bifurcations, aneurysm or areas with an abrupt increase in diameter) and high blood velocity (see Figure 1.6). These two characteristics, combined with the heart flow pulsatility, can generate high frequency velocity fluctuations within the blood flow, leading to a transitional or turbulent flow field [12].

During this transitional state, blood flow does not exhibit the typical inertial range scales of fully developed turbulent flow. This means that the blood flow should be named as highly unsteady or chaotic flow in some cases but not strictly turbulent at all (surely not an isotropic, homogeneous, stationary turbulence).

Turbulence can significantly alter the effect that the fluid has on the arterial walls, modifying hemodynamic indexes such as Wall Shear Stress. A turbulent flow is also considered to be more damaging to endothelial cells[4] than laminar flows [13, 14]. Moreover, turbulence increases the energy required to drive blood flow since it develops friction. This means an increase of the perfusion pressure[5] required to drive a given flow (see Figure 1.7).

[4]Endothelium refers to cells that line the interior surface of blood vessels. Endothelial cells are involved in many aspects of vascular biology, including blood clotting, formation of new blood vessels, vasoconstriction, and vasodilation (hence, the control of blood pressure).

[5]The resistance to flow, R, offered by the blood vessel and its interactions with the flowing blood, is related to the pressure difference, ΔP (sometimes called driving pressure

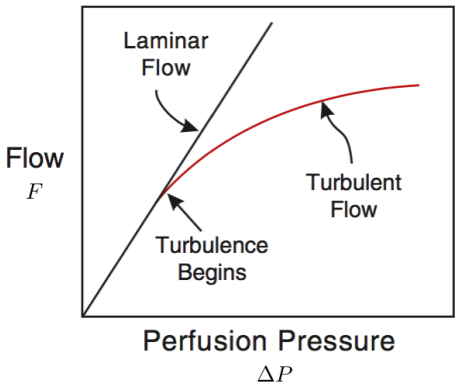

Figure 1.7: Pressure-flow relationship ($F = \frac{\Delta P}{R}$.): turbulence increases the perfusion pressure required to drive a given flow. Alternatively, at a given perfusion pressure, turbulence leads to a decrease in flow (picture taken from *www.cvphysiology.com*).

Turbulence generates sound waves (e.g., ejection murmurs, carotid bruits) that can be heard with a stethoscope. Because higher velocities enhance turbulence, murmurs intensify as flow increases. Elevated cardiac outputs, even across anatomically normal aortic valves, can cause physiological murmurs because of turbulence. Recent studies have investigated transition to turbulence in presence of pathologic conditions

- atherosclerotic carotids [15, 16, 17], (Figure 1.8),
- aneurysms [18, 19, 20], (Figure 1.10),
- hemodialysis treatment [21, 22],

but also in healthy conditions

- ascending aorta [23, 24], (Figure 1.9a),
- left ventricle [25, 26], (Figure 1.9b),
- pulmonary airway [27], (Figure 1.9c).

To understand how blood flow is undergoing to this transition to turbulence, we will explain, in the next Chapter, how we can model the blood flow and the turbulence effect in a fluid flow using the LES approach.

---

or perfusion pressure), and the current of the blood flow, F, by: $R = \frac{\Delta P}{F}$ (see Figure 1.7).

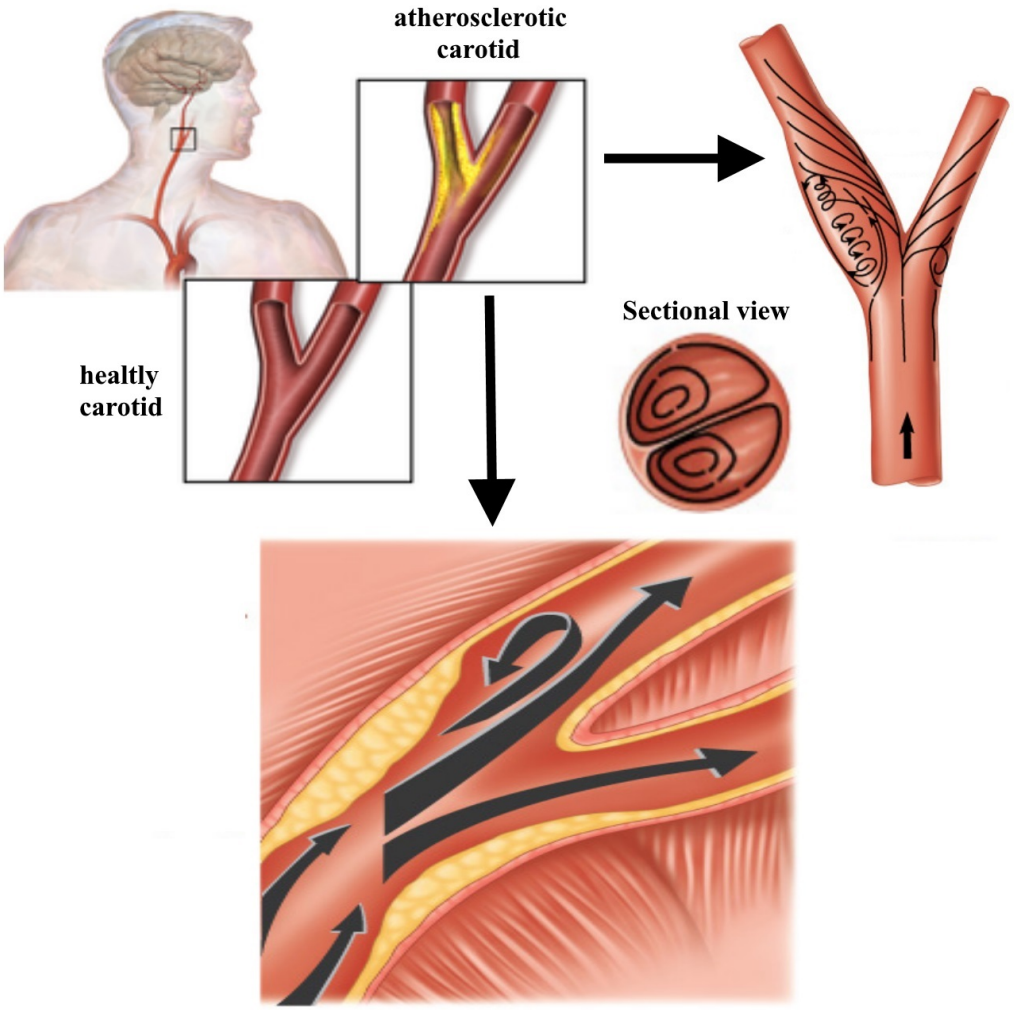

Figure 1.8: Healthy and atheroslerotic catotid (pictures taken from *www.wikipedia.org*).

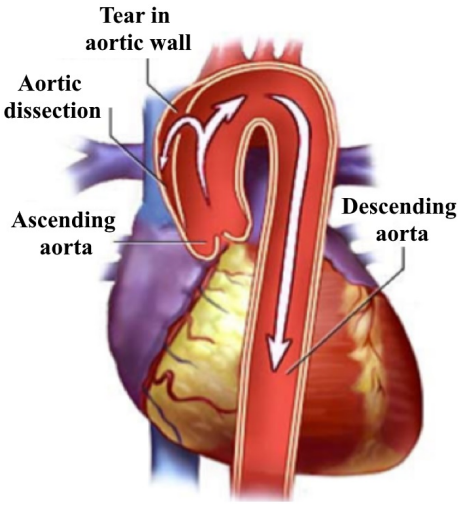

(a) Aorta.

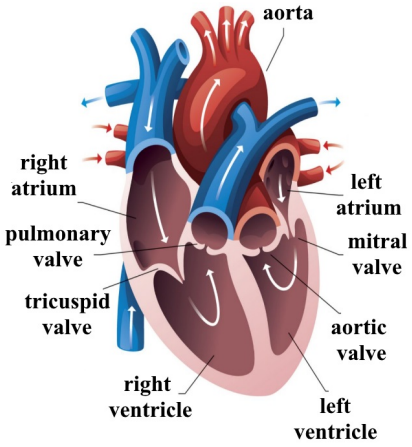

(b) Heart.

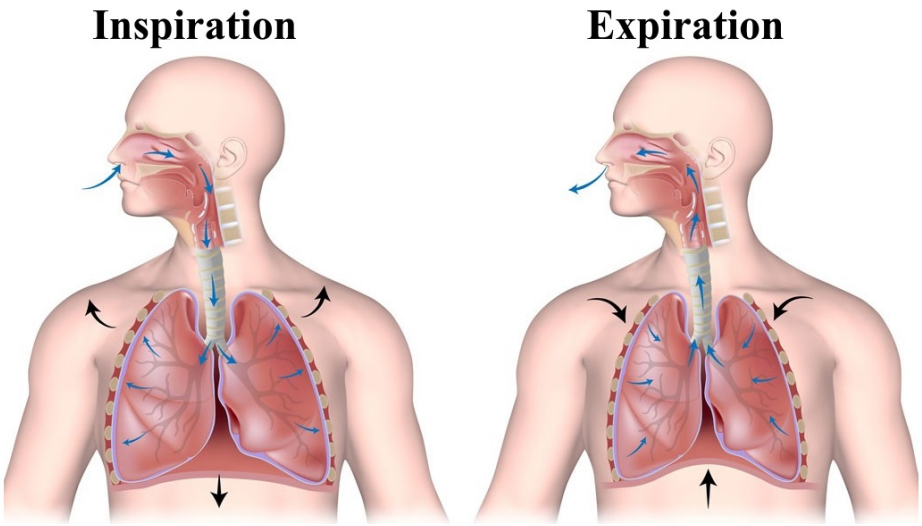

(c) Breathing.

Figure 1.9: Other examples of turbulent flow in circulatory system and in pulmonary airway (pictures taken from *www.pedilung.com*, *www.slideshare.net*, *www.thoughtco.com*).

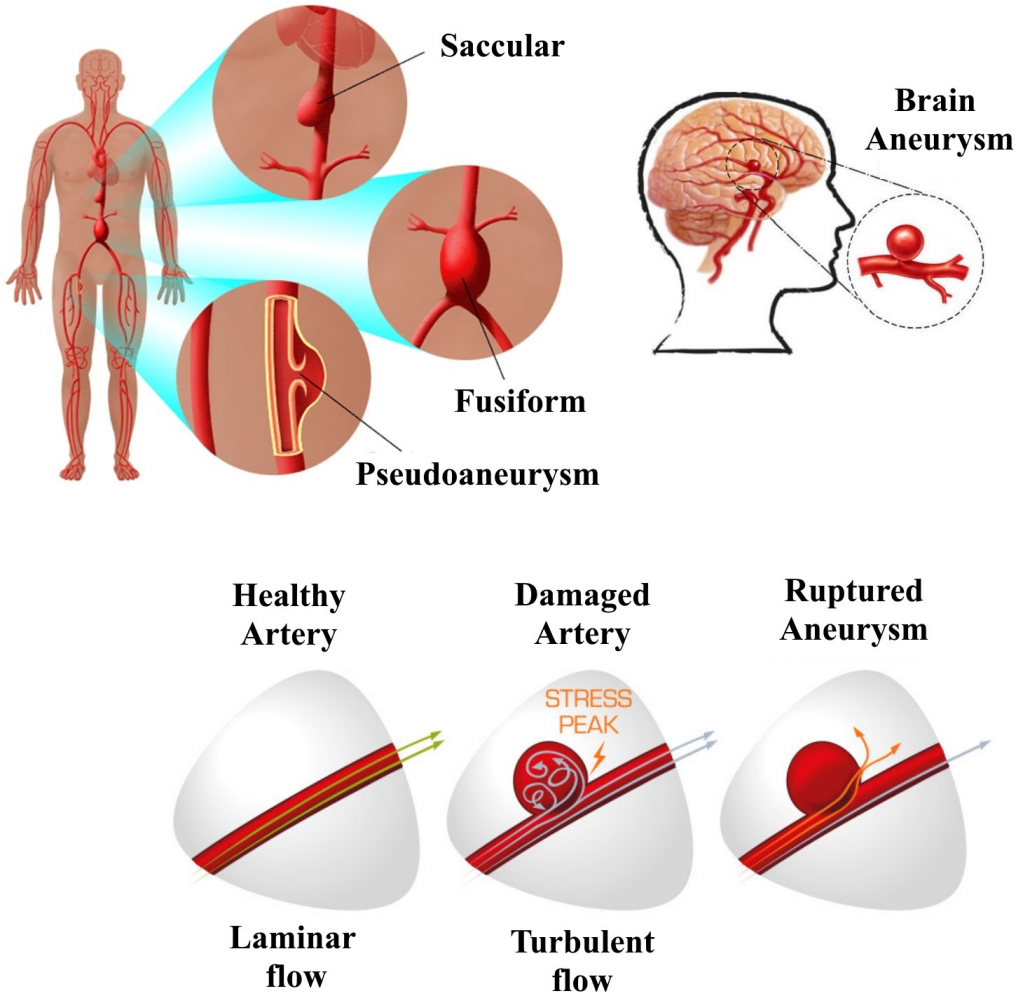

Figure 1.10: Different types of aneurysms (pictures taken from *www.stanfordhealthcare.org*, *www.steptohealth.com*, *www.cardiatis.com*).

1.2.1 Turbulence in Abdominal Aortic Aneurysms

An aneurysm consists in the dilatation of the vessel wall (at least 50% of the normal artery's diameter [87]) with formation of a bulge, mainly in aorta and cerebral arteries, due to a loss of elastin resulting in a weakening of the arterial wall. This process is usually gradual and distributed over years. This dilatation makes the arterial wall thinner and weaker and so, prone to rupture or dissection: $80-90\%$ of ruptured abdominal aortic aneurysms and 45% of ruptured cerebral aneurysms result in death.

Aneurysms can be classified in two groups according to the shape [88],

[10]: fusiform aneurysm and saccular aneurysm (see Figure 1.10). In fusiform aneurysm the dilation involves all the aortic segment, and it is more common in abdominal aorta, in particular, abdominal aortic aneurysms (AAA) are usually found in the segment of the aorta between the renal arteries and the iliac bifurcation (see Figure 1.10). Saccular aneurysm, on the other hand, is caused by a weakening of only one side of the artery wall resulting in a spherical or balloon-like shape and can be found mainly in the arteries of the cerebral circulation (see Figure 1.10).

The role of blood fluid-dynamics has been recognized to be crucial for the development of these diseases [89, 90]. In particular, wall shear stresses, i.e. the viscous/friction forces exerted by the blood on the wall vessel, although about 100 times smaller in magnitude than pressure, regulate the permeability of the wall and the loss of elastin, thus playing an important role in aneurysm development [90] (see Figure 1.10). Although not determined mainly by wall shear stress, the rupture process may be influenced by turbulence in the aneurysm, since the corresponding arterial wall vibration may damage the structural components of the wall [91, 92].

In AAA there is a complex fluid dynamics, characterized by a disturbed flow, vortices, recirculation regions, backflow and possible transition to turbulence. The effects of transition to turbulence in AAA is related to the heart pulsatility and the sudden change of diameter of the vessels [20].

For these reasons, the inclusion of turbulence effects is mandatory for a computational study of blood dynamics in AAA and for an accurate description of the aneurysm evolution [19]. A particularly important motivation for a numerical investigation of AAA is to better evaluate the risk of rupture. In clinical practice, the current parameter used to evaluate the probability of rupture is the aneurysm diameter: patients with an aneurysm diameter of $\sim 5\ cm$ are considered for elective repair [19]. This estimation is a too rough approximation of the risk of rupture derived from the Law of Laplace that states that the wall tension in a sphere is proportional to the radius. However, some studies found that there is no significant correlation between tensile strength or rupture probability and diameter [93, 44] and the main reason is that the shape of an aneurysm is significantly different from a sphere. So, the probability of rupture depends also on the local strength of the AAA wall. Moreover, AAA are mostly present in men and women older than 65 year [94] and there is also high risk of complication caused by a surgical intervention.

For all these reasons, a somewhat more precise evaluation of the risk of rupture against the risk of surgical complication is mandatory for this disease. This can be achieved by a mathematical modeling of the problem.

Chapter 2

Mathematical models

2.1 Blood flow modeling

Blood flow refers to the movement of blood through a vessel, tissue, or organ. It is initiated by the contraction of the ventricles of the heart. Ventricular contraction ejects blood into the major arteries, resulting in flow from regions of higher pressure to regions of lower pressure, as blood encounters smaller arteries and arterioles, then capillaries, then the venules and veins of the venous system (see Figure 2.1).

Blood is made by plasma (about 55% of its total volume) in which cellular elements are suspended. Plasma is an aqueous solution mainly composed by water, 92% by volume. The cellular part [82, 83, 84] is composed by platelets, white blood cells and red blood cells[1]. Nearly half of the blood's volume (40% to 45%) is red blood cells. For this reason, they are the most important factor for the mechanical properties of blood. In particular, the slight compressibility of the blood is due to the presence of red blood cells. However, in many situations (e.g. in the abdominal aorta) the changes in pressure and temperature are sufficiently small that the changes in density are negligible. So, we can assume the blood as an incompressible fluid [9].

The diameter of blood cells is approximately $10^{-3}\,cm$, whereas that of the arteries/veins is about $10^{-1}\,cm$. In particular, the vessel for medium and large vessels diameters have a dimension of some millimeters in the case of coronaries, up to some centimeter in the case of the aorta. Hence, because the differece between the blood cells and the arteries is more than two order of magnitude, we can consider the blood as Newtonian, i.e. characterized

[1] The main function of platelets is to stop bleeding blood vessel damages. White blood cells are involved in protecting the organism from infections. Red blood cells deliver oxygen to the body tissues via blood flow through the circulatory system.

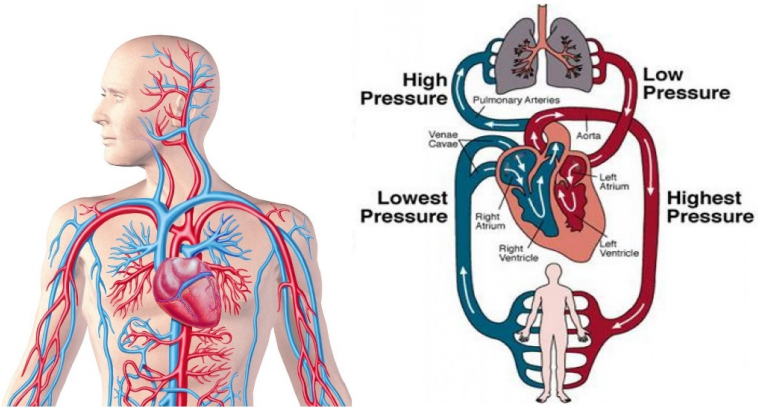

Figure 2.1: The human circulatory system (simplified). Red indicates oxygenated blood carried in arteries, blue indicates deoxygenated blood carried in veins (pictures taken from *www.interactive-biology.com*, *www.ainuna.com*).

by a linear relationship between internal forces and velocity gradients [10] [85]. In particular, a Newtonian fluid is a fluid where viscosity does not depend on the velocity. However, in the smallest arteries, such as coronaries in presence of a vessel narrowing (stenosis), a non-Newtonian blood is more appropriately assumed [86].

For all the reasons mentioned above, blood is modeled as a constant density, Newtonian and homogeneous fluid, a well accepted hypothesis for medium and large vessels [8, 9, 10]. As a consequence, blood fluid dynamics in large vessels (like the abdominal aorta) is modeled by the incompressible Navier-Stokes equations for a Newtonian fluid. In particular, in the abdominal aorta, the incompressibility approximation is supported by the size of blood cells that presents a difference of about three order of magnitude from aortic diameter.

The most suitable way to model blood flow dynamics is to take into account the interaction with the vessel wall. In fact, there is a significant energy exchange between the vessel and the fluid at the interface. This interconnection is described by a coupled problem, named Fluid-Structure-Interaction (FSI), which leads to a very complex non-linear system of Partial Differential Equations (PDE). In this thesis, we make the assumption of vessels *rigid wall*, because our primarily aim is to study and compare different turbulence models able to describe turbulent and transitional phenomena in AAA. We stress that however a FSI simulations could increase the accuracy of the results obtained in this thesis.

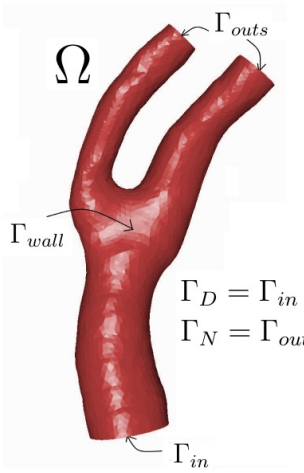

Figure 2.2: Choices of the Dirichlet ($\Gamma_{in} \cup \Gamma_{wall}$) and Neumann ($\Gamma_{outs}$) boundaries for a carotid domain (Ω) in the fluid stand-alone problem (reconstructed from Magnetic Resonance Angiography, MRA, images). Picture taken from [55].

Let's consider the hemodynamic problem concerning a portion of blood vessel which is part of an entire cardiovascular system (Figure 2.1).

Let $\Omega \subset \mathbb{R}^3$ be the spatial blood fluid vessel domain with a smooth boundary $\partial\Omega \equiv \Gamma$, where $\Gamma = \Gamma_N \cup \Gamma_D$, with $\Gamma_D = \Gamma_{in} \cup \Gamma_{wall}$ the subset of Γ in which the essential (Dirichlet) boundary conditions are set, while $\Gamma_N = \Gamma_{outs}$ the portion of the boundary where natural (Neumann) boundary conditions have been considered. Moreover, $\Gamma_N = \Gamma \backslash \Gamma_D$, and $\mathring{\Gamma}_N \cap \mathring{\Gamma}_D = \emptyset$ (see Figure 2.2).

Introducing an unknown velocity field $\mathbf{u}(\mathbf{x}, t) : \Omega \times [0, T] \to \mathbb{R}^3$ and an unknown pressure field $p(\mathbf{x}, t) : \Omega \times [0, T] \to \mathbb{R}$, in absence of body forces[2], the NS equations for an incompressible fluid read

$$\frac{\partial \mathbf{u}}{\partial t} + (\mathbf{u} \cdot \nabla)\mathbf{u} - \frac{1}{\rho}\nabla \cdot \boldsymbol{\sigma}(\mathbf{u}, p) = \mathbf{0} \qquad \text{in } \Omega \times (0, T], \quad (2.1a)$$

$$\nabla \cdot \mathbf{u} = 0 \qquad \text{in } \Omega \times (0, T], \quad (2.1b)$$

$$\mathbf{u} = \mathbf{g} \qquad \text{on } \Gamma_D \times (0, T], \quad (2.1c)$$

$$\boldsymbol{\sigma}(\mathbf{u}, p)\hat{\mathbf{n}} = \mathbf{h} \qquad \text{on } \Gamma_N \times (0, T], \quad (2.1d)$$

$$\mathbf{u}(\mathbf{x}, 0) = \mathbf{u}_0(\mathbf{x}) \qquad \text{in } \Omega \times \{0\}, \quad (2.1e)$$

[2]Blood flow to all parts of the body is primarily regulated by blood pressure. Arterial blood pressure outweighs gravitational fluid force.

where $\hat{\mathbf{n}}$ is the outward directed unit normal vector to Γ_N, $\boldsymbol{\sigma}$ is the Cauchy stress tensor, ρ is the fluid density, and ∇ and $\nabla\cdot$ are the usual gradient and divergence operators. The functions $\mathbf{g}$ and $\mathbf{h}$ indicate suitable Dirichlet and Neumann data, respectively, while $\mathbf{u}_0$ is the known initial field solution at time $t = 0$.

For a Newtonian fluid, the Cauchy stress tensor $\boldsymbol{\sigma}$ depends linearly on the components of the strain rate tensor:

$$\boldsymbol{\sigma}(\mathbf{u}, p) = -p\mathbf{I} + 2\mu\mathbf{S}(\mathbf{u}),$$

where μ is the dynamic viscosity of the fluid (taken to be a known constant) and $\mathbf{I}$ is the second order identity tensor, while $\mathbf{S}(\mathbf{u})$ is the strain rate tensor

$$\mathbf{S}(\mathbf{u}) = \frac{1}{2}\big[\nabla\mathbf{u} + (\nabla\mathbf{u})^T\big].$$

We recall that the first equation (2.1a) represents the balance of momentum and the second one (2.1b) the conservation of the mass, also called continuity equation (or incompressible constraint). Equations (2.1c), (2.1d), and (2.1e) guarantee the well posedness of the problem[3]. Vectorial functions $\mathbf{u}_0$, $\mathbf{g}$, and $\mathbf{h}$ are assigned.

Because the blood vessel domain Ω is a portion of the entire circulatory sistem (Figure 2.1), it is appropriate to simulate the blood flow not as an isolated system. In hemodynamics, it is a common practice to impose a velocity profile, $\mathbf{u}_{in}$, at the inlet, Γ_{in}, fitting an experimental measured flow rate Q_{in} [11]:

$$\mathbf{u} = \mathbf{u}_{in}(Q_{in}) \qquad \text{on } \Gamma_{in} \times (0, T]\,.$$

Thanks to the *rigid wall* hypothesis, we impose a null velocity on the vessel wall, Γ_{wall}:

$$\mathbf{u} = \mathbf{0} \qquad \text{on } \Gamma_{wall} \times (0, T]\,.$$

At the outlets, Γ_{outs}, because of the incompressibility constraint (2.1b), we impose a zero-traction condition (homogeneous Neumann boundary condition)[4]:

$$\boldsymbol{\sigma}(\mathbf{u}, p)\hat{\mathbf{n}} = \mathbf{0} \qquad \text{on } \Gamma_{outs} \times (0, T]\,.$$

[3] In the 2-D case, the NS equations, with initial and boundary conditions, give rise to well posed problem (see [81]): solutions with continuous derivatives, and without singularities in time, for regular data. Instead, in the 3-D case existence and uniqueness have only been demonstrated for small time.

[4] We will see later on that on the outlets we do not really set a Neumann boundary condition but a Robin non linear condition related to the Backflow stabilization.

In the next Chapter we will see more in detail the imposed boundary conditions for our specific case (AAA).

So, the general hemodynamic mathematical problem we want to solve is:

Find, $\forall t \in (0,T]$, velocity $\mathbf{u}(\mathbf{x},t)$ and pressure $p(\mathbf{x},t)$ such that:

$$\frac{\partial \mathbf{u}}{\partial t} + (\mathbf{u}\cdot\nabla)\mathbf{u} + \nabla\hat{p} - 2\nu\nabla\cdot\mathbf{S}(\mathbf{u}) = \mathbf{0} \qquad \text{in } \Omega\times(0,T]\,, \tag{2.2a}$$

$$\nabla\cdot\mathbf{u} = 0 \qquad \text{in } \Omega\times(0,T]\,, \tag{2.2b}$$

$$\mathbf{u} = \mathbf{u}_{in}(Q_{in}) \qquad \text{on } \Gamma_{in}\times(0,T]\,, \tag{2.2c}$$

$$(-\hat{p}\mathbf{I} + 2\nu\mathbf{S}(\mathbf{u}))\,\hat{\mathbf{n}} = \mathbf{0} \qquad \text{on } \Gamma_{outs}\times(0,T]\,, \tag{2.2d}$$

$$\mathbf{u} = \mathbf{0} \qquad \text{on } \Gamma_{wall}\times(0,T]\,, \tag{2.2e}$$

$$\mathbf{u}(\mathbf{x},0) = \mathbf{u}_0(\mathbf{x}) \qquad \text{in } \Omega\times\{0\}\,, \tag{2.2f}$$

where, $\nu = \frac{\mu}{\rho}$ is the kinematic viscosity, and the pressure is rescaled by ρ, $\hat{p} = \frac{p}{\rho}$. However, for the sake of clearness, we will neglect the hat on pressure variable in what follows. Equations (2.2) are the strong formulation of the incompressible Navier-Stokes equations for a constant density, Newtonian and homogeneous fluid (see Figure 2.2).

We note that in the strong formulation, due to incompressibility constraint (2.2b), we have the equivalence

$$2\nu\nabla\cdot\mathbf{S}(\mathbf{u}) = \nu\Delta\mathbf{u}.$$

However, this equivalence is no longer valid for what concern the boundary conditions, because the (2.2d) is the correct way to impose the normal stress tensor on the Neumann boundary.

Observing the (2.2a), we can say that the Reynolds number tells us how important is the non linear term, $(\mathbf{u}\cdot\nabla)\mathbf{u}$, compared to the dissipative term, $\nu\Delta\mathbf{u}$:

$$\frac{(\mathbf{u}\cdot\nabla)\mathbf{u}}{\nu\Delta\mathbf{u}} \approx \frac{\frac{U^2}{L}}{\nu\frac{U}{L^2}} = \frac{UL}{\nu} = Re.$$

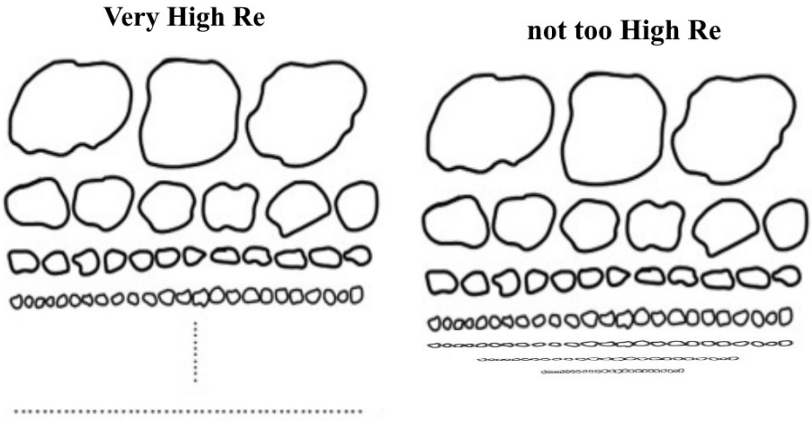

(a) DNS not feasible (b) DNS feasible.

Figure 2.3: Schematic representation of Direct Numerical Simulations for "very high" Re (a) and "not too high" Re (b).

2.2 Turbulence modeling

If we want to completely capture a statistically homogeneous and isotropic turbulent fluid flow motion, we have to solve (numerically) the Navier-Stokes equations which, as mentioned before, describe the fluid flow. To accomplish this task, we have to discretize these equations in space and time capturing all the scales associated to our problem, including the smallest scales. We will describe this discretization process in detail in Chapter 3. In this Section we want only to justify the introduction of turbulence model which is strictly related to numerical discretization.

For a 3D turbulence, assuming that L is equal to the dimension of the domain (for example, in a cube of side equal to L), the relation (1.1) implies

$$N_{d.o.f} = \left[\frac{L}{\eta}\right]^3 \sim O(Re^{\frac{9}{4}}),$$

where $N_{d.o.f}$ indicates the number of degree of freedom - d.o.f[5]. This means that we need $O(Re^{\frac{9}{4}})$ d.o.f. to represent all the scales. Namely, for $Re \sim 10^6$ we need ten thousand of billions of mesh points

$$N_{d.o.f} \sim O(Re^{\frac{9}{4}}) \sim 10^{13}.$$

[5]The $N_{d.o.f}$, at numerical level, is the finite dimension of the discretized NS solution. In particular we have different number of d.o.f. for pressure and velocity (for details, see Section 3.2.1).

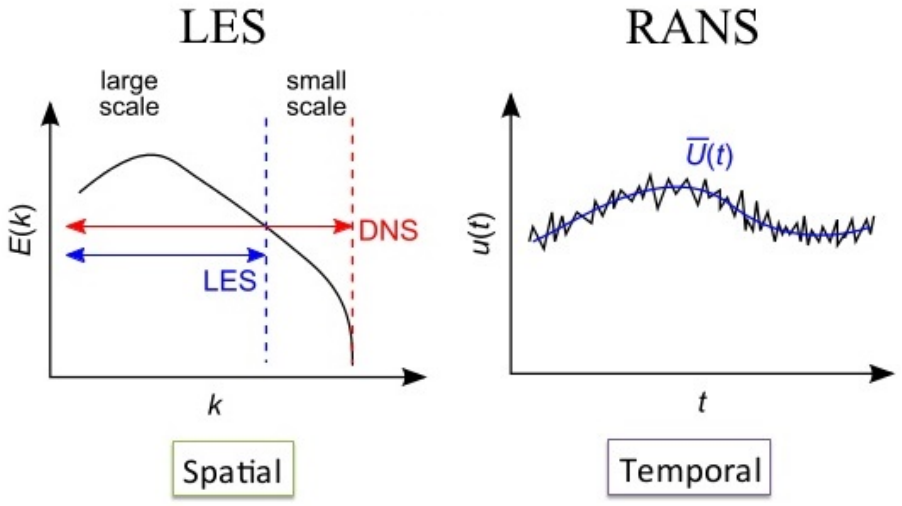

(a) LES methods. (b) RANS methods.

Figure 2.4: LES versus RANS approach.

Moreover, the evolution of the smallest eddies is very small itself and can be derived in K41 from

$$\frac{t_L}{t_\eta} \sim O(Re^{\frac{1}{2}}),$$

where t_L and t_η are respectively the typical time evolution of the L.S. and S.S. eddies (see Figure 1.5).

For these reasons, the computation of very high Reynolds number flows resolving all the physical scales of the flow (Direct Numerical Simulation, DNS), is prohibitive (see Figure 2.3a). Anyway, for Re not "too" high the DNS can be done using a lot of computational resources (see, Figure 2.3b).

In order to find another way to fully describe turbulent flows, we need to find some turbulence modeling allowing to reduce the computational cost by the introduction of a coarser description of the flow (i.e. reducing the $N_{d.o.f.}$ of the discretized NS equations).

Two are the widely used approaches of turbulence modeling:

A: to compute only the averaged flow field (Figure 2.4b). This approach is called Reynolds Averaged Navier Stokes, or RANS [6];

B: to compute only the largest spatial scales of the flow, and suitably model the small scales (Figure 2.4a). This approach is named Large Eddy Simulation, or LES [7].

Using RANS methods, we are not interested in describing exactly the velocity flow field at every scale and at every time. RANS equations are averaged equations of motion for fluid flow. The idea behind RANS is the Reynolds decomposition, whereby the instantaneous velocity flow field, $\mathbf{u}(\mathbf{x}, t)$ is decomposed into its averaged, $\overline{\mathbf{u}}$, and fluctuating quantities $\mathbf{u}'$

$$\mathbf{u}(\mathbf{x}, t) = \overline{\mathbf{u}}(\mathbf{x}) + \mathbf{u}'(\mathbf{x}, t).$$

The RANS equations are derived inserting the Reynolds decomposition into the NS equations.

The second approach is based on LES methods, which resolve the largest spatial scales of the flow, corresponding to low-frequency modes, and model the smallest (unresolved) scales. The idea behind the LES methods is a filtering procedure (with a low frequency pass filter) in which the velocity field $\mathbf{u}(\mathbf{x}, t)$ is decomposed into its filtered quantity, $\overline{\mathbf{u}}$, and fluctuating quantities $\mathbf{u}'$

$$\mathbf{u}(\mathbf{x}, t) = \overline{\mathbf{u}}(\mathbf{x}, t) + \mathbf{u}'(\mathbf{x}, t).$$

The LES equations are derived inserting this decomposition into the NS equations.

Although the equations produced by both RANS and LES methods look very similar, there is an important difference between RANS and LES approaches. The LES methods will tend to the DNS with the mesh grid refinement[6], while, in any RANS method it does not make any sense to use a finer grid as soon as we are resolving the average flow field.

In this thesis, we chose the LES approch [7]. In particular, we used the so called σ-models (static and dynamic) [30] [38], whose details will be described in the next Section.

[6] We will highlight this property of LES methods in the next Section.

2.3 Large Eddy Simulation

The Direct Numerical Simulation (DNS) of turbulent flows requires the full representation of the whole range of spatial and temporal turbulent scales at the discrete level [1, 28, 29].

The Large Eddy Simulation (LES) is a turbulence modeling approach which strongly reduces the computational cost with respect to a DNS. In fact, in the LES approaches [1, 7, 30] only the "large scales" of the flow field are fully represented and resolved at the discrete level, while the effect of the "small" unresolved scales is taken into account by means of suitable models based on the resolved scales. This is the reason why the computational costs of LES is more affordable with respect to a DNS.

The steps to perform a LES are:

1. separation of the small (unresolved) scales from the large (resolved) scales by a filtering procedure;

2. modelization of the interaction between the removed smaller scales and the larger ones. In particular, we consider models able to include their effects on the larger scales, obtaining the modeled filtered Navier Stokes equations;

3. solution of the resulting filtered Navier Stokes equations.

2.3.1 Filtering procedure

Scales are separated by applying a high-pass filter in the physical space, i.e. low-pass in the frequency one. This filtering is represented in physical space as a convolution product.

Let us define the generic filtered quantity $\overline{f}(\mathbf{x}, t)$ as

$$\overline{f}(\mathbf{x}, t) = \int_{\Omega} G_{\overline{\Delta}}(\mathbf{r}, \mathbf{x}) f(\mathbf{x} - \mathbf{r}, t) d^3\mathbf{r}, \tag{2.3}$$

which is a convolution of the generic variable f with the filter function G (with a given length $\overline{\Delta}$), resulting in a filtered variable $\overline{f}$.

We can define the fluctuating part, f', of the quantity f as

$$f'(\mathbf{x}, t) = f(\mathbf{x}, t) - \overline{f}(\mathbf{x}, t).$$

Hence, $G_{\overline{\Delta}}(\mathbf{r}, \mathbf{x})$ is the low pass filter that take away all the high frequencies modes of the generic variable $f(\mathbf{x}, t)$, which are the fluctuating quantity $f'(\mathbf{x}, t)$.

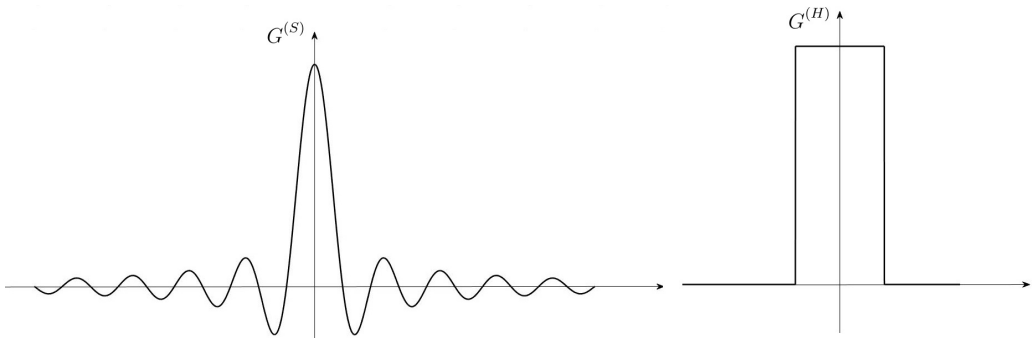

(a) Sharp cut off filter. (b) Box filter.

Figure 2.5: Different types of filter functions for filtering procedure.

Filtering operation commute with time derivative

$$\overline{\frac{\partial f}{\partial t}} = \frac{\partial \overline{f}}{\partial t}$$

because we are assuming that the filter $G_{\overline{\Delta}}(\mathbf{r}, \mathbf{x})$ does not depend on time.

Moreover, we have the property of linearity and constant conservation

$$\overline{f+g} = \overline{f} + \overline{g} \quad , \quad \overline{cf} = c\overline{f}.$$

Filtering operation does not always commutes with space derivative because $G_{\overline{\Delta}}(\mathbf{r}, \mathbf{x})$ depends on $\mathbf{x}$. Filtering operation and space derivative commute if and only if the filter function $G_{\overline{\Delta}} = G_{\overline{\Delta}}(\mathbf{r})$ does not depend on $\mathbf{x}$, which means that the $G_{\overline{\Delta}}$ is an homogeneous filter

$$\overline{\frac{\partial f}{\partial x_i}} = \frac{\partial \overline{f}}{\partial x_i} \Longleftrightarrow G_{\overline{\Delta}} = G_{\overline{\Delta}}(\mathbf{r}).$$

For now on, we will assume that the filter function is homogeneous. Moreover, for the sake of easier analysis, we also assume that our filter $G_{\overline{\Delta}}$ is also isotropic, which means that its dependence on $\mathbf{r}$ is just through the magnitude $r = \|\mathbf{r}\|$.

Since the filtering operation is a convolution, for an homogeneous $G_{\overline{\Delta}}(r)$, the spatial Fourier transform of equation (2.3) is

$$\widehat{\overline{f}}(k) = \widehat{G}_{\widehat{\Delta}}(k)\widehat{f}(k),$$

where $\widehat{f}$ indicates the Fourier transform of the quantity f, $\widehat{f} = FT(f)$, and $\widehat{\Delta}$ represents the filter width in the Fourier space.

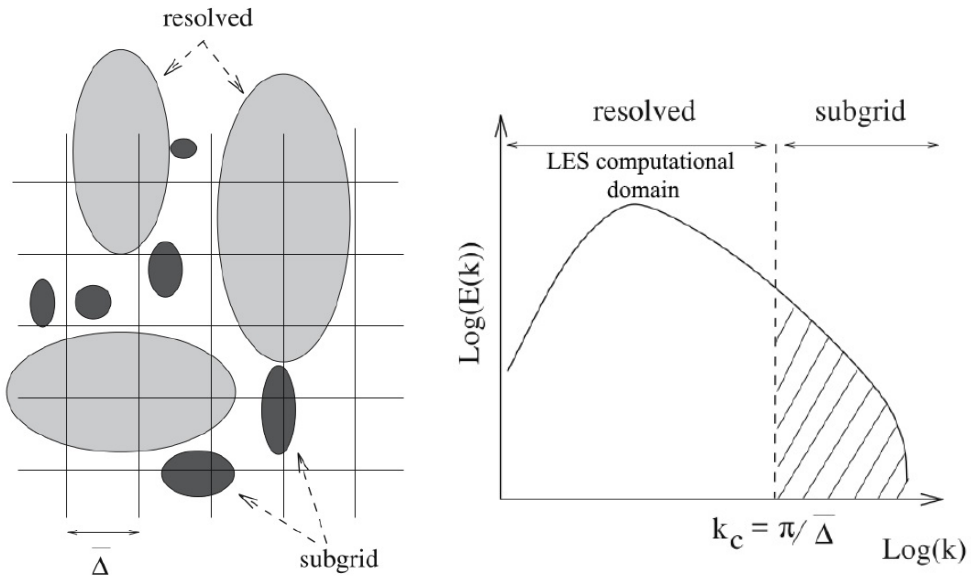

(a) Physical space. (b) Fourier space.

Figure 2.6: Filtering procedure in Physical and Fourier space. Pictures taken from [69].

In general the filtered fluctuation is not zero because it depends on the filter $G_{\overline{\Delta}}$. This means that if we filter two times the function f we will not get the same quantity

$$\overline{f'} \neq 0 \Longrightarrow \overline{\overline{f}} \neq \overline{f}.$$

The filtered fluctuation is zero only if $G_{\overline{\Delta}}$ is a sharp cutoff filter (see Figure 2.5a) which is also an homogeneous filter. In fact, the Fourier transform of a sharp cutoff off filter is the Heaviside function (Figure 2.5b)

$$G(r) = \frac{\sin(\frac{1}{2}r\overline{\Delta})}{\frac{1}{2}r\overline{\Delta}} \Longrightarrow \widehat{G}(k) = H\left(\frac{\pi}{\widehat{\overline{\Delta}}} - k\right).$$

Hence, due to the fact that for a sharp cutoff filter $\widehat{G}\widehat{G} = \widehat{G}$, we have

$$\widehat{\overline{\overline{f}}} = \widehat{G}\widehat{G}\widehat{f} = \widehat{G}\widehat{f} = \widehat{\overline{f}},$$

from which, doing the inverse Fourier transform of both members, we arrive at

$$\overline{\overline{f}} = \overline{f} \Longrightarrow \overline{f'} = 0.$$

The quantity $\widehat{\Delta}$ represents the cutoff length. This means that, in doing the filtering procedure, we get only the scales (or low spatial frequencies) $|k| < \frac{\pi}{\widehat{\Delta}}$ (see Figure 2.6b)).

2.4 Filtered Navier-Stokes equations

LES models are based on the decomposition of the fluid unknowns in resolved and unresolved quantities, $[\overline{\mathbf{u}}, \overline{p}]$ and $[\mathbf{u}', p']$, respectively, so that

$$\mathbf{u} = \overline{\mathbf{u}} + \mathbf{u}' \quad , \quad p = \overline{p} + p'.$$

The resolved quantities are referred to as filtered [32], since a filtering operation is performed over the fluid equations.

In order to derive a set of equations for $\overline{\mathbf{u}}$ and $\overline{p}$, a formal filtering procedure is performed over the Navier-Stokes equations (2.2), obtaining

$$\begin{aligned} &\overline{\frac{\partial \mathbf{u}}{\partial t}} + \overline{(\mathbf{u}\cdot\nabla)\mathbf{u}} + \overline{\nabla p} - 2\nu\overline{\nabla\cdot\mathbf{S}(\mathbf{u})} = \mathbf{0} && \text{in } \Omega\times(0,T]\,, \\ &\overline{\nabla\cdot\mathbf{u}} = 0 && \text{in } \Omega\times(0,T]\,. \end{aligned}$$

Exploiting the commutative property with time and spatial derivatives for an homogeneous filter, we obtain

$$\frac{\partial \overline{\mathbf{u}}}{\partial t} + \overline{(\mathbf{u}\cdot\nabla)\mathbf{u}} + \nabla\overline{p} - 2\nu\nabla\cdot\mathbf{S}(\overline{\mathbf{u}}) = \mathbf{0} \qquad \text{in } \Omega\times(0,T]\,, \tag{2.4a}$$

$$\nabla\cdot\overline{\mathbf{u}} = 0 \qquad \text{in } \Omega\times(0,T]\,, \tag{2.4b}$$

where we stress that the non linear term $\overline{(\mathbf{u}\cdot\nabla)\mathbf{u}}$ cannot be expressed in term of the filtered quantities $\overline{\mathbf{u}}$ and $\overline{p}$. Indeed, the filtered non-linear term can be written in components as

$$\left(\overline{(\mathbf{u}\cdot\nabla)\mathbf{u}}\right)_i = \sum_{j=1}^{3} \overline{u_j \frac{\partial u_i}{\partial x_j}} = \sum_{j=1}^{3} \frac{\partial\, \overline{u_i u_j}}{\partial x_j}, \tag{2.5}$$

where we have used the homogeneous filter commutation property and also the incompressibility constraint [7]. By adding and subtracting the term $\overline{u_i}\,\overline{u_j}$ inside (2.5) we obtain

$$\begin{aligned} \left(\overline{(\mathbf{u}\cdot\nabla)\mathbf{u}}\right)_i &= \sum_{j=1}^{3} \frac{\partial\, \overline{u_i u_j} - \overline{u_i}\,\overline{u_j}}{\partial x_j} + \sum_{j=1}^{3} \frac{\partial\, \overline{u_i}\,\overline{u_j}}{\partial x_j} = \\ &= \left[\nabla\cdot(\overline{\mathbf{u}\otimes\mathbf{u}} - \overline{\mathbf{u}}\otimes\overline{\mathbf{u}})\right]_i + \left[(\overline{\mathbf{u}}\cdot\nabla)\overline{\mathbf{u}}\right]_i, \end{aligned}$$

[7] The incompressibility constraint can be written in component as:

$$\nabla\cdot\mathbf{u} = \sum_i \frac{\partial u_i}{\partial x_i} = 0 \Longrightarrow \sum_j u_j \frac{\partial u_i}{\partial x_j} = \sum_j \frac{\partial u_i u_j}{\partial x_j}.$$

where we have introduced the tensor product operator $(\mathbf{u} \otimes \mathbf{v})_{ij} = u_i v_j$.

Defining the subgrid scale stress tensor τ_{ij}^{sgs} as

$$\tau_{ij}^{sgs} = (\overline{\mathbf{u} \otimes \mathbf{u}} - \overline{\mathbf{u}} \otimes \overline{\mathbf{u}})_{ij} = \overline{u_i u_j} - \overline{u_i}\,\overline{u_j},$$

we can rewrite equations (2.4) as follows

$$\frac{\partial \overline{\mathbf{u}}}{\partial t} + (\overline{\mathbf{u}} \cdot \nabla)\overline{\mathbf{u}} + \nabla \overline{p} - 2\nu \nabla \cdot \mathbf{S}(\overline{\mathbf{u}}) + \nabla \cdot \boldsymbol{\tau}^{sgs} = \mathbf{0} \qquad \text{in } \Omega \times (0,T]\,, \quad (2.6a)$$

$$\nabla \cdot \overline{\mathbf{u}} = 0 \qquad \text{in } \Omega \times (0,T]\,. \quad (2.6b)$$

The subgrid scale stress tensor $\boldsymbol{\tau}^{sgs}$ should contain the effect of the small (unresolved) scales over the large (resolved) scales. The modeling problem regards a suitable choice for $\boldsymbol{\tau}^{sgs}$: this is addressed as the turbulence closure problem. The choice of how to model this term, $\boldsymbol{\tau}^{sgs}$, leads to different LES models.

We do not need to model the complete tensor $\boldsymbol{\tau}^{sgs}$, but its enough to consider only the deviatoric part

$$\boldsymbol{\tau}_d^{sgs} = \boldsymbol{\tau}^{sgs} - \frac{1}{3} Tr(\boldsymbol{\tau}^{sgs})\mathbf{I},$$

where Tr is the trace operator defined as $Tr(\mathbf{A}) = \sum_i A_{ii}$. This is because the tensor $\boldsymbol{\tau}^{sgs}$ enters in the equation (2.6a) as

$$\nabla \cdot \boldsymbol{\tau}^{sgs} = \nabla \cdot \boldsymbol{\tau}_d^{sgs} + \nabla \Pi,$$

where $\Pi = \frac{1}{3} Tr(\boldsymbol{\tau}^{sgs})$. Hence, we can add the isotropic part of the subgrid scale stress tensor to the filtered pressure, defining a modified pressure

$$\overline{P} = \overline{p} + \Pi.$$

The resulting filtered Navier-Stokes equations, for a general hemodynamic problem (2.2), are

$$\frac{\partial \overline{\mathbf{u}}}{\partial t} + (\overline{\mathbf{u}} \cdot \nabla)\overline{\mathbf{u}} + \nabla \overline{P} - 2\nu \nabla \cdot \mathbf{S}(\overline{\mathbf{u}}) + \nabla \cdot \boldsymbol{\tau}_d^{sgs} = \mathbf{0} \qquad \text{in } \Omega \times (0,T]\,, \quad (2.7a)$$

$$\nabla \cdot \overline{\mathbf{u}} = 0 \qquad \text{in } \Omega \times (0,T]\,, \quad (2.7b)$$

$$\overline{\mathbf{u}} = \overline{\mathbf{u}}_{in}(Q_{in}) \qquad \text{on } \Gamma_{in} \times (0,T]\,, \quad (2.7c)$$

$$\left(-\overline{P}\mathbf{I} + 2\nu \mathbf{S}(\overline{\mathbf{u}}) - \boldsymbol{\tau}_d^{sgs}\right)\hat{\mathbf{n}} = \mathbf{0} \qquad \text{on } \Gamma_{outs} \times (0,T]\,, \quad (2.7d)$$

$$\overline{\mathbf{u}} = \mathbf{0} \qquad \text{on } \Gamma_{wall} \times (0,T]\,, \quad (2.7e)$$

$$\overline{\mathbf{u}}(\mathbf{x},0) = \overline{\mathbf{u}}_0(\mathbf{x}) \qquad \text{in } \Omega \times \{0\}\,. \quad (2.7f)$$

A special remark should be highlighted for what concerns the boundary conditions. Indeed, often LES models are written for unbounded domains (in practice, with periodic boundary conditions). However, we can reasonably assume that the boundary conditions in the filtered equations are the same as those of the unfiltered problem. In particular, we have added the deviatoric tensor $\boldsymbol{\tau}_d^{sgs}$ into the Neumann boundary condition because it represents the contribution of the subgrid (unresolved) scales on traction. This is consistent with the fact that the Neumann condition is the "natural" condition [17].

2.5 Eddy viscosity models

The first idea of turbulent eddy viscosity was made by Boussinesq (1877). The concept behind the eddy viscosity model is based on the following hypothesis [7]:

HP "The energy transfer mechanism from the resolved to the subgrid scales is analogous to the molecular mechanisms represented by the diffusion term (in which the viscosity ν appears)."

According to this hypothesis, we made an analogy with the kinetic theory of gases, in which the molecular agitation draws energy from the flow thanks to molecular viscosity. In the same way, the energy cascade mechanism can be modeled by a term with a similar mathematical structure of the molecular diffusion term

$$\boldsymbol{\tau}_d^{sgs} = -2\nu_{sgs}(\overline{\mathbf{u}})\mathbf{S}(\overline{\mathbf{u}}), \tag{2.8}$$

where the subgrid scale viscosity have been introduced, $\nu_{sgs}(\overline{\mathbf{u}})$.

Inserting the model expression (2.8) in the filtered momentum equation of NS (2.7a), we have

$$\frac{\partial \overline{\mathbf{u}}}{\partial t} + (\overline{\mathbf{u}} \cdot \nabla)\overline{\mathbf{u}} + \nabla \overline{P} - 2(\nu + \nu_{sgs}(\overline{\mathbf{u}}))\nabla \cdot \mathbf{S}(\overline{\mathbf{u}}) = \mathbf{0} \qquad \text{in } \Omega \times (0, T]\,.$$

Hence in eddy viscosity models the overall effect of turbulence modeling is to add to the viscous molecular kinematic coefficient ν a new viscosity ν_{sgs}

$$\nu_{eff} = \nu + \nu_{sgs}.$$

To explain and understand this new term, we can make an analogy between the turbulent viscosity term, ν_{sgs}, and the molecular viscosity, ν. First of all, we recall that the total stress tensor for the molecular viscosity is

$$\boldsymbol{\sigma} = 2\nu\mathbf{S} - p\mathbf{I} \Longrightarrow -\nabla \cdot \boldsymbol{\sigma} = -2\nu\nabla \cdot \mathbf{S} + \nabla p.$$

At molecular level there are fluctuations through the molecules which produce a stress tensor $\boldsymbol{\sigma}$. In the cascade of energy most of the velocity fluctuations are present at small scales. Hence, we can imagine that small scales are composed by individual eddies in which velocity fluctuates randomly. Similarly to molecules fluctuation, we can make an analogy between the random motion of molecules and the fluctuations of these eddies. Therefore, we can write an expression for the subgrid viscosity analogous to the molecular one

$$\boldsymbol{\epsilon} := 2\nu_{sgs}\mathbf{S} - \Pi\mathbf{I} \Longrightarrow -\nabla\cdot\boldsymbol{\epsilon} = -2\nu_{sgs}\nabla\cdot\mathbf{S} + \nabla\Pi.$$

Since $\Pi = \frac{1}{3}Tr(\boldsymbol{\tau}^{sgs})$, and $\boldsymbol{\tau}_d^{sgs} = -2\nu_{sgs}(\overline{\mathbf{u}})\mathbf{S}$, we obtained the same terms we have in (2.7a) due to the subgrid scale stress tensor. We underline that this is only an analogy and it is not a formal concept.

Eddy viscosity models assume an alignment between the resolved strain rate tensor $\mathbf{S}$ and the deviatoric part of subgrid stress tensor $\boldsymbol{\tau}_d^{sgs}$, due to their direct proportionality. However it has been shown that this alignment is not physical [33, 34, 35]. Nonetheless, the eddy viscosity models have been widely used because of the easy computational implementation.

Different choices of $\nu_{sgs}(\overline{\mathbf{u}})$ lead to different eddy viscosity models. The first eddy viscosity model was proposed by Smagorinsky (1963) and it is based on the following choice [36]

$$\nu_{sgs} = \nu_{sgs}^{smag} = C_S\overline{\Delta}^2|\mathbf{S}(\overline{\mathbf{u}})|,$$

where, $\overline{\Delta}$ is the filter width, $|\mathbf{S}(\overline{\mathbf{u}})| = \sqrt{2\mathbf{S}(\overline{\mathbf{u}}):\mathbf{S}(\overline{\mathbf{u}})}$ (in which ":" is the operator such that $\mathbf{A}:\mathbf{B} = \sum_{ij}A_{ij}B_{ij}$, for two generic tensor $\mathbf{A}$ and $\mathbf{B}$), and the value of C_S, named the Smagorinsky costant, has to be suitably chosen [31, 37].

The Smagorinky model has the nice feature to vanish for pure rotations, but it does not vanish in near-wall regions and for pure shear [38]. Moreover, it is too dissipative in laminar regions [39]. It has been used in several works for the analysis of the fluid-dynamics in stenotic vessels, see [17, 40, 41, 42, 43].

2.5.1 Static Sigma model

The eddy viscosity model considered in this thesis is the $\sigma-$model [38]. This model is based on the introduction of the singular values of the gradient of velocity $\nabla\overline{\mathbf{u}}$[8]

$$\sigma_i = \sqrt{\text{eig}[(\nabla\overline{\mathbf{u}})^T\nabla\overline{\mathbf{u}}]}, \qquad i = 1, 2, 3,$$

where

$$\sigma_1(\mathbf{x}, t) \geq \sigma_2(\mathbf{x}, t) \geq \sigma_3(\mathbf{x}, t) > 0,$$

are used to build the subgrid-scale viscosity as

$$\nu_{sgs} = \nu_{sgs}^{\sigma} = C_\sigma \overline{\Delta}^2 \left[\frac{\sigma_3(\sigma_1 - \sigma_2)(\sigma_2 - \sigma_3)}{\sigma_1^2}\right],$$

where C_σ is a suitable constant.

The σ-model vanishes for both pure rotation, like Smagorinsky model, and pure shear, since σ_3 is zero for a two dimensional flow (such as a pure rotation). The term ν_{sgs}^{σ} vanishes also when the resolved scales are in axisymmetric or isotropic configuration due to the fact that $\sigma_2 = \sigma_1$ or $\sigma_3 = \sigma_1$ in case of a axisymmetric configuration, and $\sigma_2 = \sigma_1 = \sigma_3$ in case of isotropy. Moreover, the turbulent stresses decay as the distance to the solid boundary.

All these features make the σ-model suitable to simulate fluid flow in the presence of shear layers (as it happens in our case). For this reason it has also been successfully used in other cardiovascular applications [17, 20, 44]. For example, in [26] the σ-model was successfully applied to describe the ventricular blood fluid-dynamics.

The σ-model is characterized by the choice *a priori* of the constant C_σ appearing in the subgrid scale tensor model. We refer to static σ-model when the parameter C_σ is fixed to a constant value during the simulation.

[8] We recall that the singular values of a matrix $A \in \mathbb{R}^{m\times n}$, are defined as the square root of the eigenvalues of the matrix A^TA

$$\sigma_i = \sqrt{\text{eig}(A^TA)} \qquad i = 1, ..., n.$$

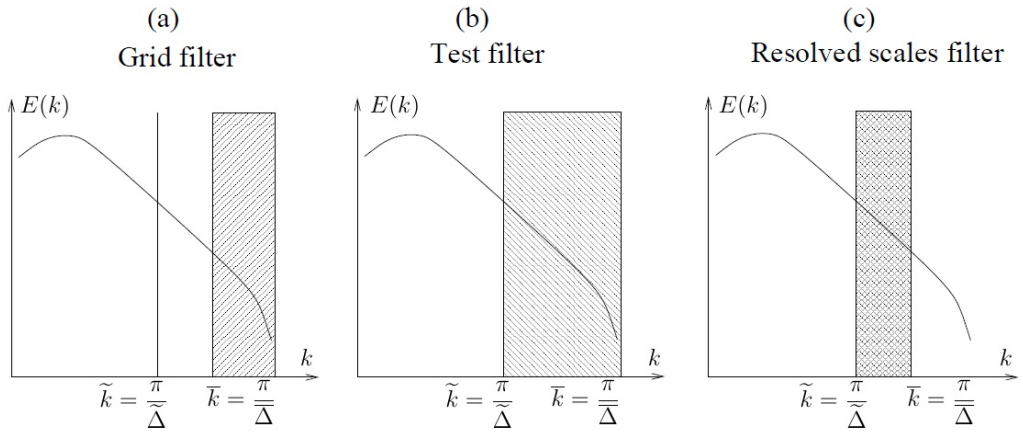

Figure 2.7: Filters involved in the Germano dynamic procedure. Picture taken from [4]

2.5.2 Dynamic Sigma model

In this thesis, besides the use of static σ-model, we also considered the dynamic procedure in which C_σ is not prescribed at the beginning but computed during the simulation: here we refer to dynamic σ-model.

Many LES models (Smagorinsky and σ-model) are characterized by the choice of the constant C appearing in the subgrid scale tensor.

The dynamic procedure, introduced in [39, 45, 46], is an effective way to provide an estimation of this constant C. It is based on the Germano identity to automatically compute the constant.

The Germano dynamic procedure introduces a second filter, besides the one associated to the mesh, known as the test filter (hereafter indicated as $\widetilde{(.)}$), which acts on a larger scale (see Figure 2.7b).

The test filter is applied to the filtered momentum equation (2.7) obtaining

$$\frac{\partial \widetilde{\overline{\mathbf{u}}}}{\partial t} + (\widetilde{\overline{\mathbf{u}}} \cdot \nabla)\widetilde{\overline{\mathbf{u}}} + \nabla \widetilde{\overline{P}} - 2\nu \nabla \cdot \mathbf{S}(\widetilde{\overline{\mathbf{u}}}) + \nabla \cdot \mathbf{L}_d = \mathbf{0} \qquad \text{in } \Omega \times (0, T]\,, \tag{2.9}$$

where $\mathbf{L}_d$, in analogy with $\boldsymbol{\tau}_d^{sgs}$ in (2.7a), is the deviatoric part of the resolved stress tensor $\mathbf{L}$ defined by

$$\mathbf{L} = \widetilde{\overline{\mathbf{u}} \otimes \overline{\mathbf{u}}} - \widetilde{\overline{\mathbf{u}}} \otimes \widetilde{\overline{\mathbf{u}}}, \tag{2.10}$$

and the characteristic test filter width, $\widetilde{\Delta}$, is such that $\widetilde{\Delta} > \overline{\Delta}$[9] (with the

[9]We recall that we are considering an isotropic homogeneous sharp cutoff filter. So, in case of $\widetilde{\Delta} > \overline{\Delta}$ which means $\frac{\pi}{\widetilde{\Delta}} < \frac{\pi}{\overline{\Delta}}$ we could use the properties $\widetilde{\overline{f(\mathbf{u})}} = \widetilde{f(\mathbf{u})}$ and $\widetilde{\overline{\mathbf{u}}} = \widetilde{\mathbf{u}}$.

optimal value $\widetilde{\Delta} = 2\overline{\Delta}$ [39]).

Alternatively, we could apply directly the two filters sequentially to the non filtered momentum equation (2.2a) obtaining

$$\frac{\partial \widetilde{\overline{\mathbf{u}}}}{\partial t} + (\widetilde{\overline{\mathbf{u}}} \cdot \nabla)\widetilde{\overline{\mathbf{u}}} + \nabla \widetilde{\overline{P}} - 2\nu \nabla \cdot \mathbf{S}(\widetilde{\overline{\mathbf{u}}}) + \nabla \cdot \mathbf{T}_d = 0 \qquad \text{in } \Omega \times (0, T]\,, \quad (2.11)$$

where, as usual, $\mathbf{T}_d$ is the deviatoric part of the subgrid scale tensor $\mathbf{T}$, named subtest stress tensor, defined by

$$\mathbf{T} = \widetilde{\overline{\mathbf{u}} \otimes \overline{\mathbf{u}}} - \widetilde{\overline{\mathbf{u}}} \otimes \widetilde{\overline{\mathbf{u}}}. \quad (2.12)$$

We recall that the subgrid stress tensor is

$$\boldsymbol{\tau}_{sgs} = \overline{\mathbf{u} \otimes \mathbf{u}} - \overline{\mathbf{u}} \otimes \overline{\mathbf{u}}. \quad (2.13)$$

By a direct comparison of (2.10), (2.12) and (2.13) we derive the so called Germano identity which is the base of the dynamic procedure

$$\mathbf{L} = \mathbf{T} - \widetilde{\boldsymbol{\tau}}_{sgs}.$$

Let us now rewrite in a more compact form the modeled deviatoric part of the subgrid stress tensor appearing in the σ-model

$$\boldsymbol{\tau}_d^{sgs} = -2C_\sigma \overline{\Delta}^2 \beta(\overline{\mathbf{u}}) S(\overline{\mathbf{u}}),$$

where we have introduced $\beta(\overline{\mathbf{u}}) = \frac{\sigma_3(\sigma_1-\sigma_2)(\sigma_2-\sigma_3)}{\sigma_1^2}(\overline{\mathbf{u}})$. We can use the same model also for the deviatoric part of the subgrid tensor $\mathbf{T}$

$$\mathbf{T}_d = -2C_\sigma \widetilde{\Delta}^2 \beta(\widetilde{\overline{\mathbf{u}}}) \mathbf{S}(\widetilde{\overline{\mathbf{u}}}),$$

where we have made the assumption that the constant C_σ does not depend on the filter width.

By expliciting the Germano identity for the deviatoric part of $\mathbf{L}$ we obtain

$$\mathbf{L}_d = \mathbf{T}_d - \widetilde{\boldsymbol{\tau}}_d^{sgs} = C_\sigma \mathbf{M}, \quad (2.14)$$

where $\mathbf{M} = 2(\overline{\Delta}^2 \beta(\overline{\mathbf{u}}) S(\overline{\mathbf{u}}) - \widetilde{\Delta}^2 \beta(\widetilde{\overline{\mathbf{u}}}) \mathbf{S}(\widetilde{\overline{\mathbf{u}}}))$. Because tensors $\mathbf{L}_d$ and $\mathbf{M}$ are both computable, since they depend on $\overline{\mathbf{u}}$, we have found a way to prescribe the constant C_σ. The identity (2.14) must be fulfilled for all tensor components

$$T_{ij}^d = C_\sigma M_{ij} \qquad \forall\, i, j.$$

Whereas, both tensors $\mathbf{T}_d$ and $\mathbf{M}$ are symmetric and with null trace, we have to solve five equations with one unknown. Hence, (2.14) cannot be

chosen to match the five independent components of the tensors. Applying a least-square minimization (as proposed by Lilly [46])

$$C_\sigma \;\; s.t. \quad \frac{d}{dC}\left\{[L_{ij}^d - CM_{ij}][L_{ij}^d - CM_{ij}]\right\}\Big|_{C=C_\sigma} = 0,$$

we obtained the following result

$$C_\sigma(\mathbf{x},t) = \frac{\sum_{ij} M_{ij} L_{ij}^d}{\sum_{ij} M_{ij} M_{ij}},$$

where C_σ is now a function of space and time.

The computed constant C_σ has the following properties:

- it can take negative values (i.e. an anti-dissipative effect is taken into account locally). This characteristic is often interpreted as a backscatter modeling energy cascade (the energy transfers from the smaller modeled scales to the larger resolved ones);
- it is not bounded.

These two properties potentially represent drawbacks for the stability of the simulation as shown in [46, 47]. To avoid numerical instabilities, we can statistically average C_σ in time or locally in space [47]. Moreover, we can limit the value of C_σ using arbitrary bounds [47] (procedure known as clipping) to ensure that

I $\nu_{eff} = \nu + \nu_{sgs} \geq 0$;

II $|C_\sigma| \leq C_{\sigma,max}$.

Condition **I** is a constraint on the total resolved dissipation positiveness, while condition **II** fixes a maximum value on $|C_\sigma|$.

Notice that neither problem (2.9) nor (2.11) are explicitly solved. Thus, most of the computational effort of the dynamic LES model remain the solution of the NS problem (2.7).

2.6 Grid filtering and test filter

The framework of homogeneous isotropic filters is the one in which subgrid modeling, detailed in Section 2.4, has been developed.

We recall that homogeneous means that the filter is characterized by a constant cutoff scale in all directions of space, and isotropic means that filter properties are independent of the position and orientation of the frame of reference in space.

However, the use of homogeneous isotropic filters is unpractical in real applications, where the fluid domain is bounded. Hence, we need filters that are local in space in order to take the boundaries into account.

Anyway, the filtering procedure is not performed explicitly because the fields $\mathbf{u}$ and p, being the solution, are not known. Therefore, the application of the filter is only formal.

In this thesis, we considered an implicit filtering procedure, given by the solution of the fluid equations on a mesh[10] (named grid filtering). Therefore, $\overline{\Delta}$ represents the size of the mesh. This empirical choice was first proposed by Deardorff [31] and it is the most widely used today. Therefore, the $\overline{\Delta}$ filter, the computational mesh, made a sort of spatial "sampling" of the variable up to a certain scale. This is similar to a cutoff filter that eliminates the higher spatial frequencies (see Figure 2.6a).

To obtain the expression of an effective constant C_σ in the dynamic procedure (see Section 2.5.2) we have used the so called test filter, fully detailed in [48]. In particular, this filter is based on

i) computing the average velocity $\mathbf{w}$ of the grid-filtered velocity $\overline{\mathbf{u}}$ in each mesh element (tetrahedra in our case),

ii) assigning to each node $\mathbf{x}_i$ of the mesh the velocity field $\widetilde{\overline{\mathbf{u}}}$ obtained by averaging the values $\mathbf{w}$ related to the tetrahedra that share $\mathbf{x}_i$. The characteristic length $\widetilde{\Delta}$ related to this geometric filter is equal to the cubic roots of the sum of the volumes of the tetrahedron sharing the node $\mathbf{x}_i$.

[10] We will detail the process of meshes building in Chapter 5.

Chapter 3

Numerical methods

We use the finite element method (FEM) to numerically solve the Navier-Stokes equations. For the sake of exposition, we report again the strong formulation of the modeled filtered Navier-Stokes equations for a general hemodynamic problem (2.7):

Find velocity $\mathbf{u}$ and pressure p such that

$$\frac{\partial \mathbf{u}}{\partial t} + (\mathbf{u}\cdot\nabla)\mathbf{u} + \nabla p - 2\nu\nabla\cdot\mathbf{S}(\mathbf{u}) + \nabla\cdot\boldsymbol{\tau}_d^{sgs} = \mathbf{0} \qquad \text{in } \Omega\times(0,T]\,, \quad (3.1a)$$

$$\nabla\cdot\mathbf{u} = 0 \qquad \text{in } \Omega\times(0,T]\,, \quad (3.1b)$$

$$\mathbf{u} = \mathbf{u}_{in}(Q_{in}) \qquad \text{on } \Gamma_{in}\times(0,T]\,, \quad (3.1c)$$

$$(-p\mathbf{I} + 2\nu\mathbf{S}(\mathbf{u}) - \boldsymbol{\tau}_d^{sgs})\,\hat{\mathbf{n}} = \mathbf{0} \qquad \text{on } \Gamma_{outs}\times(0,T]\,, \quad (3.1d)$$

$$\mathbf{u} = \mathbf{0} \qquad \text{on } \Gamma_{wall}\times(0,T]\,, \quad (3.1e)$$

$$\mathbf{u}(\mathbf{x},0) = \mathbf{u}_0(\mathbf{x}) \qquad \text{in } \Omega\times\{0\}\,, \quad (3.1f)$$

where, for the sake of clearness, we neglected the filtering operation in the rest of this Section. In addition, for the LES σ-model we have

$$\boldsymbol{\tau}_d^{sgs}(\mathbf{u}) = -2\nu_{sgs}^{\sigma}(\mathbf{u})\mathbf{S}(\mathbf{u}),$$

$$\nu_{sgs}^{\sigma}(\mathbf{u}) = C_\sigma\overline{\Delta}^2\beta(\mathbf{u}) \qquad \beta(\mathbf{u}) = \frac{\sigma_3(\sigma_1-\sigma_2)(\sigma_2-\sigma_3)}{\sigma_1^2}(\mathbf{u}),$$

where C_σ can be fixed *a priori* (static - σ), or computed during the simulation (dynamic - σ) through the Germano dynamic procedure.

3.1 Weak formulation

The weak formulation [49] of the governing equations (3.1) is obtained by multiplying equations (3.1a) and (3.1b) by test functions $\mathbf{v}$ and q, respectively, belonging to suitable function spaces (that we will specify later on), and integrating these equation all over the fluid domain Ω. As a consequence:

$$\begin{aligned}
&\int_\Omega \frac{\partial \mathbf{u}}{\partial t} \cdot \mathbf{v}\, d\Omega + \int_\Omega (\mathbf{u}\cdot\nabla)\mathbf{u}\cdot\mathbf{v}\, d\Omega + \int_\Omega \nabla p \cdot \mathbf{v}\, d\Omega + \\
&- \int_\Omega 2\nu\nabla\cdot\mathbf{S}(\mathbf{u})\cdot\mathbf{v}\, d\Omega - \int_\Omega 2\nabla\cdot[\nu^\sigma_{sgs}(\mathbf{u})\mathbf{S}(\mathbf{u})]\cdot\mathbf{v}\, d\Omega = 0, \\
&\int_\Omega \nabla\cdot\mathbf{u}\, q\, d\Omega = 0.
\end{aligned}$$

By summing up the two equations and performing integration by parts for pressure (∇p), viscous ($\nabla\cdot\mathbf{S}(\mathbf{u})$), and eddy viscosity turbulent ($\nabla\cdot[\nu^\sigma_{sgs}(\mathbf{u})\mathbf{S}(\mathbf{u})]$) terms, we get

$$\begin{aligned}
&\int_\Omega \frac{\partial \mathbf{u}}{\partial t} \cdot \mathbf{v}\, d\Omega + \int_\Omega (\mathbf{u}\cdot\nabla)\mathbf{u}\cdot\mathbf{v}\, d\Omega + \\
&+ \int_\Omega \nabla\cdot\mathbf{u}\, q\, d\Omega - \int_\Omega p\nabla\cdot\mathbf{v}\, d\Omega + \int_{\partial\Omega} p\mathbf{v}\cdot\hat{\mathbf{n}}\, d\Gamma + \\
&+ \int_\Omega 2\nu\mathbf{S}(\mathbf{u}) : \nabla\mathbf{v}\, d\Omega - \int_{\partial\Omega} 2\nu\mathbf{S}(\mathbf{u})\cdot\mathbf{v}\cdot\hat{\mathbf{n}}\, d\Gamma + \\
&+ \int_\Omega 2\nu^\sigma_{sgs}(\mathbf{u})\mathbf{S}(\mathbf{u}) : \nabla\mathbf{v}\, d\Omega - \int_{\partial\Omega} 2\nu^\sigma_{sgs}(\mathbf{u})\mathbf{S}(\mathbf{u})\cdot\mathbf{v}\cdot\hat{\mathbf{n}}\, d\Gamma = 0.
\end{aligned}$$

Regarding the choice of the function spaces, it's enough that p and q, $\mathbf{u}$ and $\mathbf{v}$, and their derivative, $\nabla\mathbf{u}$ and $\nabla\mathbf{v}$ are square-integrable functions in order to have sense in the integrals that appear in the above formulation. Hence, we defined

$$\mathcal{Q} = L^2(\Omega) = \{q \in \Omega \text{ s.t. } \|q\|_{L^2} = \sqrt{\int_\Omega |q|^2\, d\Omega} < \infty\},$$

$$\mathcal{V} = \{\mathbf{v} \in [L^2(\Omega)]^3 \text{ and } \nabla\mathbf{v} \in [L^2(\Omega)]^{3\times 3},\ \mathbf{v}|_{\Gamma_{in}} = \mathbf{u}_{in},\ \mathbf{v}|_{\Gamma_{wall}} = \mathbf{0}\}.$$

$$\mathcal{V}_0 = \{\mathbf{v} \in \mathcal{V} \text{ s.t. } \mathbf{v}|_{\Gamma_D} = \mathbf{0}\},$$

where $\Gamma_D = \Gamma_{in} \cup \Gamma_{wall}$. Because we want to prescribe the solution function $\mathbf{u}$ on the Dirichlet boundaries, we have to choose the test function to be zero on Γ_D, $\mathbf{v}|_{\Gamma_D} = \mathbf{0}$.

Having specified the function spaces $\mathcal{V}$, $\mathcal{V}_0$ and $\mathcal{Q}$, and by applying the boundary conditions (3.1c), (3.1d), (3.1e), the boundary terms vanish. Indeed, by rewriting the boundary terms as

$$\int_{\Gamma_D \cup \Gamma_N} p\mathbf{v} \cdot \hat{\mathbf{n}}\, d\Gamma + \int_{\Gamma_D \cup \Gamma_N} [-2\nu S(\mathbf{u}) - 2\nu^{\sigma}_{sgs}(\mathbf{u})\mathbf{S}(\mathbf{u})] \cdot \mathbf{v} \cdot \hat{\mathbf{n}}\, d\Gamma,$$

where $\partial\Omega = \Gamma_D \cup \Gamma_N$ with $\Gamma_D = \Gamma_{in} \cup \Gamma_{wall}$ and $\Gamma_N = \Gamma_{outs}$. The integral terms with Γ_D vanish because $\mathbf{v}|_{\Gamma_D} = \mathbf{0}$. The term

$$\int_{\Gamma_{outs}} [p\mathbf{I} - 2\nu S(\mathbf{u}) - 2\nu^{\sigma}_{sgs}(\mathbf{u})\mathbf{S}(\mathbf{u})] \cdot \mathbf{v} \cdot \hat{\mathbf{n}}\, d\Gamma,$$

also vanishes thanks to (3.1d).

The weak formulation of the modeled filtered Navier-Stokes equations for a general hemodynamic problem 3.1 reads:

Find, for all $t \in (0, T]$, $(\mathbf{u}, p) \in \{\mathcal{V} \times \mathcal{Q}\}$, such that

$$\left(\frac{\partial \mathbf{u}}{\partial t}, \mathbf{v}\right) + c(\mathbf{u}, \mathbf{u}, \mathbf{v}) + b(\mathbf{u}, q) - b(\mathbf{v}, p) + a(\mathbf{u}, \mathbf{v}) + g(\mathbf{u}, \mathbf{u}, \mathbf{v}) = 0$$

$$\forall \mathbf{v} \in \mathcal{V}_0 \quad , \quad \forall q \in \mathcal{Q}, \tag{3.2}$$

with $\mathbf{u}|_{t=0} = \mathbf{u}_0$, where

$$\left(\frac{\partial \mathbf{u}}{\partial t}, \mathbf{v}\right) := \int_{\Omega} \frac{\partial \mathbf{u}}{\partial t} \cdot \mathbf{v}\, d\Omega,$$

$$b(\mathbf{u}, q) := \int_{\Omega} \nabla \cdot \mathbf{u}\, q\, d\Omega,$$

$$a(\mathbf{u}, \mathbf{v}) := \int_{\Omega} 2\nu \mathbf{S}(\mathbf{u}) : \nabla \mathbf{v}\, d\Omega,$$

and

$$c(\mathbf{w}, \mathbf{u}, \mathbf{v}) := \int_{\Omega} (\mathbf{w} \cdot \nabla)\mathbf{u} \cdot \mathbf{v}\, d\Omega,$$

$$g(\mathbf{w}, \mathbf{u}, \mathbf{v}) := \int_{\Omega} 2\nu^{\sigma}_{sgs}(\mathbf{w})\mathbf{S}(\mathbf{u}) : \nabla \mathbf{v}\, d\Omega.$$

The weak formulation reduces the space derivation order of the solution. We moved from a second order differential problem (the strong formulation) to a first order problem in integral form (the weak formulation), which allows to treat less regular data. It can be proved that there is an equivalence, in the sense of distribution, between the weak formulation and the strong one [49].

3.2 Galerkin formulation

In order to solve the problem numerically, we first perform a space discretization of the weak formulation (3.2).

Let us consider a triangulation Ω_h, composed by tetrahedra $\mathcal{T}_i$, with $i = 1, ..., N_\mathcal{T}$ (where $N_\mathcal{T}$ is the total number of tetrahedra), of the domain Ω

$$\Omega \approx \Omega_h = int\left(\bigcup_{i=1}^{N_\mathcal{T}} \mathcal{T}_i\right),$$

where $int(A)$ indicates the internal part of a domain A. We denoted the refining level of triangulation as

$$h = \max_{\mathcal{T}\in\mathcal{T}_h} h_\mathcal{T},$$

where $h_\mathcal{T}$ is a characteristic length of the element $\mathcal{T}$ of the triangulation.

Introducing two families of finite-dimensional sub-spaces $\mathcal{V}_h$ and $\mathcal{Q}_h$, approximations of $\mathcal{V}$ and $\mathcal{Q}$ respectively, and depending on a discretization parameter h, with $\dim \mathcal{V}_h = N_V$ and $\dim \mathcal{Q}_h = N_Q$,

$$\mathcal{V}_h \subset \mathcal{V} \qquad \mathcal{Q}_h \subset \mathcal{Q},$$

the space discretization of the weak formulation (3.2) reads:

Find, for all $t \in (0, T]$, $(\mathbf{u}_h, p_h) \in \{\mathcal{V}_h \times \mathcal{Q}_h\}$, such that

$$\left(\frac{\partial \mathbf{u}_h}{\partial t}, \mathbf{v}_h\right) + c(\mathbf{u}_h, \mathbf{u}_h, \mathbf{v}_h) + b(\mathbf{u}_h, q_h) - b(\mathbf{v}_h, p_h) + a(\mathbf{u}_h, \mathbf{v}_h) + g(\mathbf{u}_h, \mathbf{u}_h, \mathbf{v}_h) = 0$$

$$\forall \mathbf{v}_h \in \mathcal{V}_{0h} \quad , \quad \forall q_h \in \mathcal{Q}_h, \tag{3.3}$$

with $\mathbf{u}_h|_{t=0} = \mathbf{u}_{h,0}$, where $\mathbf{u}_{h,in}$ and $\mathbf{u}_{h,0}$ are approximations of $\mathbf{u}_{in}$ and $\mathbf{u}_0$, respectively (for example, their interpolants), and as usual $\mathcal{V}_{0h} = \{\mathbf{v}_h \in \mathcal{V}_h \text{ s.t. } \mathbf{v}_h|_{\Gamma_D} = \mathbf{0}\}$.

The (3.3) is the discretized-in-space Galerkin problem of (3.2).

3.2.1 Finite Element formulation

Let's define the finite element (FE) spaces of continuous functions, X_h^r (polynomials of degree r on each element $\mathcal{T}_i$ of the triangulation) as

$$X_h^r = \{v_h \in C^0(\overline{\Omega}) : v_h|_{\mathcal{T}_i} \in \mathbb{P}_r \ \forall \mathcal{T}_i \in \Omega_h\} \qquad r = 0, 1, 2, ...,$$

where, $\mathbb{P}_r$ is the space of polynomials of degree less than or equal to r.

We introduce the finite element formulation, as a specific Galerkin problem, choosing in (3.3) $\mathcal{V}_h$ and $\mathcal{Q}_h$ as

$$\mathcal{V}_h \equiv [X_h^r]^3 \qquad \mathcal{Q}_h \equiv X_h^s \qquad\qquad r, s \in \mathbb{N}.$$

The FE spaces $\mathcal{V}_h$ and $\mathcal{Q}_h$ need to satisfy the well known inf-sup (or LBB) condition [50]:

$$\exists \beta_h > 0 \ \ s.t. \ \ \inf_{q_h \in \mathcal{Q}_h} \sup_{\mathbf{v}_h \in \mathcal{V}_h} \frac{b(q_h, \mathbf{v}_h)}{\|\mathbf{v}_h\|_{H^1} \|q_h\|_{L^2}} \geq \beta_h \qquad \forall h > 0, \qquad (3.4)$$

with $\beta_h > 0$, and independent of the mesh size h. This property is necessary for the well posedness of the discrete problem and the optimal convergence of the method.

Examples of FE spaces satisfying (3.4) are the so named Taylor-Hood pair $\mathbb{P}_{k+1} - \mathbb{P}_k$ (with $k \geq 1$), where it can be noticed that the velocity space $\mathcal{V}_h$ has to be, in some sense, "richer" in comparison to the pressure space $\mathcal{Q}_h$. Indeed, the inf-sup condition couples the space $\mathcal{V}_h$ and $\mathcal{Q}_h$, and it is a sort of compatibility condition between the velocity and pressure spaces.

The equal order finite elements, $\mathbb{P}_k - \mathbb{P}_k$ ($\forall k$), do not satisfy the inf-sup condition and leads to instability on the discrete pressure (also called spurious pressure). However, $\mathbb{P}_k - \mathbb{P}_k$ can still be used with additional stabilization terms such as Streamline Upwind Petrov-Galerkin with a Pressure-Stabilizing Petrov-Galerkin term (SUPG-PSPG) [51, 52]. We will detail this stabilization procedure in Section 3.4.

In order to derive the algebraic formulation of (3.3) we have to explain the two basis for the discrete spaces $\mathcal{V}_h$ and $\mathcal{Q}_h$

$$\{\boldsymbol{\phi}_i(\mathbf{x})\}_{i=1}^{N_V} \qquad \{\psi_k(\mathbf{x})\}_{k=1}^{N_Q},$$

in order to expand our variables as

$$\mathbf{u}_h = \sum_{j=1}^{N_V} U_j(t)\boldsymbol{\phi}_j(\mathbf{x}), \qquad\qquad q_h = \sum_{l=1}^{N_Q} P_l(t)\psi_l(\mathbf{x}).$$

The coefficients, $U_j(t)$ $(j = 1, ..., N_V)$ and $P_l(t)$ $(l = 1, ..., N_Q)$ are called degrees of freedom of the finite element for the velocity and pressure field, respectively. The dimension of the FE spaces, N_V and N_Q, is the number of d.o.f, of the velocity and pressure field, respectively. Hence, the total number of d.o.f $N_{d.o.f}$[1] is

$$N_{d.o.f} = N_V + N_Q.$$

Since the problem (3.3) holds for all elements of the space $\mathcal{V}_h$ and $\mathcal{Q}_h$, then it is valid also for the basis. Hence, choosing these basis functions as test functions in (3.3), and using bilinearity of $a(.,.)$ and $b(.,.)$, and trilinearity of $c(.,.,.)$ and $g(.,.,.)$, we obtained the following system of Ordinary Differential Equations (ODEs):

$$\begin{cases} M\dfrac{d\mathbf{U}}{dt} + A\mathbf{U} + C(\mathbf{U})\mathbf{U} + G(\mathbf{U})\mathbf{U} + B^T\mathbf{P} = 0 \\ B\mathbf{U} = 0 \end{cases}, \tag{3.5}$$

where $M \in \mathbb{R}^{N_V \times N_V}$, $A \in \mathbb{R}^{N_V \times N_V}$, $C(\mathbf{U}) \in \mathbb{R}^{N_V \times N_V}$, $G(\mathbf{U}) \in \mathbb{R}^{N_V \times N_V}$, and $B \in \mathbb{R}^{N_Q \times N_V}$ are matrices whose elements are given by

$$M_{ij} = \int_\Omega \boldsymbol{\phi}_j \cdot \boldsymbol{\phi}_i d\Omega$$

$$A_{ij} = a(\boldsymbol{\phi}_j, \boldsymbol{\phi}_i)$$
$$C_{ij}(\mathbf{u}(t)) = c(\mathbf{u}(t), \boldsymbol{\phi}_j, \boldsymbol{\phi}_i),$$
$$G_{ij}(\mathbf{u}(t)) = g(\mathbf{u}(t), \boldsymbol{\phi}_j, \boldsymbol{\phi}_i),$$
$$B_{kj} = b(\boldsymbol{\phi}_j, \psi_k),$$

and $\mathbf{U}$ and $\mathbf{P}$ are the unknown vectors

$$\mathbf{U} = \Big(U_1(t), ..., U_{N_V}(t)\Big)^T, \qquad \mathbf{P} = \Big(P_1(t), ..., P_{N_Q}(t)\Big)^T.$$

Problem (3.5)is completed by an initial condition on the velocity

$$\mathbf{U}(0) = \mathbf{U}_0.$$

[1] We stress that this is the same parameter that we used in Section 2.2 to introduce the turbulence modeling.

3.3 Time discretization

Time discretization of the Galerkin problem (3.3) was performed by using the second order Backward Differentiation Formula (BDF2), that is an implicit second order multistep method (see [53, 54]).

First of all, we uniformly divided the finite time interval $[0, T]$, where $T = N_c T_{hb}$ with T_{hb} the period of the cardiac cycle and N_c the total number of cycles, into N_t step of size δt (time step)

$$t_n = n\delta t, \quad n = 0, 1, 2, ..., N_t \qquad N_t = \frac{T}{\delta t}.$$

For a general function z, we denoted z^n as the approximation of $z(t_n)$. Thus, the BDF2 approximation of the time derivative in (3.3) results:

$$\left(\frac{\partial \mathbf{u}_h}{\partial t}\right)^{n+1} \simeq \frac{3\mathbf{u}_h^{n+1} - 4\mathbf{u}_h^n + \mathbf{u}_h^{n-1}}{2\delta t} \qquad \text{for } n \geq 1$$

So, the discretized in time and space FEM Galerkin problem for the generic hemodynamic problem (3.3) is:

Find, for $n = 0, 1, ..., N_t - 1$, $(\mathbf{u}_h^{n+1}, p_h^{n+1}) \in \{\mathcal{V}_h \times \mathcal{Q}_h\}$, such that

$$\left(\frac{3\mathbf{u}_h^{n+1} - 4\mathbf{u}_h^n + \mathbf{u}_h^{n-1}}{2\delta t}, \mathbf{v}_h\right) + c(\mathbf{u}_h^*, \mathbf{u}_h^{n+1}, \mathbf{v}_h) + b(\mathbf{u}_h^{n+1}, q_h) - b(\mathbf{v}_h^{n+1}, p_h) + g(\mathbf{u}_h^*, \mathbf{u}_h^{n+1}, \mathbf{v}_h) + a(\mathbf{u}_h^{n+1}, \mathbf{v}_h) = 0,$$

$$\forall \mathbf{v}_h \in \mathcal{V}_{0h} \quad , \quad \forall q_h \in \mathcal{Q}_h, \tag{3.6}$$

with $\mathbf{u}_h^0 = \mathbf{u}_{h,0}$, and u_h^* is a quantity that we will specify in what follows.

The main issue of a fully implicit method is that the resulting problem is still non linear, due to the convective, $c(\mathbf{u}_h^*, \mathbf{u}_h^{n+1}, \mathbf{v}_h)$, and the turbulent eddy-viscosity, $g(\mathbf{u}_h^*, \mathbf{u}_h^{n+1}, \mathbf{v}_h)$, terms in (3.6). Indeed, if we put $u_h^* = u_h^{n+1}$, this choice leads us to solve a non linear system[2] with an huge computational cost. In order to reduce this cost, we use a semi-implicit approach with a second order extrapolation for the velocity, $\mathbf{u}_h^*$, in the convective and eddy-viscosity terms (as suggested in [49])

$$\mathbf{u}_h^* = 2\mathbf{u}_h^n - \mathbf{u}_h^{n-1}. \tag{3.7}$$

[2]For example, we can solve this system with Newton or Fixed point algorithm.

Accordingly, time discretization of the finite element approximation of the ODEs system (3.5) is

$$\begin{cases} M\dfrac{3\mathbf{U}^{n+1}-4\mathbf{U}^{n}+\mathbf{U}^{n-1}}{2\delta t} & +A\mathbf{U}^{n+1}+C(\mathbf{U}^{*})\mathbf{U}^{n+1}+ \\ & +G(\mathbf{U}^{*})\mathbf{U}^{n+1}+B^{T}\mathbf{P}^{n+1}=\mathbf{0}\,, \\ B\mathbf{U}^{n+1}=\mathbf{0} & \end{cases} \tag{3.8}$$

where $\mathbf{U}^{*}=2\mathbf{U}^{n}-\mathbf{U}^{n-1}$. With this semi-implicit treatment the trilinear term $c(.,.,.)$ and $g(.,.,.)$ become bilinear, and the corresponding matrices are

$$C_{ij}=c(\mathbf{u}^{*},\boldsymbol{\phi}_j,\boldsymbol{\phi}_i)=\int_{\Omega}(\mathbf{u}^{*}\cdot\nabla)\boldsymbol{\phi}_j\cdot\boldsymbol{\phi}_i\,d\Omega,$$

$$G_{ij}=g(\mathbf{u}^{*},\boldsymbol{\phi}_j,\boldsymbol{\phi}_i)=\int_{\Omega}2\nu_{sgs}^{\sigma}(\mathbf{u}^{*})\mathbf{S}(\boldsymbol{\phi}_j):\nabla\boldsymbol{\phi}_i\,d\Omega.$$

The (3.8) is now a linear system, that can be written in a single monolithic matrix (Σ, also called monolithic NS matrix) form

$$\begin{bmatrix} K & B^{T} \\ B & 0 \end{bmatrix}\begin{bmatrix} \mathbf{U}^{n+1} \\ \mathbf{P}^{n+1} \end{bmatrix}=\begin{bmatrix} \frac{1}{2\delta t}M(4\mathbf{U}^{n}-\mathbf{U}^{n-1}) \\ \mathbf{0} \end{bmatrix},\qquad \Sigma=\begin{bmatrix} K & B^{T} \\ B & 0 \end{bmatrix}. \tag{3.9}$$

where

$$K=\frac{3}{2\delta t}M+A+C(U^{*})+G(U^{*}).$$

The non-symmetric linear system (3.9) can be solved by a Krylov method, e.g. the GMRES method. However, due to the undefiniteness monolithic matrix we have a slow convergence (see [55]). To speed up convergence, the use of preconditioner is mandatory. We will use the Additive Schwarz Preconditioner [56, 57].

For this semi-implicit scheme the stability condition is

$$\delta t\leq C\frac{h}{\max\limits_{\mathbf{x}\in\Omega}\|\mathbf{u}_h\|}, \tag{3.10}$$

where $C\in\mathbb{R}^{+}$.

The semi-implicit is a compromise between a completely explicit scheme which has a stricter stability condition of the type

$$\delta t\leq C\min\left(\frac{h^{2}}{\nu},\frac{h}{\max\limits_{\mathbf{x}\in\Omega}\|\mathbf{u}_h\|}\right),$$

and a completely implicit BDF2 scheme which is unconditionally stable [10, 58].

However, in hemodynamic problem, the constraint (3.10) is mild, since δt, for accuracy purposes, should be typically taken smaller than the required by the previous condition.

3.4 SUPG-PSPG stabilization

Navier-Stokes equations with finite element formulation suffer from two source of numerical instability, due to the fact that:

I NS is a convection dominated problem, which means "large" Re (as in the aorta during the systolic phase), where numerical oscillations in the velocity field can occur (spurious velocity);

II FE spaces $\mathbb{P}_k - \mathbb{P}_k$ $(\forall k)$ are unstable combinations of velocity and pressure finite element spaces, that do not satisfy the inf-sup condition (3.4), and generates numerical oscillations in the pressure field (spurious pressure).

In order to have a global second order convergence rate[3]

$$\|\mathbf{u}_h^{n+1} - \mathbf{u}(t^{n+1})\|_{H^1(\Omega)} \sim O(h^2) + O(\delta t^2),$$

we used a BDF2 semi-implicit approach for the time discretization, in combination with a $\mathbb{P}_2 - \mathbb{P}_2$ Finite Elements, that is piece-wise quadratic polynomials, for the space approximation of the velocity and each pressure component.

$\mathbb{P}_2 - \mathbb{P}_2$ FE spaces are inf-sup unstable. So, to control instabilities arising from inf-sup condition and convection dominated problem, Pressure-Stabilizing Petrov-Galerkin(PSPG) stabilization along with Streamline-Upwind Petrov-Galerkin (SUPG) stabilization were added to the problem (3.6), respectively [51].

The SUPG-PSPG stabilization consists in adding a series of terms to the formulation (3.6), involving the product of the residual of the strong formulation of NS equations with its skew-symmetric part [60]

$$s_{LES}(\mathbf{u}_h^{n+1}, p_h^{n+1}; \mathbf{v}_h, q_h) = \gamma \sum_{\mathcal{T} \in \Omega_h} \tau_{\mathcal{T}} \int_{\mathcal{T}} \left[\mathcal{L}(\mathbf{u}_h^{n+1}, p^{n+1})\right]^T \mathcal{L}_{ss}(\mathbf{v}_h, q_h) d\mathcal{T},$$

[3]For an analysis of the numerical errors of a Finite Elements approximation in presence of a LES model, see [59].

where $\gamma > 0$ is a positive constant, $\tau_{\mathcal{T}}$ is the stabilization parameter (that will be specified later on), $\mathcal{T}$ is a generic tetrahedron belonging to the finite elements partitioned domain Ω_h, $\mathcal{L}(\mathbf{u}, p)$ is the residual of the NS equations (3.1a)-(3.1b)

$$\mathcal{L}(\mathbf{u}, p) = \begin{bmatrix} \frac{\partial \mathbf{u}}{\partial t} + (\mathbf{u} \cdot \nabla)\mathbf{u} + \nabla p - 2\nu \nabla \cdot \mathbf{S}(\mathbf{u}) - 2\nu_{sgs}(\mathbf{u}) \nabla \cdot \mathbf{S}(\mathbf{u}) \\ \nabla \cdot \mathbf{u} \end{bmatrix},$$

and $\mathcal{L}_{ss}(\mathbf{u}, p)$ is the skew-symmetric part[4] of the NS equations (3.1a)-(3.1b)

$$\mathcal{L}_{ss}(\mathbf{u}, p) = \begin{bmatrix} (\mathbf{u} \cdot \nabla)\mathbf{u} + \nabla p \\ \mathbf{0} \end{bmatrix}.$$

Since, it is based on the residual of the NS equations, the SUPG-PSPG is a strongly consistent stabilization [51].

The discretized finite element Galerkin formulation with SUPG-PSPG stabilization can be written as:

Find, for all $t = 0, 1, ..., N_t - 1$, $(\mathbf{u}_h^{n+1}, p_h^{n+1}) \in \{\mathcal{V}_h \times \mathcal{Q}_h\}$, such that

$$\left(\frac{3\mathbf{u}_h^{n+1} - 4\mathbf{u}_h^n + \mathbf{u}_h^{n-1}}{2\delta t}, \mathbf{v}_h \right) + c(\mathbf{u}_h^*, \mathbf{u}_h^{n+1}, \mathbf{v}_h) + b(\mathbf{u}_h^{n+1}, q_h) - b(\mathbf{v}_h, p_h^{n+1}) +$$
$$+ g(\mathbf{u}_h^*, \mathbf{u}_h^{n+1}, \mathbf{v}_h) + a(\mathbf{u}_h^{n+1}, \mathbf{v}_h) + s_{LES}(\mathbf{u}_h^{n+1}, p_h^{n+1}; \mathbf{v}_h, q_h) = 0$$
$$\forall \mathbf{v}_h \in \mathcal{V}_{0h} \quad , \quad \forall q_h \in \mathcal{Q}_h, \tag{3.11}$$

with $\mathbf{u}_h^0 = \mathbf{u}_{h,0}$, where

$$\begin{aligned} & s_{LES}(\mathbf{u}_h^{n+1}, p_h^{n+1}; \mathbf{v}_h, q_h) = \\ & = \gamma \sum_{\mathcal{T} \in \Omega_h} \tau_{M,\mathcal{T}} \left(\frac{3\mathbf{u}_h^{n+1} - 4\mathbf{u}_h^n + \mathbf{u}_h^{n-1}}{2\delta t} + (\mathbf{u}_h^* \cdot \nabla)\mathbf{u}_h^{n+1} + \nabla p_h^{n+1} + \right. \\ & \left. -2[\nu + \nu_{sgs}(\mathbf{u}_h^*)] \nabla \cdot \mathbf{S}(\mathbf{u}_h^{n+1}) \, , \, u_h^* \cdot \nabla \mathbf{v}_h + \frac{\nabla q_h}{\rho} \right)_{\mathcal{T}} + \\ & + \gamma \sum_{\mathcal{T} \in \Omega_h} \tau_{C,\mathcal{T}} \left(\nabla \cdot \mathbf{u}_h^{n+1}, \nabla \cdot \mathbf{v}_h \right)_{\mathcal{T}}, \end{aligned} \tag{3.12}$$

[4] The skew-symmetric part of a generic operator $\mathcal{L}(\mathbf{u}, p)$ is the one for which

$$\Big(\mathcal{L}(\mathbf{u}, p), (\mathbf{v}, q) \Big) = - \Big((\mathbf{v}, q), \mathcal{L}(\mathbf{u}, p) \Big).$$

and $\tau_{M,\mathcal{T}}$, and $\tau_{C,\mathcal{T}}$ are two stabilization parameters for the momentum and the continuity NS equations, respectively. In addition, the notation $(a, b)_{\mathcal{T}} = \int_{\mathcal{T}} ab\, d\mathcal{T}$ has been introduced, and $\mathbf{u}_h^*$ was defined in agreement to (3.7).

In the previous expression of s_{LES} (3.12), the term

$$\sum_{\mathcal{T}\in\Omega_h} \tau_{M,\mathcal{T}} \left(\nabla p_h^{n+1}, \frac{\nabla q_h}{\rho} \right)_{\mathcal{T}},$$

is the Brezzi-Pitkaranta stabilization for the inf-sup, while the term

$$\sum_{\mathcal{T}\in\Omega_h} \tau_{M,\mathcal{T}} \left(u_h^* \cdot \nabla \mathbf{u}_h^{n+1}, u_h^* \cdot \nabla \mathbf{v}_h \right)_{\mathcal{T}},$$

corresponds to the streamline diffusion term stabilization for large Re. The other terms in (3.12) occur to obtain a strongly consistent stabilization.

Regarding the choice of the stabilization parameters $\tau_{M,\mathcal{T}}$, and $\tau_{C,\mathcal{T}}$ we used

$$\tau_{M,\mathcal{T}} = \left(\frac{\sigma_{BDF}^2}{\delta t^2} + \frac{\|\mathbf{u}\|^2}{h_{\mathcal{T}}^2} + C_k \frac{(\nu + \nu_{sgs})^2}{h_{\mathcal{T}}^4} \right)^{-1/2}, \qquad \tau_{C,\mathcal{T}} = \frac{h_{\mathcal{T}}^2}{\tau_{M,\mathcal{T}}},$$

where: $C_k = 60 \cdot 2^{k-2}$ is a constant obtained by an inverse inequality relation (and k is the order of the chosen pair $\mathbb{P}_k - \mathbb{P}_k$); σ_{BDF} is a constant equal to the order of the time discretization; δt is the time step; $h_{\mathcal{T}}$ is the "element length" (e.g. the element diameter) of a generic tetrahedra belonging to the partitioned domain Ω_h [61]. $\tau_{M,\mathcal{T}}$ and $\tau_{C,\mathcal{T}}$ were obtained by a multidimensional generalization of the optimal value introduced in [62] for the one-dimensional case [64].

Notice that the terms added by the SUPG-PSPG stabilization 3.12 can be explicitly written as fallows

$$s_{11}^{(1)} = \left(\frac{3}{2} \frac{\mathbf{u}_h^{n+1}}{\delta t}, \mathbf{u}_h^* \cdot \nabla \mathbf{v}_h \right)_{\mathcal{T}}, \qquad s_{21}^{(1)} = \left(\frac{3}{2} \frac{\mathbf{u}_h^{n+1}}{\delta t}, \frac{\nabla q_h}{\rho} \right)_{\mathcal{T}},$$

$$s_{11}^{(2)} = \left(\mathbf{u}_h^* \cdot \nabla \mathbf{u}_h^{n+1}, \mathbf{u}_h^* \cdot \nabla \mathbf{v}_h \right)_{\mathcal{T}}, \qquad s_{21}^{(2)} = \left(\mathbf{u}_h^* \cdot \nabla \mathbf{u}_h^{n+1}, \frac{\nabla q_h}{\rho} \right)_{\mathcal{T}},$$

$$s_{11}^{(3)} = \left(-2(\nu + \nu_{sgs}(\mathbf{u}^*)) \nabla \cdot \mathbf{S}(\mathbf{u}_h^{n+1}), \mathbf{u}_h^* \cdot \nabla \mathbf{v}_h \right)_{\mathcal{T}},$$

$$s_{21}^{(3)} = \left(-2(\nu + \nu_{sgs}(\mathbf{u}^*)) \nabla \cdot \mathbf{S}(\mathbf{u}_h^{n+1}), \frac{\nabla q_h}{\rho} \right)_{\mathcal{T}},$$

$$s_{11}^{(4)} = \left(\nabla \cdot \mathbf{u}_h^{n+1}, \nabla \cdot \mathbf{v}_h \right)_{\mathcal{T}},$$

$$s_{12} = \left(\nabla p_h \,,\, \mathbf{u}_h^* \cdot \nabla \mathbf{v}_h\right)_{\mathcal{T}}, \qquad s_{22} = \left(\nabla p_h \,,\, \frac{\nabla q_h}{\rho}\right)_{\mathcal{T}},$$
$$f_v = \left(\frac{4\mathbf{u}_h^n - \mathbf{u}_h^{n-1}}{2\delta t} \,,\, \mathbf{u}_h^* \cdot \nabla \mathbf{v}_h\right)_{\mathcal{T}}, \qquad f_q = \left(\frac{4\mathbf{u}_h^n - \mathbf{u}_h^{n-1}}{2\delta t} \,,\, \frac{\nabla q_h}{\rho}\right)_{\mathcal{T}},$$

where, for the sake of clearness, the sum over the tetrahedra was omitted[5]. Moreover, the indices I, J in $s^{(n)}_{(I,J)}$ refer to the position of the corresponding term in the monolithic NS matrix, Σ (3.9), and n distinguishes the different terms inside each block,

$$\begin{bmatrix} \Sigma_{11} & \Sigma_{12} \\ \Sigma_{21} & \Sigma_{22} \end{bmatrix} \Longrightarrow \begin{bmatrix} s^{(1)}_{(11)} + s^{(2)}_{(11)} + s^{(3)}_{(11)} + s^{(4)}_{(11)} & s_{(12)} \\ s^{(1)}_{(21)} + s^{(2)}_{(21)} + s^{(3)}_{(21)} & s_{(22)} \end{bmatrix}, \tag{3.13}$$

while the corresponding vectors to f_v and f_q fill the RHS of the system (3.9).

The matrix elements corresponding to (3.13) are

$$[S^{(1)}_{11}]_{ij} = \frac{3}{2\delta t} \sum_{\mathcal{T}\in\Omega_h} \tau_{M,\mathcal{T}} \int_{\mathcal{T}} \boldsymbol{\phi}_j (\mathbf{u}_h^* \cdot \nabla)\boldsymbol{\phi}_i \, d\mathcal{T},$$

$$[S^{(2)}_{11}]_{ij} = \sum_{\mathcal{T}\in\Omega_h} \tau_{M,\mathcal{T}} \int_{\mathcal{T}} (\mathbf{u}_h^* \cdot \nabla)\boldsymbol{\phi}_j (\mathbf{u}_h^* \cdot \nabla)\boldsymbol{\phi}_i \, d\mathcal{T},$$

$$[S^{(3)}_{11}]_{ij} = -\sum_{\mathcal{T}\in\Omega_h} \tau_{M,\mathcal{T}} \int_{\mathcal{T}} (\nu + \nu_{sgs}(\mathbf{u}^*))\Delta\boldsymbol{\phi}_j (\mathbf{u}_h^* \cdot \nabla)\boldsymbol{\phi}_i \, d\mathcal{T},$$

$$[S^{(4)}_{11}]_{ij} = \sum_{\mathcal{T}\in\Omega_h} \tau_{C,\mathcal{T}} \int_{\mathcal{T}} \nabla\cdot\boldsymbol{\phi}_j \nabla\cdot\boldsymbol{\phi}_i \, d\mathcal{T},$$

$$[S^{(1)}_{21}]_{kj} = \frac{3}{2\delta t\rho} \sum_{\mathcal{T}\in\Omega_h} \tau_{M,\mathcal{T}} \int_{\mathcal{T}} \boldsymbol{\phi}_j \nabla\psi_k \, d\mathcal{T},$$

$$[S^{(2)}_{21}]_{kj} = \frac{1}{\rho} \sum_{\mathcal{T}\in\Omega_h} \tau_{M,\mathcal{T}} \int_{\mathcal{T}} (\mathbf{u}_h^* \cdot \nabla)\boldsymbol{\phi}_j \nabla\psi_k \, d\mathcal{T},$$

$$[S^{(3)}_{21}]_{kj} = -\frac{1}{\rho} \sum_{\mathcal{T}\in\Omega_h} \tau_{M,\mathcal{T}} \int_{\mathcal{T}} (\nu + \nu_{sgs}(\mathbf{u}^*))\Delta\boldsymbol{\phi}_j \nabla\psi_k \, d\mathcal{T},$$

$$[S_{12}]_{il} = \sum_{\mathcal{T}\in\Omega_h} \tau_{M,\mathcal{T}} \int_{\mathcal{T}} \nabla\psi_l (\mathbf{u}_h^* \cdot \nabla)\boldsymbol{\phi}_i \, d\mathcal{T},$$

[5] All the terms to be intended as $s^{(n)}_{(I,J)} = \sum_{\mathcal{T}\in\Omega_h} \tau_{\mathcal{T}} (\,.\,,\,.\,)_{\mathcal{T}}$.

$$[S_{22}]_{kl} = \frac{1}{\rho} \sum_{\mathcal{T} \in \Omega_h} \tau_{M,\mathcal{T}} \int_{\mathcal{T}} \nabla \psi_l \nabla \psi_k \, d\mathcal{T},$$

$$[F_v]_i = \sum_{\mathcal{T} \in \Omega_h} \tau_{M,\mathcal{T}} \int_{\mathcal{T}} \frac{4\mathbf{u}_h^n - \mathbf{u}_h^{n-1}}{2\delta t} (\mathbf{u}_h^* \cdot \nabla) \boldsymbol{\phi}_i \, d\mathcal{T},$$

$$[F_q]_k = \frac{1}{\rho} \sum_{\mathcal{T} \in \Omega_h} \tau_{M,\mathcal{T}} \int_{\mathcal{T}} \frac{4\mathbf{u}_h^n - \mathbf{u}_h^{n-1}}{2\delta t} \nabla \psi_k \, d\mathcal{T}.$$

Hence, the NS monolithic system with the SUPG-PSPG stabilization becomes

$$\begin{bmatrix} \Sigma & B^T + S_{12}^T \\ \widetilde{B} & S_{22} \end{bmatrix} \begin{bmatrix} \mathbf{U}^{n+1} \\ \mathbf{P}^{n+1} \end{bmatrix} = \begin{bmatrix} \frac{1}{2\delta t} M(4\mathbf{U}^n - \mathbf{U}^{n-1}) + \mathbf{F}_v \\ \mathbf{F}_q \end{bmatrix}, \tag{3.14}$$

where $\Sigma = K + \sum_{i=1}^{4} S_{11}^{(i)}$, and $\tilde{B} = B + \sum_{i=1}^{3} S_{21}^{(i)}$.

It is well known that SUPG-PSPG stabilization does not exhibit excessive numerical diffusion if at least second-order velocity elements and first-order pressure elements ($\mathbb{P}_2 - \mathbb{P}_1$) are used [62].

In LES the subgrid scales are represented by a physical model (see Section 3), which uses dissipation to include the effect of the small unresolved scales on the larger resolved scales. The numerical dissipation coming from the SUPG-PSPG is introduced for the purpose of achieving a stable, consistent and convergent discretization, and it can interfere with the dissipation related to these physical models. In particular, the SUPG-PSPG stabilization can be considered a numerical subgrid scale model.

To guarantee that LES models feature the same amount of dissipation independently of the SUPG stabilization, in [63] a correction of the subgrid-scale viscosity has been introduced for the Smagorinsky model in an open channel. We rather decided to follow [65] where no correction of the subgrid tensor was implemented. However, further investigations about this topic will deserve future studies.

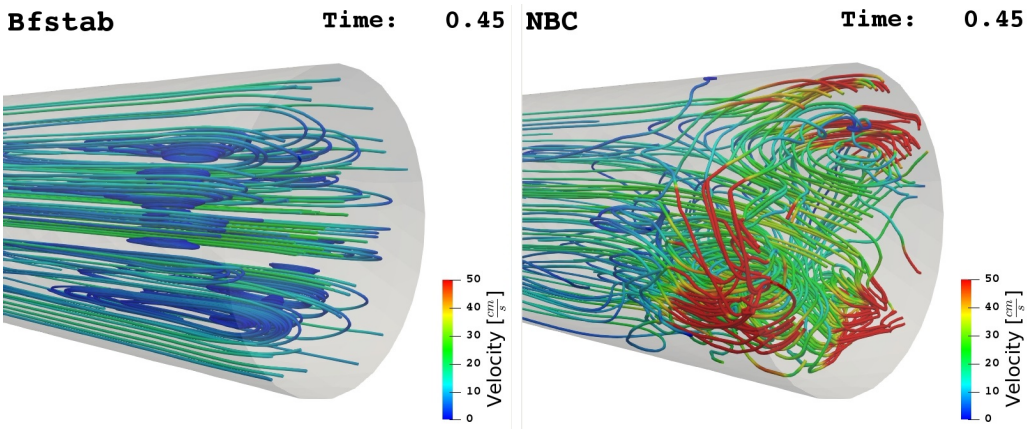

(a) Bfstab on outlet.

(b) NBC on outlet.

Figure 3.1: Backflow stabilization (Bfstab) versus Neumann Boundary Condition (NBC) on an outlet flow of a cylinder. We have imposed a parabolic (in space) and pulsatile (in time) inlet profile.

3.5 Backflow instabilities

As mentioned in Section 2.1, we imposed homogeneous Neumann boundary condition (3.1d) on the outlets of the domain, since we want to avoid prescribing a particular velocity profile on outlets. Indeed, due to the complex flow in the AAA, an assumption of the velocity field on the outlets would not be realistic. A drawback is that the Neumann boundary condition (NBC) suffers from numerical instability coming from backflow (see, for example, Figures 3.1b, 3.2b, 3.3b).

This problem can arise when there is an inward flow over the entire outlet surface, or also when flow partially reverses at an outlet. Flow reversal is present in both healthy and diseased cardiovascular system [66] (for example, during the diastole phase of the cardiac cycle). A partial retrograde flow can also be induced by recirculation caused by complex geometry near the outlets, or can be triggered also by the convection of vortices moving through the outlet. As a matter of fact, the outlet section is an "artificial" boundary of the fluid domain, which is truncated to focus on the region of interest.

When these phenomena occur, an outlet section becomes an inlet section, which is the cause of numerical instability. In fact, a general mixed boundary condition $\partial\Omega = \Gamma_N \cup \Gamma_D$[6], for the NS equations, leads to stable results

[6]Where, as usual, Γ_N and Γ_D indicate disjoint portions (i.e. $\mathring{\Gamma}_N \cap \mathring{\Gamma}_D = \emptyset$) of the boundary, $\partial\Omega = \Gamma_N \cup \Gamma_D$, where we impose Neumann and Dirichlet boundary condition, respectively.

only if

$$\mathbf{u}(\mathbf{x}) \cdot \widehat{\mathbf{n}} \geq 0, \quad \forall \mathbf{x} \in \Gamma_N,$$

where $\widehat{\mathbf{n}}$ indicates the outward normal unit vector to Γ_N, and $\mathbf{u}(\mathbf{x})$ is the velocity field on Γ_N.

The motivation for this numerical instabilities is that the system energy is not controlled in case of an incoming flux from a Neumann boundary. In fact, from a stability analysis[7] [67]

$$\frac{d}{dt}\int_\Omega \frac{1}{2}|\mathbf{u}|^2 d\Omega + (\nu + \nu_{sgs})\int_\Omega |\nabla \mathbf{u}|^2 d\Omega + \int_{\Gamma_{outs}} \frac{1}{2}|\mathbf{u}|^2 \mathbf{u}\cdot\widehat{\mathbf{n}}\, d\Gamma = 0,$$

from which, defining $E(t) = \int_\Omega \frac{1}{2}|\mathbf{u}|^2 d\Omega$, and $D(t) = (\nu + \nu_{sgs})\int_\Omega |\nabla \mathbf{u}|^2 d\Omega$, we obtain

$$\frac{d}{dt}E(t) = -D(t) - \int_{\Gamma_{outs}} \frac{1}{2}|\mathbf{u}|^2 \mathbf{u}\cdot\widehat{\mathbf{n}}\, d\Gamma. \tag{3.15}$$

In (3.15) $D(t)$ is always non-negative (i.e. always dissipative), while the last term can add energy in case of $\mathbf{u}\cdot\widehat{\mathbf{n}} \leq 0$ on Γ_{outs}, which correspond to an inward velocity on the outlet. So during partial backflow, the last term can lead to an uncontrolled energy increase [68].

Backflow stabilization

One way to resolve the backflow instability is to add a stabilization term to the Neumann boundary conditions (as proposed in [67, 68]).

This approach is referred to Backflow Stabilization [67] (Bfstab). It consists in suppressing the unstable term in equation (3.15) by modifying the Neumann boundary condition (3.1d):

$$(-p\mathbf{I} + 2\nu\mathbf{S}(\mathbf{u}) - \boldsymbol{\tau}_d^{sgs})\,\widehat{\mathbf{n}} = \beta \int_{\Gamma_{outs}} \frac{1}{2}|\mathbf{u}\cdot\widehat{\mathbf{n}}|_-\mathbf{u}\, d\Gamma \qquad \text{on } \Gamma_{outs}\times(0,T]\,,$$

where

$$|\mathbf{u}\cdot\widehat{\mathbf{n}}|_- = \frac{\mathbf{u}\cdot\widehat{\mathbf{n}} - |\mathbf{u}\cdot\widehat{\mathbf{n}}|}{2} = \begin{cases} \mathbf{u}\cdot\widehat{\mathbf{n}} & \text{for} \quad \mathbf{u}\cdot\widehat{\mathbf{n}} < 0 \\ 0 & \text{for} \quad \mathbf{u}\cdot\widehat{\mathbf{n}} \geq 0 \end{cases}.$$

This type of boundary condition is a non-linear Robin condition.

The stabilization term is active only where and when $\mathbf{u}\cdot\widehat{\mathbf{n}} < 0$ (i.e. where backflow is present - see, for example, Figures 3.1a, 3.2a, 3.3a).

This method can ensure a theoretical backflow stable simulation with a parameter $\beta = 1$, but it is often used with a value $\beta \in (0, 1]$. In physical

[7] Stability result can be obteined from the weak formulation (3.2) tested on the solution, i.e. putting $\mathbf{v} = \mathbf{u}$ in (3.2).

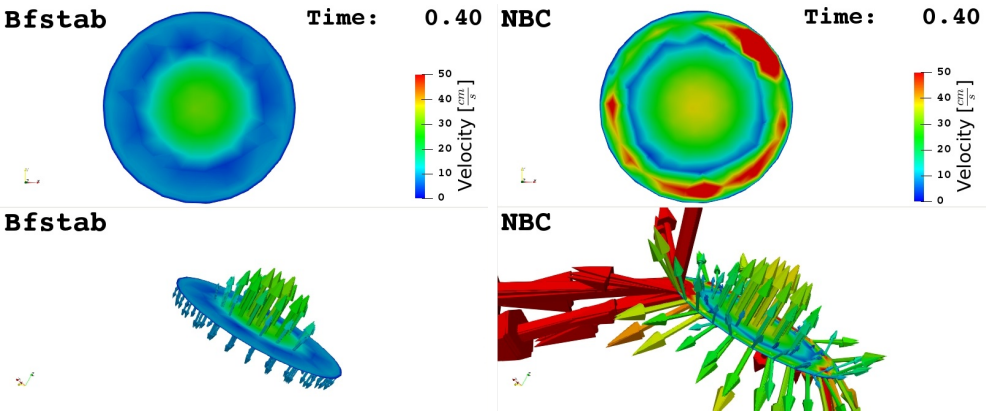

(a) Bfstab on outlet. (b) NBC on outlet.

Figure 3.2: Bfstab versus NBC on an outlet flow of a cylinder. Parabolic and pulsatile inlet profile.

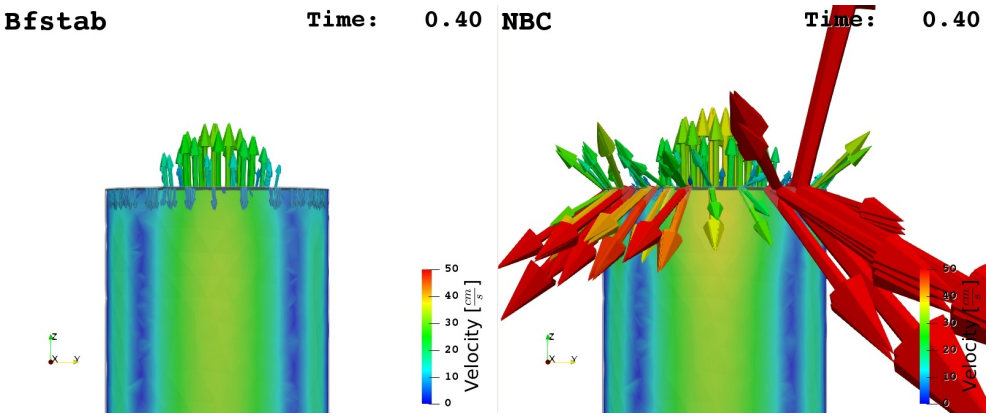

(a) Bfstab on outlet. (b) NBC on outlet.

Figure 3.3: Bfstab versus NBC on an outlet flow of a cylinder. Parabolic and pulsatile inlet profile.

terms, it is an outward traction proportional to the magnitude of the normal component of the backflow velocity.

In this thesis we used the backflow stabilization, implemented and studied in [69]. Indeed, this type of stabilization reveals to be effective in many cardiovascular and pulmonary applications [66, 70, 71].

3.6 Inlet defective boundary condition

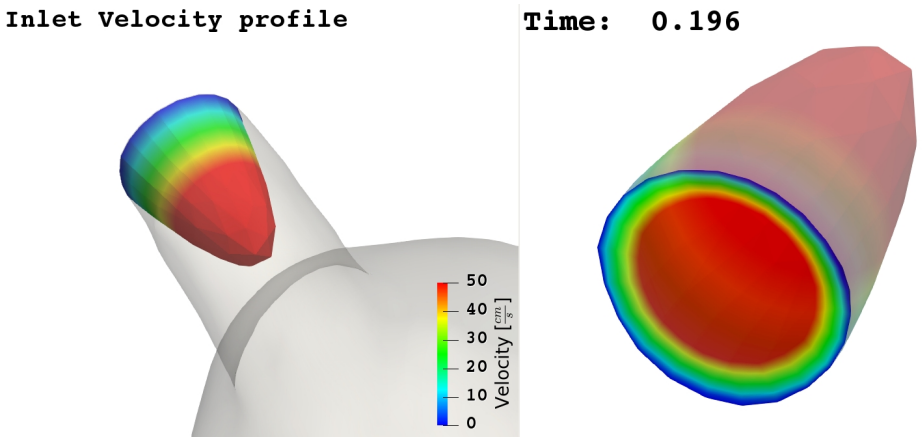

Figure 3.4: Velocity profile $\mathbf{u}_{in}$ at the inlet Γ_{in} during the first systolic peak.

In numerical simulation of blood flow problems, it might happen that the unique available boundary condition prescribe the flow rate incoming the vascular district at hand. In order to have a well posed NS problem, this condition needs to be completed. This problem is usually faced by choosing *a priori* velocity profile on the inflow section, to be fitted with the assigned flow rate [72].

In this thesis, at the inlet Γ_{in} (see Figure 2.2), we imposed a representative time variation of the flow rate $Q_{in}(t)$ shown in Figure 3.5. The flow rate is defined as

$$Q_{in}(t) = \int_{\Gamma_{in}} \mathbf{u}_{in}(t) \cdot \widehat{\mathbf{n}} \, d\Gamma, \tag{3.16}$$

where $\mathbf{u}_{in}(t)$ is the velocity profile at the inlet surface Γ_{in}, and $\widehat{\mathbf{n}}$ is the outward directed unit normal vector to Γ_{in}.

This is a defective boundary condition [72], since at each time step we are prescribing only a scalar quantity over the whole Γ_{in}, rather than three conditions for each point of the section. To fill this gap, we assumed a parabolic velocity profile $\mathbf{u}_{in}(t) = \left(u_{in}^{(x)}(t), u_{in}^{(y)}(t), u_{in}^{(z)}(t)\right)$, along the normal direction $\widehat{\mathbf{n}} = [n_x, n_y, n_z]$ (a common choise in heamodynamics, see for example [73])

$$\begin{cases} u_{in}^{(x)}(t) = -2\frac{Q_{in}(t)}{A}\left(1 - \frac{r^2}{R^2}\right) n_x \\ u_{in}^{(y)}(t) = -2\frac{Q_{in}(t)}{A}\left(1 - \frac{r^2}{R^2}\right) n_y \\ u_{in}^{(z)}(t) = -2\frac{Q_{in}(t)}{A}\left(1 - \frac{r^2}{R^2}\right) n_z \end{cases}, \tag{3.17}$$

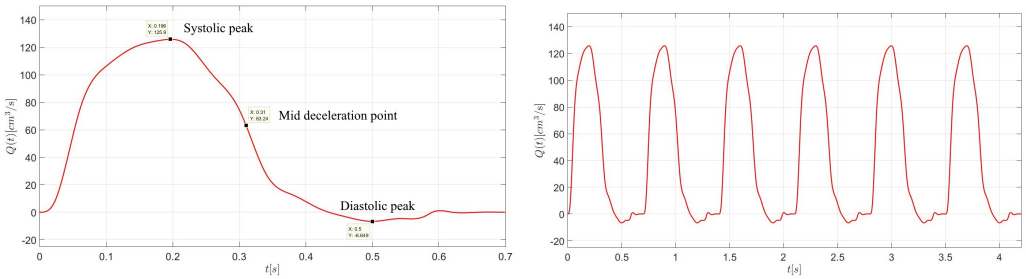

(a) $Q_{in}(t)$ in the first cardiac cycle. (b) $Q_{in}(t)$ for six cardiac cycles.

Figure 3.5: Inlet profile flow rate $Q_{in}(t)$.

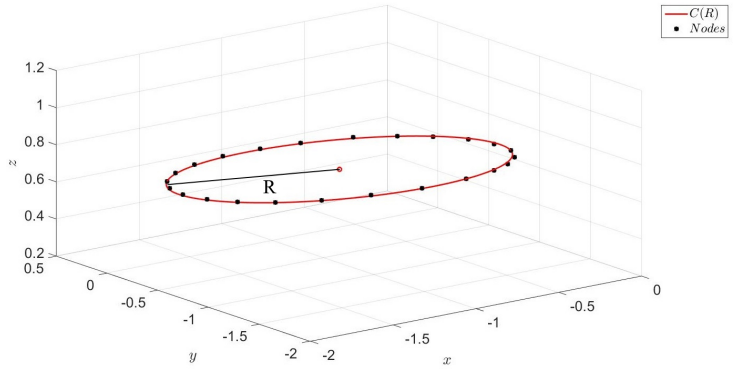

Figure 3.6: Circle $C(R)$ approximating the border surface Γ_{in}

where: $r \in \Gamma_{in}$, with $r = \sqrt{(x-x_0)^2+(y-y_0)^2+(z-z_0)^2}$ in which (x_0, y_0, z_0) are the center point coordinates of Γ_{in}; $A = \pi R^2$ is the area of the boundary surface Γ_{in}; R is the radius of the circle approximating the border surface Γ_{in} (see Figure 3.6).

Notice that $\mathbf{u}_{in}(t)$ is the unique function characterized by a parabolic profile in the normal direction $\widehat{\mathbf{n}}$, and vanishes in the tangential ones, whose flow rate at each time t, is equal to $Q_{in}(t)$.

Conditions (3.16) and (3.17) give us the Dirichlet condition 3.1c.

$$\mathbf{u} = \mathbf{u}_{in}(Q_{in}) \qquad \text{on } \Gamma_{in} \times (0, T] \,.$$

Moreover, no inlet perturbation is prescribed, so that the flow is assumed to be laminar at the inlet boundary. This will allow us to capture turbulence transitional effects arising as a consequence of geometry and pulsatility solely.

In the cardiac cycle, with period $T_{hb} = 0.7s$, we can distinguish the systolic phase, i.e. the interval of acceleration and deceleration of blood flow, and the diastolic phase, i.e. the interval of almost constant or negative flow (see Figure 3.5a).

The final part of the cardiac cycle has a null inlet flow rate, which allows the flow in the vessel to become nearly still. That supports the choice of a null initial condition 3.1f

$$\mathbf{u}(\mathbf{x}, 0) = \mathbf{u}_0(\mathbf{x}) = \mathbf{0} \qquad \text{in } \Omega \times \{0\} \, .$$

Chapter 4

Pre-processing and meshes building

As discussed in the Introduction, the aim of this thesis is to asses the reliability of LES σ-models in a specific hemodynamic scenario that is the AAA, where transitional to turbulence should not be neglected. To this aim we want to compare different numerical simulations obtained by these LES models with a DNS one. This comparison will be done in a real geometry of AAA. In this Chapter we address how we have build the meshes for LES and DNS simulations.

4.1 Geometrical data and boundary conditions

To obtain realistic results, patient specific data are used, in particular the AAA geometry and the waveform of the flow entering in the aneurysm.

The aorta geometry data were acquired using a computed tomography (CT) scan performed by the Vascular Surgery Division of the Ca' Granda Ospedale Maggiore Policlinico in Milano.

In particular, the acquisition images start from the thoracic segment of the aorta till the first track of the common Iliac arteries. The surface model of the arterial wall was reconstructed with the Vascular Modeling Toolkit, VMTK [76][1]. Figure 4.1 shows VMTK geometry taken from a patient of [74].

Observing the Figure 4.1, this segment of aorta includes a fusiform aneurysm (see Figure 1.10) with a diameter of about 4.2 cm, against a normal aortic diameter of about 1.8 cm. At the end of the aorta slits there are two branches, called common Iliac arteries.

[1] www.vmtk.org

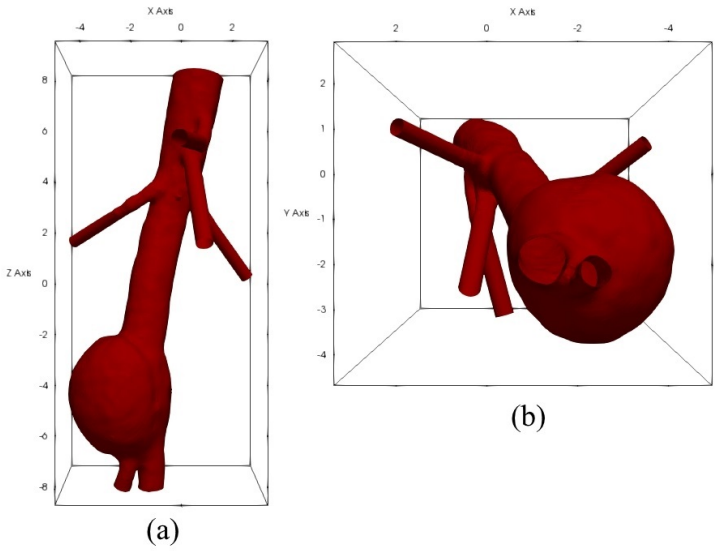

Figure 4.1: Abdominal arterial wall reconstructed by VMTK tools: (a) right-left view, (b) bottom-top view.

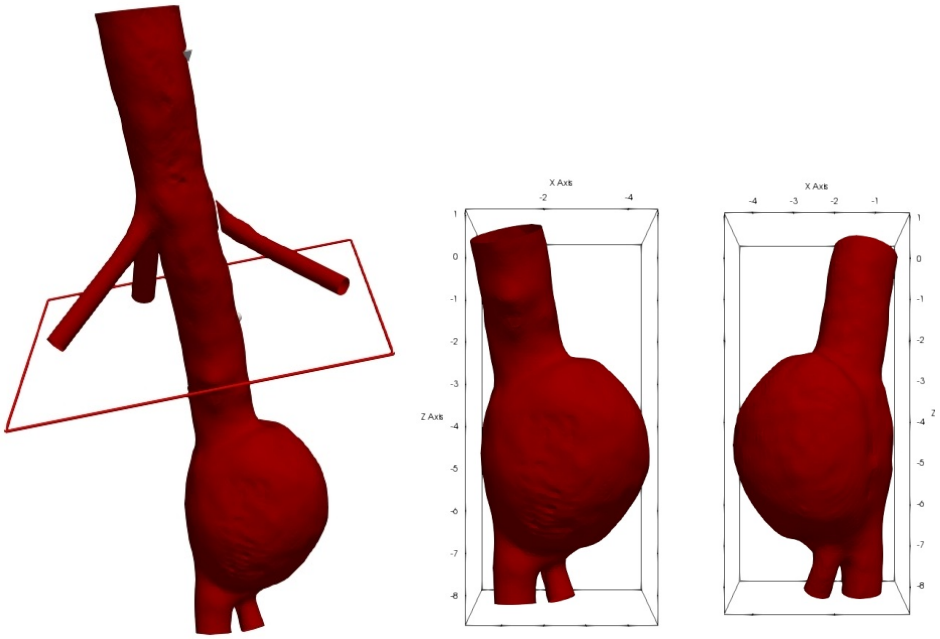

(a) Clipping plane. (b) Geometry after clipping.

Figure 4.2: VMTK clipping

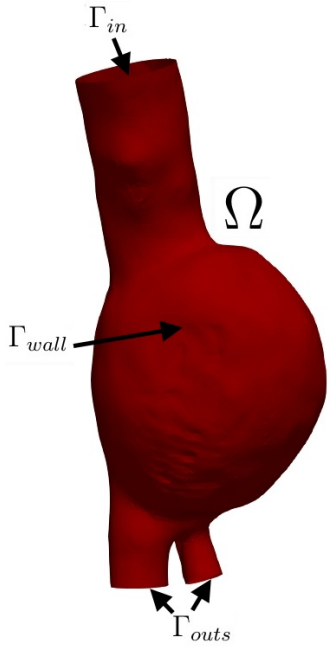

Figure 4.3: Boundaries of the AAA.

To focus our hemodynamic studies inside the aneurysm, we ignore the portion with the branches before the aneurysm. This decision does not influence substantially the fluid behavior in the aneurysm [69]. The clipping plane is placed about 3 cm proximal to the aneurysm and perpendicular to the center line of the vessel as can be seen in Figure 4.2a. The resulting geometry is represented in Figure 4.2b.

Considering the geometry in Figure 4.3, the boundaries of the Ω domain are:

- Γ_{in}, the inlet section of the aorta,
- Γ_{wall}, the arterial wall,
- Γ_{outs}, the two common Iliac outlet sections.

For each boundary, the conditions imposed are:

- On Γ_{in} Dirichlet boundary condition with parabolic velocity profile on inlet section (as explained in Section 4.5)

$$\mathbf{u}(\mathbf{x}, t) = \mathbf{u}_{in}(\mathbf{x}, Q_{in}(t)) \qquad \forall \mathbf{x} \in \Gamma_{in},\ t \in (0, N_c T_{nb}],$$

  where $N_c = 6$ is the number of cardiac cycles, and $T_{hb} = 0.7s$ is the heartbeat period. Concerning $Q_{in}(t)$, a supraceliac waveform is taken

from [74] and its flow rate magnitude is reduced by 50% to match the infrarenal waveforms reported in [75]. The resulting inlet waveform (Figure 3.4) is the used physiological waveform $Q_{in}(t)$.

- On Γ_{wall} homogeneous Dirichlet boundary condition (*rigid wall* hp.)

$$\mathbf{u}(\mathbf{x}, t) = 0 \qquad \forall \mathbf{x} \in \Gamma_{wall},\ t \in (0, N_c T_{hb}].$$

- On Γ_{outs} non-linear Robin boundary condition (due to the Backflow stabilization, detailed in Section 4.6)

$$(-p\mathbf{I} + 2\nu\mathbf{S}(\mathbf{u}) - \boldsymbol{\tau}_d^{sgs})\,\hat{\mathbf{n}} = \beta \int_{\Gamma_{outs}} \frac{1}{2}|\mathbf{u}\cdot\widehat{\mathbf{n}}|_{-}\mathbf{u} d\Gamma \qquad \text{on}\Gamma_{outs}\times(0, N_c T_{hb}],$$

with $\beta = 1$.

4.2 Computational meshes

The surface model (Figure 4.3) was turned into volumetric meshes of linear tetrahedra.

In particular the fluid domain Ω (Figure 4.3) has been discretized with an unstructured tetrahedral meshes. The open source VMTK library [76] has been used to obtain a good quality mesh. A boundary layer composed by three or four layers has been introduced in order to accurately describe the viscous effects near the wall.

In this thesis we generated the following meshes:

I *mesh-DNS* with 1M of tetrahedra (Figures 4.4a, 4.4c);

II *mesh-LES* with 125K of tetrahedra (Figures 4.5a, 4.5c);

Table 4.1: Meshes parameters

	I: *mesh-DNS*	**II**: *mesh-LES*
N_T	1M	125k
h	0.115 cm	0.25 cm
s_{BL}	0.13 cm	0.13 cm
N_{BL}	4	3
δs	0.8	0.7
$N_{d.o.f.}(V)$	4.06 M	511 K
$N_{d.o.f.}(P)$	1.35 M	170 K

The parameters of the meshes **I** and **II** are shown in the table 4.1, where:

- N_T denotes the number of tetrahedra and h the corresponding characteristic space discretization parameter;
- s_{BL} is the boundary layer thickness composed of N_{BL} layers in which a thickness ratio, δs, has been selected between two successive layers;
- $N_{d.o.f.}(V)$ and $N_{d.o.f.}(P)$ are the total number of d.o.f. in the domain Ω, using the FE spaces $\mathbb{P}_2 - \mathbb{P}_2$, for the velocity and pressure field, respectively.

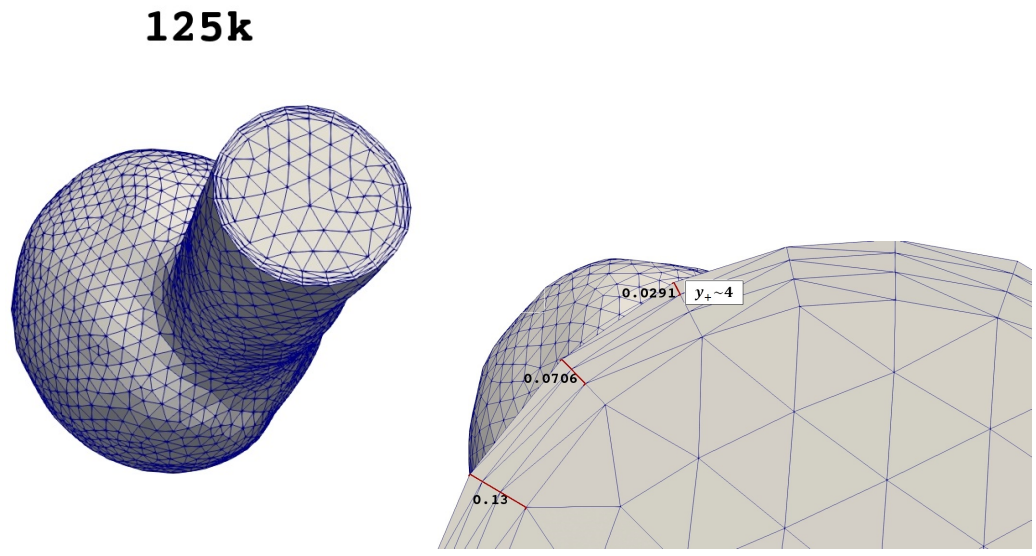

(a) Bottom view. (b) Boundary layers thickness.

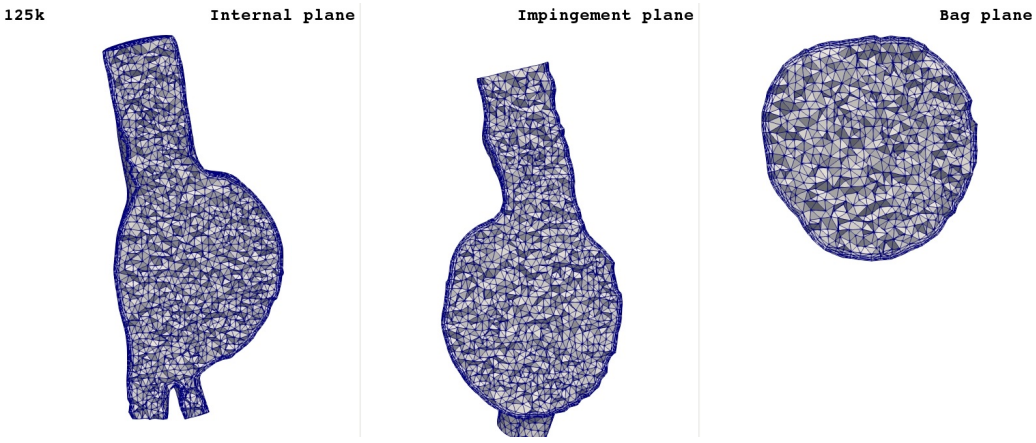

(c) Mesh inside different cut planes.

Figure 4.4: *mesh-LES* of 125k tetrahedra

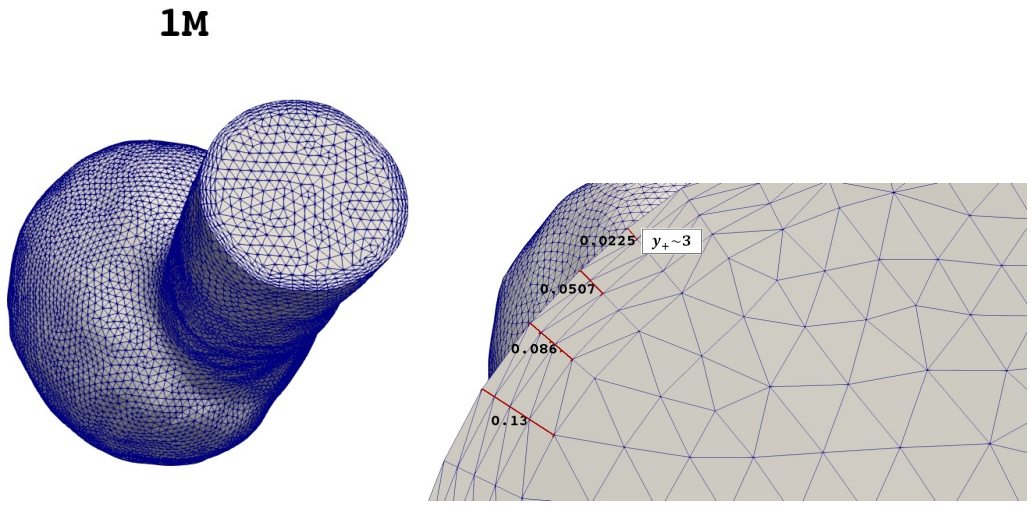

(a) Bottom view.

(b) Boundary layers thickness.

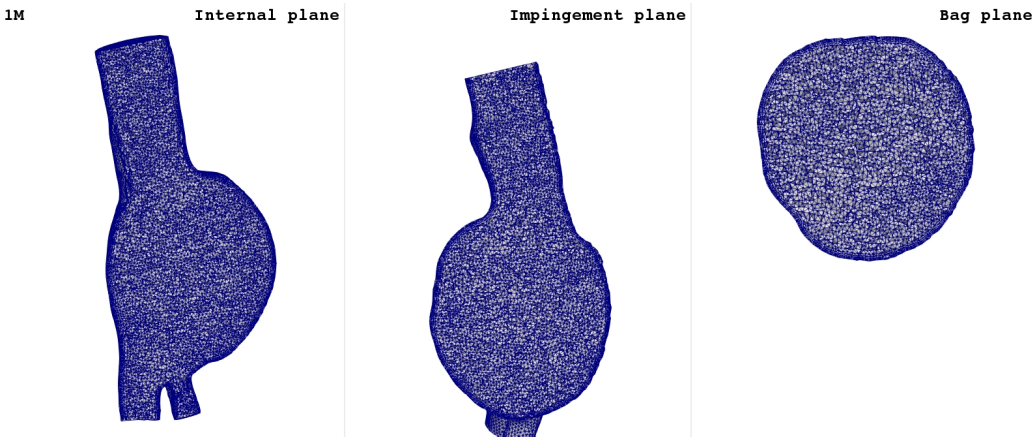

(c) Mesh inside different cut planes.

Figure 4.5: *mesh-DNS* of 1M tetrahedra

In particular, s_{BL}, N_{BL}, and δs allow us to obtain a dimensionless wall distance $y_+ < 5$, at least for the first cell (Figures 4.4b, 4.5b). This means that we have at least one point in the viscous sublayer of the turbulent boundary layer (more details are to be found in [78]). The definition of the dimensionless wall distance is

$$y_+ = \frac{U_* y}{\nu},$$

where y is the physical distance to the wall, and $U_* = \sqrt{\frac{t_w}{\rho}}$, with t_w the wall shear stress (WSS), is the friction velocity.

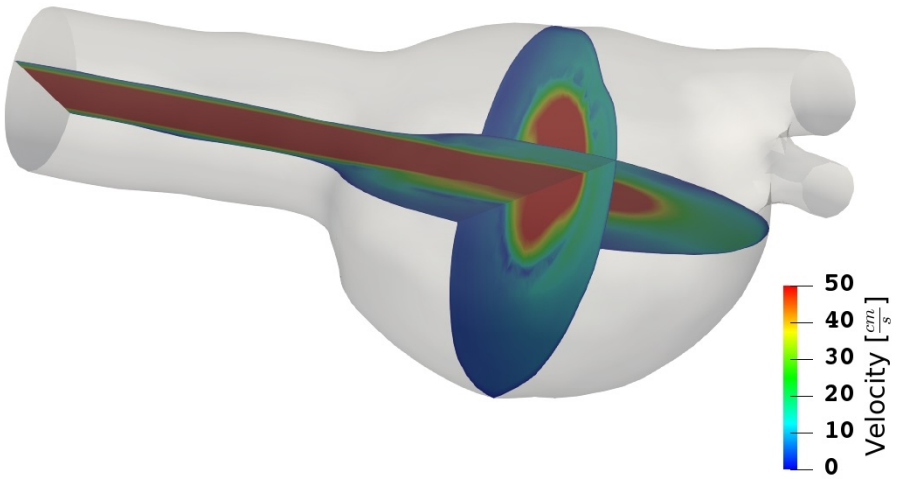

Figure 4.6: Shear layer detachment within the AAA visualized in the impingement plane and in the bag plane.

4.3 Building a DNS

In the hemodynamic framework, complex geometries and pulsatile flow, due to the heartbeat, could generate turbulent transitional effects. In this context, we cannot use the classical Kolmogorov theory (for fully developed homogeneous isotropic and stationary turbulence) to estimate the smallest scale (Kolmogorov scale η) needed to perform a DNS simulation. For this reason, we decided to use an alternative approach, enploied in [17], to generate our DNS mesh.

For the case of stenotic carotid, Lancellotti et al. [17] computed a solution without any turbulence model they called a gold standard. They estimated two shear layers[2] (at the systole) that can trigger the transition to turbulence during the deceleration phase.

Observing our numerical simulations, a long shear layer at the systole, entering in the bulge of AAA, is created (see Figure 4.6). This shear layer, impacting on the bulge wall of the aneurysm, create vortical structures that can trigger the transition to turbulence during the deceleration phase.

Following the same approach of [17], we estimated the mesh size h_{DNS} able to correctly resolve this shear layer which is the primary phenomenon characterizing the blood flow in the AAA. The same holds for the choice of the time discretization parameter δt_{DNS}.

In what follows, we refer to this simulation as the DNS no-model solution.

[2]The shear layer is defined as the region between two parallel streams.

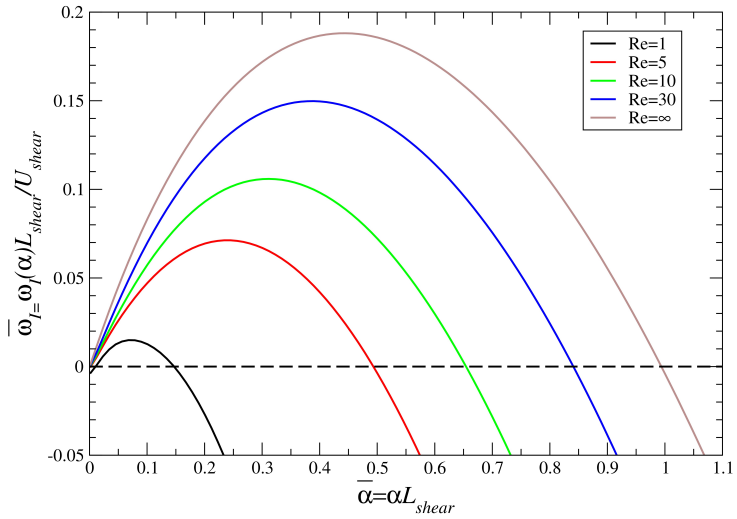

Figure 4.7: Instability curves of a shear layer for different Re. Each curve divides the frequency plane in a stable (top) and an unstable (bottom) regions. The stability regions are depicted as as function of the space frequency αL_{shear} and the time exponential growth factor $\omega_I(\alpha)L_{shear}/U_{shear}$ of the oscillation.

4.3.1 Estimation of the DNS discretization parameters

To be able to define the characteristic mesh size, h_{DNS}, and the time step, δt_{DNS}, of our reference DNS solution, we considered the simplified problem of a viscous, incompressible, and two-dimensional laminar shear layer [77], characterized by the following velocity field

$$\mathbf{u}(x,y) = \left[U_{shear}\tanh\left(\frac{y}{L_{shear}}\right),\ 0\right]^T,$$

where U_{shear} and L_{shear} are the characteristic velocity and width of the shear layer, respectively (to be suitable chosen). The Reynolds number of this shear layer is

$$Re_{shear} = \frac{U_{shear}L_{shear}}{\nu}.$$

We apply, to this two-dimensional laminar shear layer, a perturbation of the form

$$\mathbf{u}'(x,y) = [i\alpha\frac{dv}{dy},\ v(y)e^{i(\alpha x-\omega t)}]^T,$$

where, for a given $\alpha \in \mathbb{R}$, the eigenfunction v and the corresponding eigenvalue $\omega = \omega_R + i\omega_I \in \mathbb{C}$ are determined by forcing the perturbation, $\mathbf{u}'$, to satisfy the linearized NS equations [78].

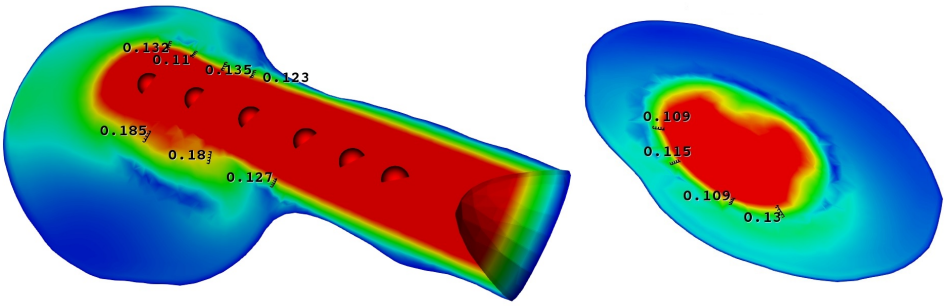

(a) Impingement plane. (b) Bag plane.

Figure 4.8: Measures (125K no-model simulation) of the shear layer thickness, L_{shear} (taken from regions of highest velocities, in red, to regions of lowest velocities, in blue), and of the velocity, U_{shear} (taken in the shear layer center), for two different plane.

Solving numerically the linearized NS equations for $\mathbf{u}'$ [78], it is possible to determine, for each Reynolds number, the stability regions of this two-dimensional shear layer [77]. In particular, it is possible to obtain the curves reported in Figure 4.7, where the instability curves are plotted as a function of the normalized space frequency, $\overline{\alpha} = \alpha L_{shear}$, and the normalized time frequency, $\overline{\omega}_I = \omega_I L_{shear}/U_{shear}$.

A shear layer will be unstable if a perturbation introduced in the system leads to oscillations which grow up in time indefinitely. Otherwise it will be said stable. In our case, the shear layer in a AAA is stable, since the oscillations do not blow up in time. Hence, we have to identify for the Reynolds number, Re_{shear}, the region in the space of the frequencies which lead to either stable or unstable shear layers, and then select the discretization parameters h_{DNS} and δt_{DNS} which guarantee that we fall in the stability region.

In [78] it has been shown that the most unstable eigenvalues have null real part ($\omega_R \simeq 0$) so that the associated modes are characterized by an exponential growth in time. Given the Reynolds number Re_{shear}, by plotting the values of $\overline{\omega}_I = \overline{\omega}_I(\overline{\alpha})$, as a function of $\overline{\alpha}$, we obtained a curve from which we derived the maximum value of $\overline{\omega}_I$, $\overline{\omega}_{I,max}$, and the maximum value of $\overline{\alpha}$, $\overline{\alpha}_{max}$, such that $\overline{\omega}_I(\overline{\alpha}) > 0$ for each $\overline{\alpha} < \overline{\alpha}_{max}$ (see Figure 4.9). Thus, we can obtain the values for h_{DNS} and δt_{DNS} as

$$h_{DNS} \leq \frac{AL_{shear}}{\overline{\alpha}_{max}}, \qquad \delta t_{DNS} \leq \frac{BL_{shear}}{\overline{\omega}_{I,max} U_{shear}}, \tag{4.1}$$

where A, $B < 1$ are two control parameters.

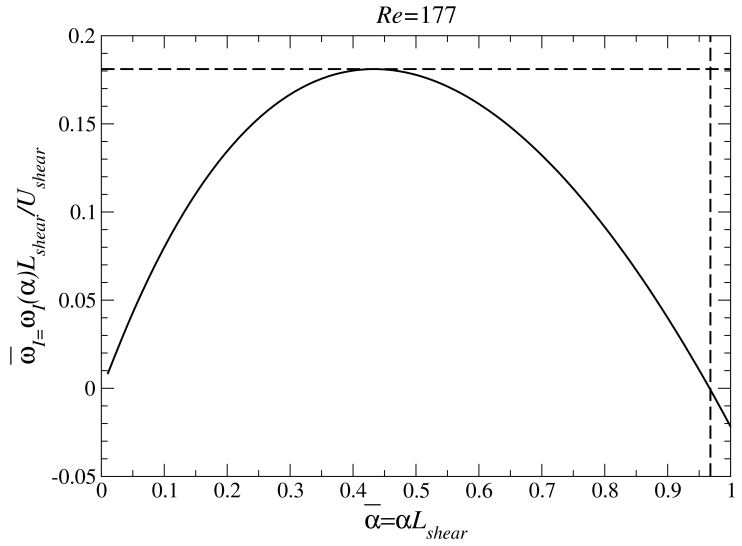

Figure 4.9: Growth rate for the shear layer instabilities for $Re_{shear} = 177$ as a function of the normalized spatial frequency αL_{shear}.

To determine Re_{shear}, we considered a no-model simulation (i.e. with no LES model) using the *mesh-LES* with 125K of tetrahedra (Figure 4.6). In particular, we measured (at systole) in different points the shear layer thickness L_{shear} and the velocity in the shear layer center, U_{shear} (see Figures 4.8)

$$U_{shear} \simeq 50\, cm/s \quad L_{shear} \simeq 0.124cm \Longrightarrow Re_{shear} \simeq 177. \tag{4.2}$$

Using this value of Re_{shear} with the procedure explained above, we obtained the Figure 4.9 from which we had

$$\overline{\alpha}_{max} = \alpha_{max} L_{shear} = 0.97, \qquad \overline{\omega}_{I,max} = \omega_I(\alpha_{max}) L_{shear}/U_{shear} = 0.18. \tag{4.3}$$

Inserting the 4.3 and 4.2 in 4.1, and choosing $A = 1/2$, $B = 1/4$, we got the following values of the discretization parameters which allow to well resolve the shear layer

$$h_{DNS} \leq 0.124\, cm \qquad\qquad \delta t_{DNS} \leq 6\, ms,$$

where we also doubled these two parameters because we considered a second order discretization in space and time ($\mathbb{P}_2-\mathbb{P}_2$, and BDF2), as we will specify in Section 5.1. Hence, we choose the following characteristic mesh size, h_{DNS}, and time step, δt_{DNS},

$$h_{DNS} = 0.115\, cm \qquad\qquad \delta t_{DNS} = 2\, ms.$$

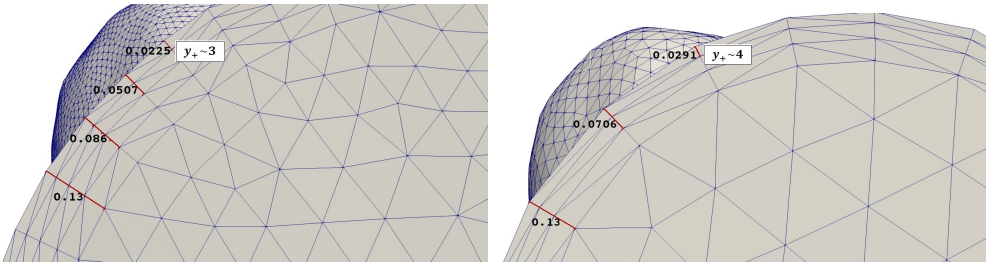

(a) *mesh-DNS* 1M (b) *mesh-LES* 125K

Figure 4.10: The dimensionless wall distance, $y_+^{(1)}$ for the first mesh point from the wall, in *mesh-DNS* (a) and *mesh-LES* (b).

In particular, $h_{DNS} = 0.115cm$ is the value used to build the *mesh-DNS* with 1M of tetrahedra (Figure 4.5), and $\delta t_{DNS} = 2ms$ is the time step used for all the simulations. Moreover, for the time step we chose an even smaller value to well fulfill the stability condition (3.10).

4.3.2 Estimation of Boundary Layer thickness

In order to estimate the boundary layer (BL) thickness, we evaluated the WSS in a no-model simulation using the *mesh-LES* 125K.

To define the WSS, we first introduce the traction tensor, $\mathbf{T}$, which is defined as the Cauchy stress tensor, $\boldsymbol{\sigma} = -p\mathbf{I} + 2\mu\mathbf{S}$, minus the hydrostatic component (due to the pressure), and the traction vector $\boldsymbol{\tau} = \mathbf{T}\widehat{\mathbf{n}}$ acting on a surface with an outward normal $\widehat{\mathbf{n}}$

$$\mathbf{T} = 2\mu\mathbf{S}(\mathbf{u}) \Longrightarrow \boldsymbol{\tau} = 2\mu\mathbf{S}(\mathbf{u})\widehat{\mathbf{n}},$$

where we recall that $\mathbf{S}(\mathbf{u}) = \frac{1}{2}\left(\nabla\mathbf{u} + (\nabla\mathbf{u})^T\right)$.

The WSS is defined as the L^2-norm of the tangential component of the traction vector

$$WSS = \|\boldsymbol{\tau}\widehat{\mathbf{t}}\| = \|\boldsymbol{\tau} - \boldsymbol{\tau}\widehat{\mathbf{n}}\|,$$

where $\widehat{\mathbf{t}}$ is the tangential unit vector of the surface in which $\mathbf{t}$ acts.

We measured the maximal values of the WSS (during the six cardiac cycles) for different points on:

I Inlet section: from the inlet to the beginning of the bulge aneurysm (see Figure 4.11a);

II Bulge section: in the bulge wall of the aneurysm (see Figure 4.11b);

III Outlets section: from the end of the bulge to the outlets (see Figure 4.11c).

We obtained :

I: $WSS_{max}^{(I)} \simeq 3.5\ Pa$; **II**: $WSS_{max}^{(II)} \simeq 8\ Pa$; **III**: $WSS_{max}^{(III)} \simeq 9 - 10\ Pa$. (see plots in Figures 4.11)

Hence, we measured the dimensionless wall distance, $y_+^{(1)}$ for the first mesh point from the wall (see Figure 4.10)

$$y_+^{(1)} = \frac{yU_*}{\nu}, \quad \text{with} \quad U_* = \sqrt{\frac{WSS_{max}}{\rho}},$$

where we had halved the value of $y_+^{(1)}$ because we considered a second order in space and time discretization ($\mathbb{P}_2 - \mathbb{P}_2$, and BDF2).

These values of $y_+^{(1)}$, for different sections **I**, **II**, **III**, are well inside the viscous sublayer, which for developed turbulence is generally assessed to extend to $y_+ \sim 5$ [78] (see Figures 4.10, 4.11 and tables 4.2, 4.3).

The tables (4.2 - 4.3) below shown the values y_+ for the layers of the BL in the *mesh-DNS* and *mesh-LES* (see Figure 4.10).

Table 4.2: dimensionless wall distances for BL of *mesh-DNS*

	Inlet	Bulge	Out Left	Out Right
$y_+^{(1)}$	1.96	2.96	3.31	3.14
$y_+^{(2)}$	4.41	6.67	7.46	7.08
$y_+^{(3)}$	7.49	11.32	12.66	12.07
$y_+^{(4)}$	11.32	17.11	19.13	18.15

Table 4.3: dimensionless wall distances for BL of *mesh-LES*

	Inlet	Bulge	Out Left	Out Right
$y_+^{(1)}$	2.53	3.83	4.28	4.06
$y_+^{(2)}$	6.15	9.29	10.39	9.86
$y_+^{(3)}$	11.32	17.11	19.13	18.15

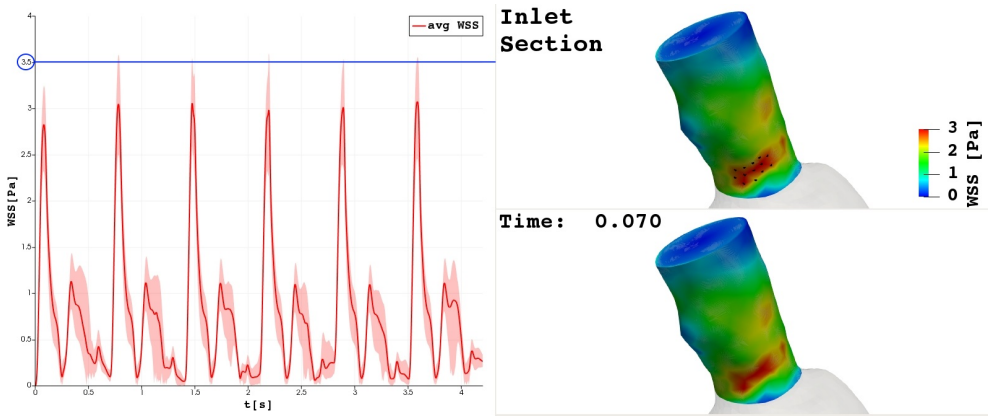

(a) Inlet section

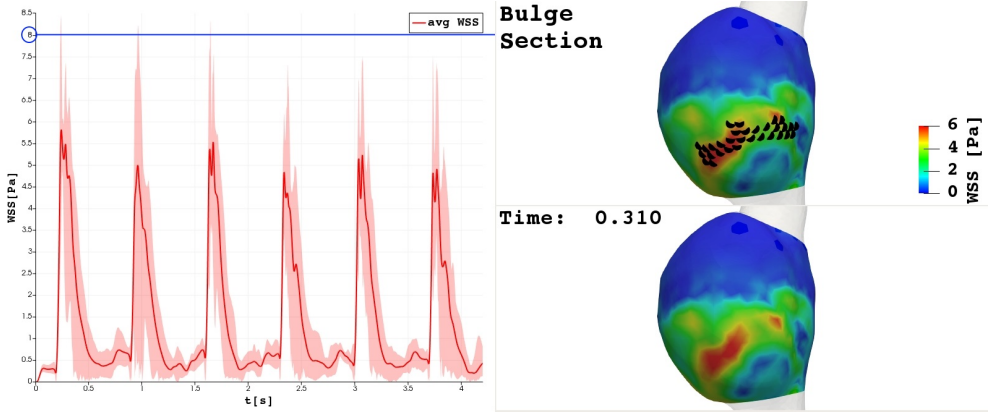

(b) Bulge section

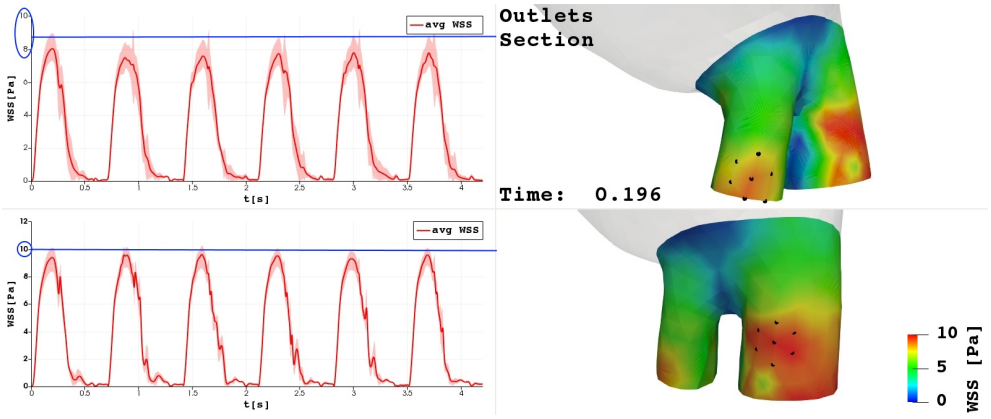

(c) Outlets section

Figure 4.11: WSS measured, during the six cardiac cycles, for specific points on different section: (a) Inlet section, (b) Bulge section, (c) Outlets section. The plots on the left are the WSS(t) for the selected points (showed in black).

Chapter 5

Numerical results

Numerical simulations were performed with the C++ parallel Finite Element library LIFEV [1] which is developed at MOX (Politecnico di Milano), INRIA (Paris), CMSCS (EPFL in Lausanne) and E(CM)^2 (Emory University of Atlanta).

LIFEV is an object oriented software (with parallel and serial version) aimed to solve complex real engineering problems. To exploit parallel computing (partitioning the mesh), it relies on ParMETIS[2], whereas the solution of the linear system is based on Trilinos[3]. In particular, the linear system arising at each time step has been solved with GMRES, preconditioned with an Additive Schwarz preconditioner available in the package Ifpack of Trilinos.

Simulations on the *mesh-LES* were run on 1 node Xerox E4610-v2 of 20 cores cluster with 64GB memory per node. Simulation on the *mesh-DNS* was run on a 2 nodes Xerox E4610-v2 of 32 cores cluster with 252GB memory per node.

The code used in this thesis, based on the turbulence models introduced in Chapter 2, was validated in [79] through a decaying isotropic turbulent test case in which different LES models were successfully compared with experimental results. The author (for details see [79]) showed that the σ-models (static and dynamics) obtain an excellent agreement (measuring the kinetic energy) with experimental results (see Figure 5.1). Moreover, the code was also used in the cardiovascular framework, in a stenotic carotid context [17] and in a primary study of transition to turbulence in AAA [20].

[1] https://cmcsforge.epfl.ch/doxygen/lifev/

[2] http://glaros.dtc.umn.edu/gkhome/views/metis

[3] http://trilinos.sandia.gov

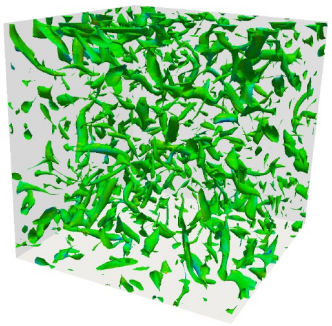

(a) High vorticity coherent structures.

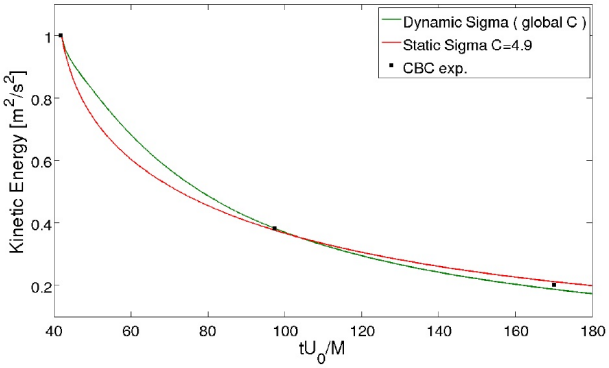

(b) Resolved kinetic energy.

Figure 5.1: (a) High vorticity coherent structures in the freely decaying isotropic homogeneous turbulence simulation; (b) Time evolution of resolved kinetic energy: comparison between the static σ model, and its dynamic version, with the experimental data. Pictures taken from [79].

Using the working conditions described in the Section 5.1 we ran the following simulations:

- DNS no-model on *mesh-DNS*;
- LES static σ-model ($C_\sigma = 1.5$) on *mesh-LES*;
- LES dynamic σ-model on *mesh-LES*.

The chosen value $C_\sigma = 1.5$ for the static σ-model was used by Nicoud et al. [38] in the case of decaying isotropic turbulence and plane channel flow, and also successfully used in another heamodynamic case treating the study of turbulence flow in a stenotic carotids in presence of atheromasic plaque [17], and in a primary investigation of turbulence flow in an abdominal aortic aneurysm [20].

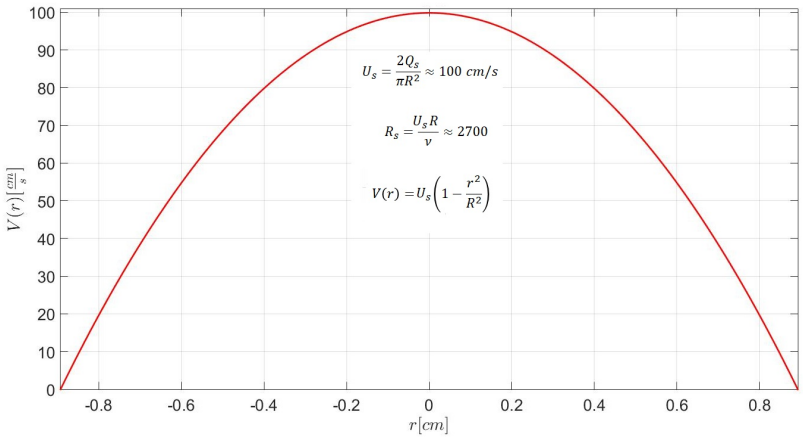

Figure 5.2: Systolic velocity profile at the inlet.

5.1 Simulations parameters

Common parameters among the simulations are:

- time step of $\delta t = 2\,ms$ with a BDF2;
- $N_c = 6$ cardiac cycles; $T_{hb} = 0.7s$ heartbeat period: $T = N_c T_{hb} = 4.2s$;
- $\mathbb{P}_2 - \mathbb{P}_2$ FE spaces with SUPG-PSPG stabilization;
- SUPG-PSPG coefficient $\gamma = 1$;
- static σ-model constant $C_\sigma = 1.5$;
- blood density $\rho = 1.06\,g/cm^3$;
- blood dynamic viscosity $\mu = 0.035\,g/(cm\,s)$;
- blood kinematic viscosity $\nu = \frac{\mu}{\rho} = 0.033\,cm/s^2$;
- $2R = 1.8cm$, the diameter at the inlet.
- $Q_s = 125cm^3/s$, the systolic flow rate at the inlet (see Figure 5.3);
- $U_s = \frac{2Q_s}{\pi R^2} \simeq 100cm/s$ is the max systolic velocity at the inlet (see Figure 5.2).

The peak systolic Reynolds number, Re_s, at the inlet is

$$Re_s = \frac{U_s R}{\nu} = \frac{2Q_s}{\pi R \nu} \simeq 2700.$$

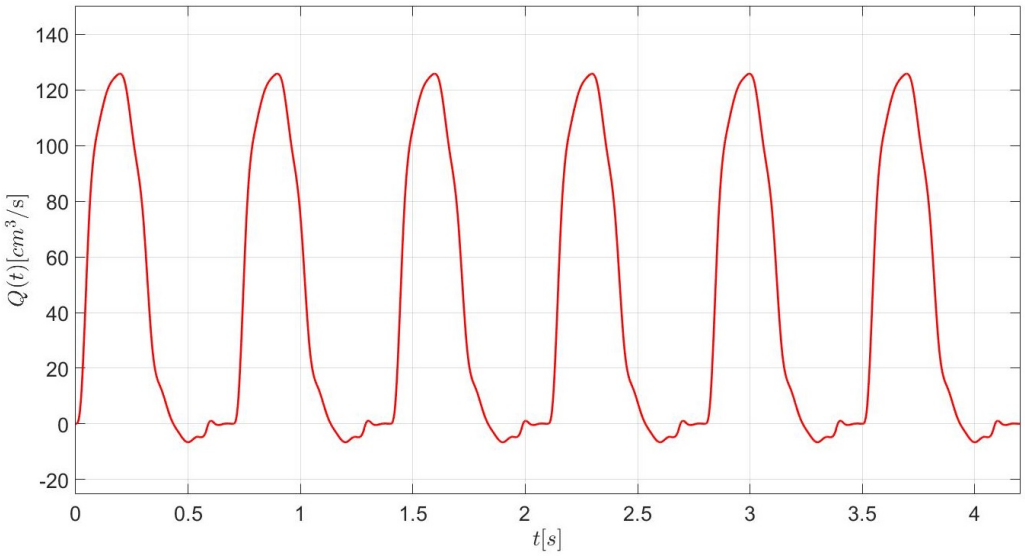

Figure 5.3: Six cardiac cycles, with period $T_{hb} = 0.7s$ for each cycle.

We considered six cardiac cycles for a total simulation time of $4.2s$. For six cardiac cycles (see Figure 5.3), we have (see Table 5.1):

- at $t_s^{(n)} = n\,0.196s$, $n = 1, ..., 6$, Systolic peaks,
- at $t_m^{(n)} = n\,0.31s$, $n = 1, ..., 6$, Mid deceleration points,
- at $t_d^{(n)} = n\,0.5s$, $n = 1, ..., 6$, Diastole peaks.

Table 5.1: Systolic, Mid deceleration, and Diastolic points, in $N_c = 6$.

	t_s	t_m	t_d
$1^{st}T_{hb}$	0.196s	0.310s	0.500s
$2^{nd}T_{hb}$	0.896s	1.010s	1.200s
$3^{th}T_{hb}$	1.596s	1.710s	1.900s
$4^{th}T_{hb}$	2.296s	2.410s	2.600s
$5^{th}T_{hb}$	2.996s	3.110s	3.300s
$6^{th}T_{hb}$	3.696s	3.810s	4.000s

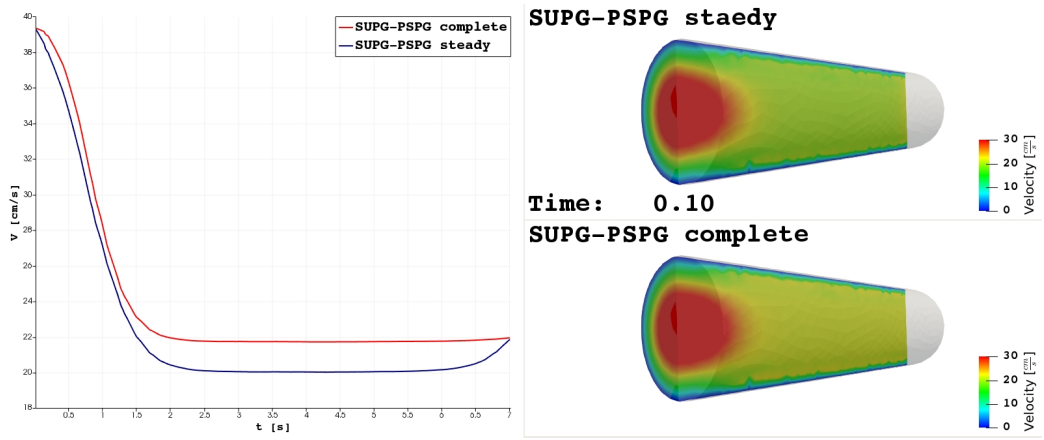

Figure 5.4: Velocity magnitude in the center line of a cylinder middle plane for the complete SUPG-PSPG (in red) and for the "steady" SUPG-PSPG stabilization (in blue).

5.2 SUPG-PSPG implementation

In LIFEV library the SUPG-PSPG stabilization (described in Section 3.4) was implemented only for the case of steady NS equations[4].

In this thesis, we implemented the fully SUPG-PSPG stabilization for the complete NS (3.1) (in the monolithic framework). In particular, we add to the existing SUPG-PSPG function of LIFEV library the missing terms $s_{11}^{(1)}$, $s_{21}^{(1)}$, f_v, and f_q (refer to 3.13).

We have tested the complete SUPG-PSPG stabilization just implemented, comparing it with the steady version, in the simple case of a flow inside a cylinder.

Figure (5.4) shows the comparison between the new version of the complete SUPG-PSPG stabilization and the steady old version. Observing the plot on the left in Figure (5.4), we see how the complete stabilization is less dissipative with respect to the steady version. This is because the steady version is a consistent stabilization, while the complete version is a strongly consistent one.

The less dissipation of the complete SUPG-PSPG is a very important feature because, when we add in the NS equations the term corresponding to the subgrid viscosity characteristic of the LES σ-model, also the subgrid term produces some dissipation. With a mesh very fine, both the stabilization and the subgrid terms goes to zero. The important difference is that the SUPG-PSPG refers to a numerical artificial diffusion, while the turbulent

[4]The steady Navier Stokes equations do not include the temporal derivative in the 3.1a.

viscosity is a physical diffusion which is involved in the process of modeling the unresolved scales. Hence the use of a strongly consistent stabilization is mandatory to avoid numerical artificial dissipation.

All the results that follows use the new complete version of the SUPG-PSPG stabilization.

5.3 Description of the reference solution

Our first analysis concerns the description of the blood flow dynamics emerging by the DNS-reference/no-model simulation.

We considered three time instants in the first cardiac cycle, namely the systolic peak $t_s = 0.196s$, the mid-deceleration point $t_m = 0.310s$, and the diastolic peak $t_d = 0.500s$.

In Figure 5.5 we report the velocity field magnitude during the first heartbeat at three different sliced planes: the Internal plane, a middle slice including both the inlet and the outlets; the Impingement plane, normal to the Internal plane, starting from the inlet and finishing on the shear layer impact zone on the bulge of AAA; the Bag plane, normal to the Internal and Impingement planes, taken approximately in the middle of the AAA bulge. The view generated by these sliced planes can be useful to see the evolution of the blood fluid dynamics inside the AAA. Figure 5.7 shows all the planes mentioned above viewed separately.

In Figure 5.6 we report the velocity field magnitude on five consecutive 3D warped sliced sections (from the inlet to the outlets).

From the Figures (5.5, 5.6, 5.7) we observe, as expected, the formation of a shear layer, which is compact and intact at the Systole (see Figures 5.5a, 5.6a, 5.7a). The jet impinges on the distal part of the aneurysmatic sac, and breaks down leading to chaotic and random swirling structures inside the AAA (see Figures 5.5b, 5.6b). We can see that after flow impingement on the arterial wall, the fluid creates a complex vortical field (see Figures 5.5b, 5.7b). The vortices created persist during the diastolic phase till the end of the cardiac cycle (see Figures 5.5c, 5.6c, 5.7c).

The above considerations are confirmed also by the Figure 5.8 representing the vorticity ($\boldsymbol{\omega} = \nabla \times \mathbf{u}$) field for the same sliced planes (Internal, Impingement, Bag plane). In Figure 5.8a we can see the annular vortex formed during the systolic phase, which grows and advances, and finally breaks into smaller vortices during mid-deceleration and diastolic phases (see Figures 5.8b, 5.8c). Hence, at the mid-deceleration point, the transitional effects are well highlighted also by the vorticity. During the remaining part of the cardiac cycle, these vortices decay slowly.

Lastly, in Figure 5.9 we report the Wall Shear Stress (WSS) over the first heartbeat. The WSS reaches its maximum value during the mid deceleration phase. From the Figure 5.8a, we observe large values in correspondence of the impingement regions.

These Figures (5.5, 5.6, 5.7, 5.8, 5.9) indicate that for the DNS-reference solution the presence of disturbed flow field , in the aneurysmatic sac, appears particularly at the mid-deceleration and early diastolic phases.

We conclude by saying that the pulsatility of the blood flow does not allow the complete development into a turbulent flow regime. This is prevented by the acceleration phase of a new heartbeat that laminarizes the flow (see Figure 5.27a). This is the reason why we prefer to call the instability processes in AAA, a transition to turbulence, instead of a fully developed turbulent flow.

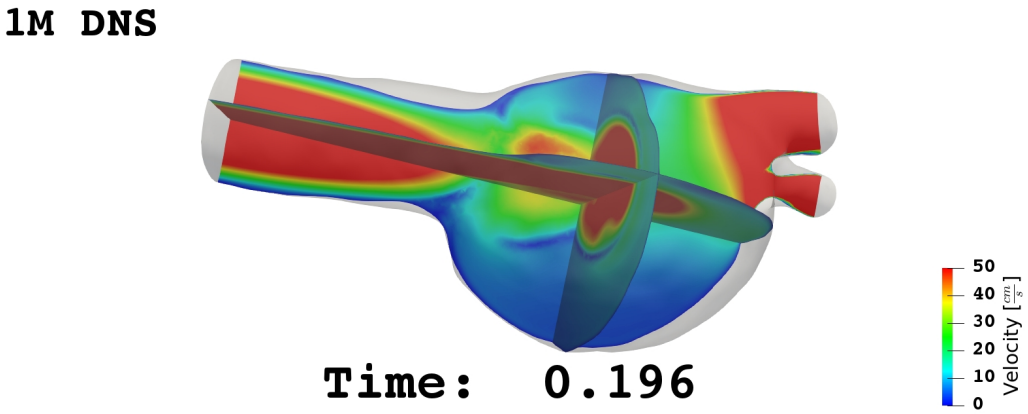

(a) Systolic peak.

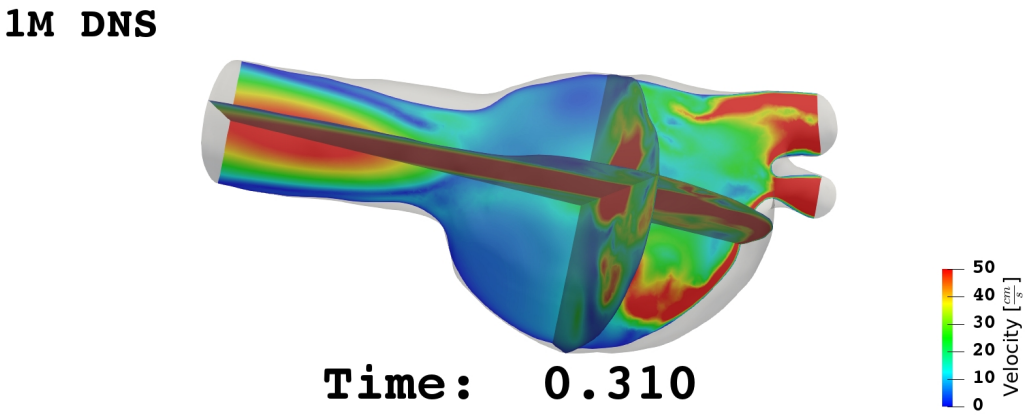

(b) Mid deceleration point.

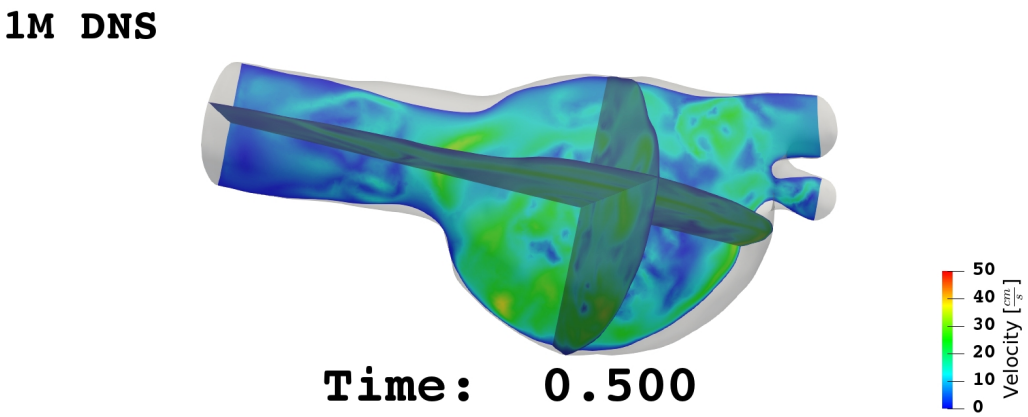

(c) Diastolic peak.

Figure 5.5: DNS Velocity field on three sliced planes (Internal, Impingement, and Bag plane) at Systole (a), Mid deceleration point (b), Diastole (c).

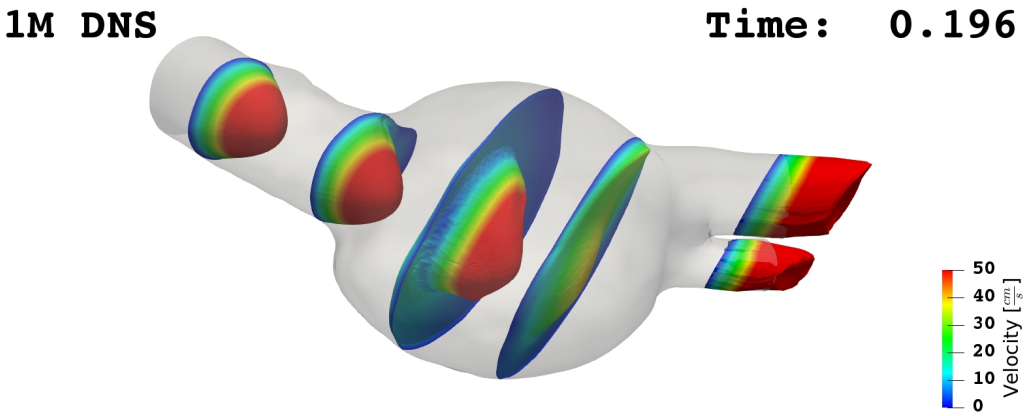

(a) Systolic peak.

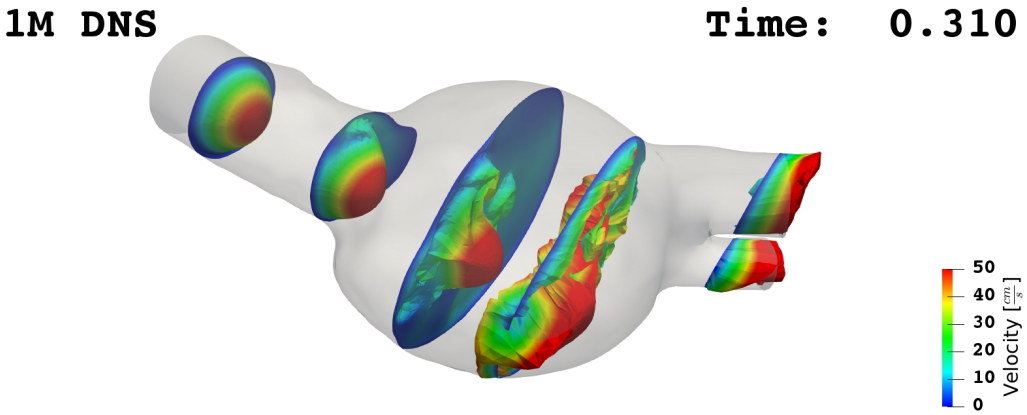

(b) Mid deceleration point.

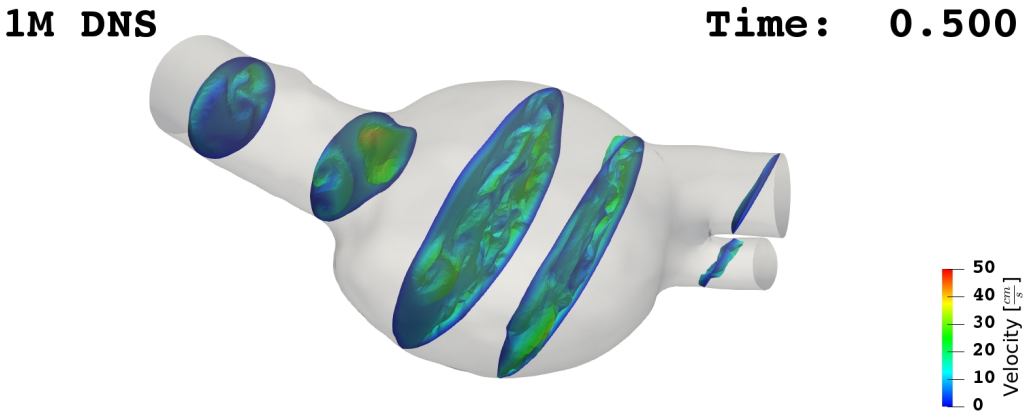

(c) Diastolic peak.

Figure 5.6: DNS Velocity field on different 3D warped sliced sections (from the inlet to outlets) at Systole (a), Mid deceleration point (b), Diastole (c).

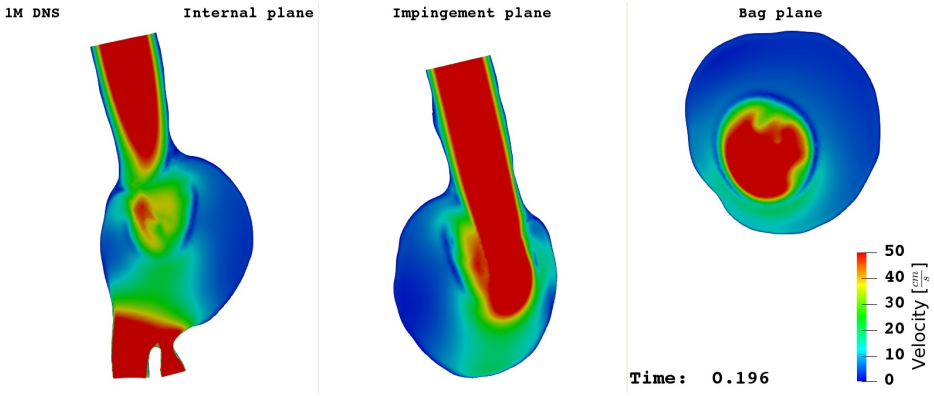

(a) Systolic peak.

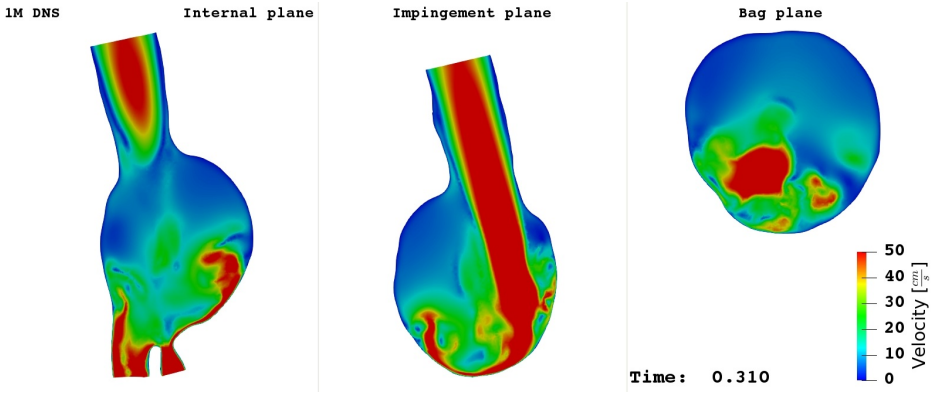

(b) Mid deceleration point.

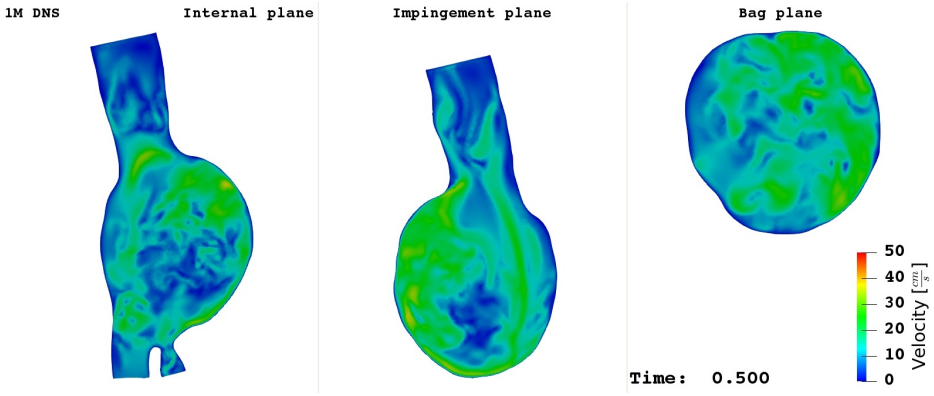

(c) Diastolic peak.

Figure 5.7: DNS Velocity field on Internal, Impingement, and Bag plane at Systole (a), Mid deceleration point (b), Diastole (c).

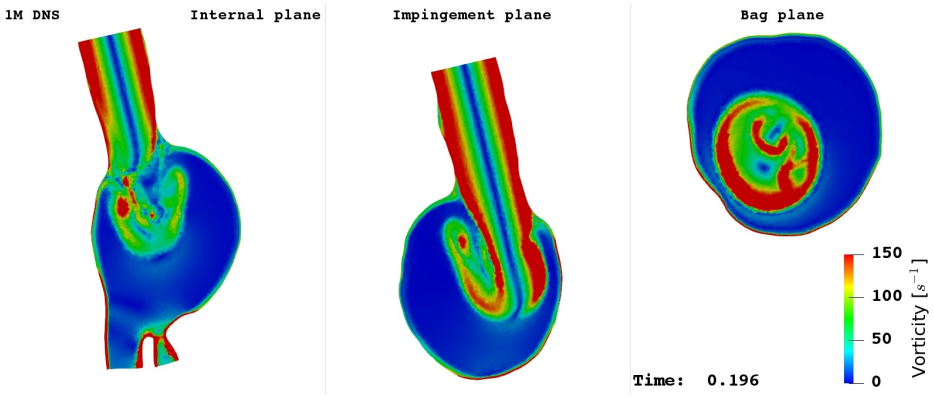

(a) Systolic peak.

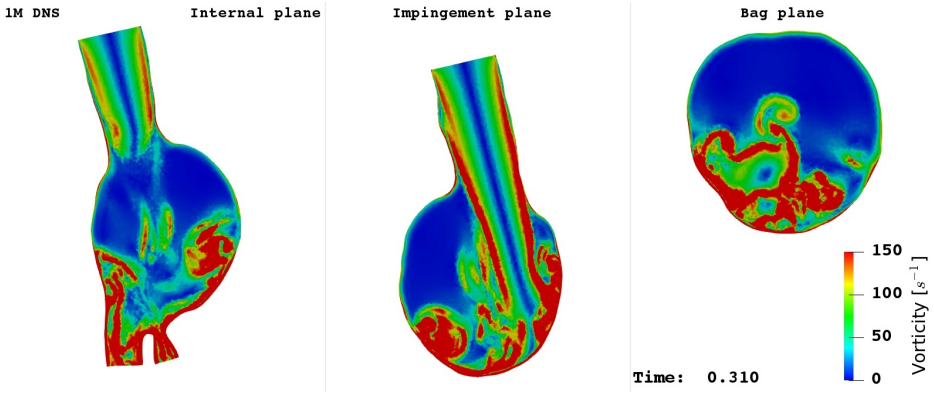

(b) Mid deceleration point.

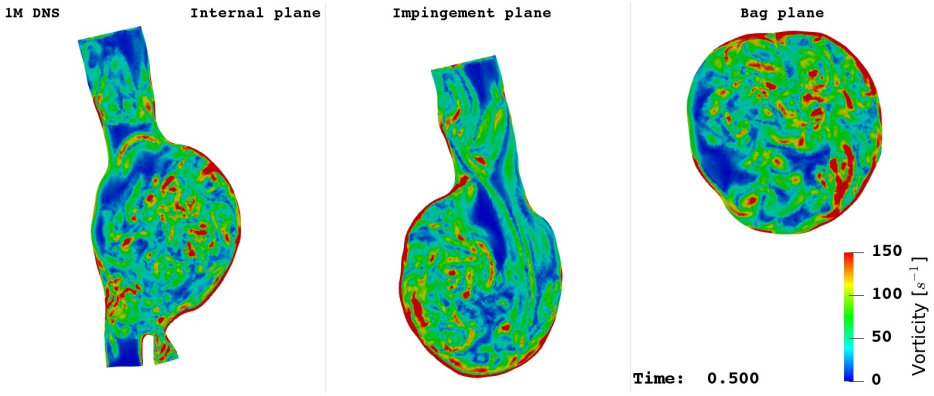

(c) Diastolic peak.

Figure 5.8: DNS Vorticity field on Internal, Impingement, and Bag plane at Systole (a), Mid deceleration point (b), Diastole (c).

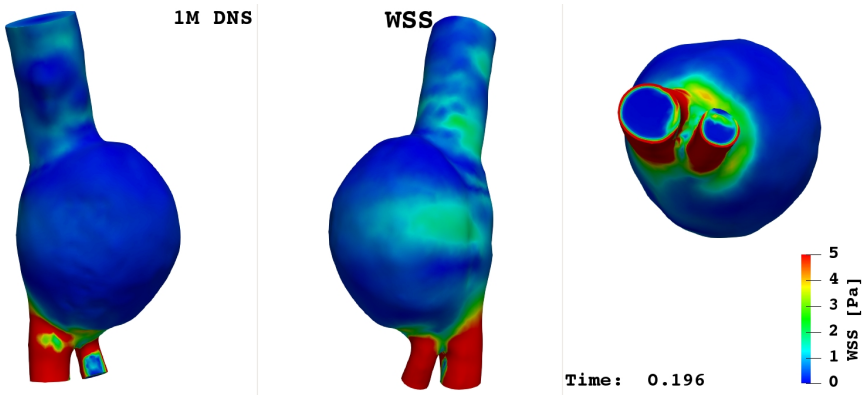

(a) Systolic peak.

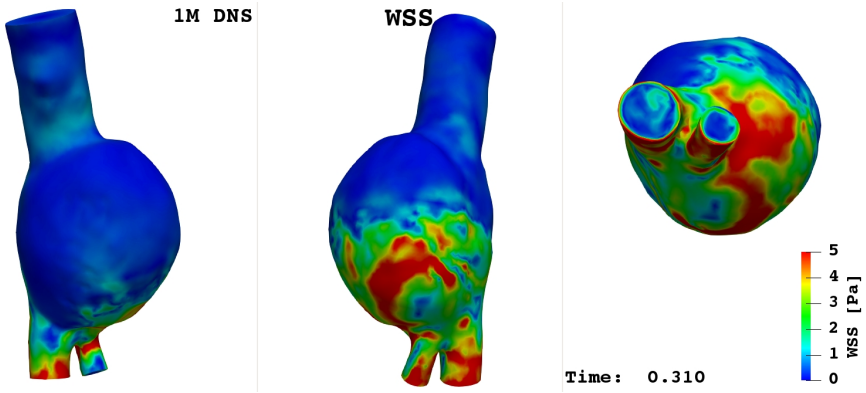

(b) Mid deceleration point.

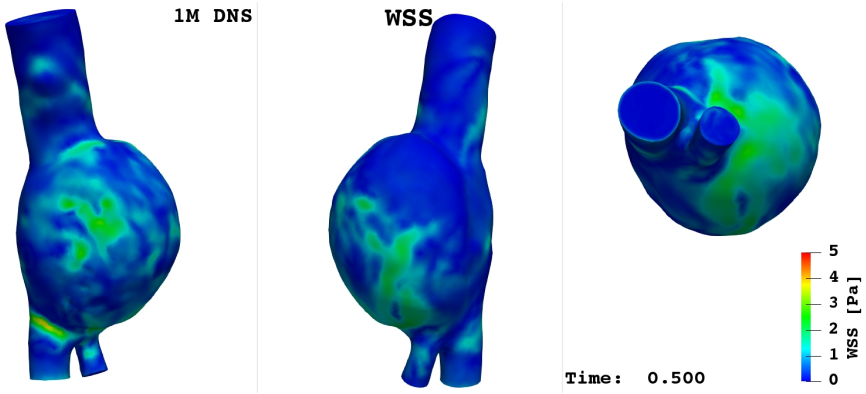

(c) Diastolic peak.

Figure 5.9: DNS Wall Shear Stress (for different views) at Systole (a), Mid deceleration point (b), Diastole (c).

5.4 Comparison between different simulations

The aim of this Section is to provide a comparison among the solutions obtained by the reference simulation (DNS) and the LES models (σ-static and σ-dynamic) described in Chapter 2.

A first comparison was made considering the WSS, the velocity and the vorticity fields. Again, we considered three time instants in the first cardiac cycle: systolic peak $t_s = 0.196s$, mid-deceleration point $t_m = 0.310s$, and diastolic peak $t_d = 0.500s$.

Regarding the velocity (Figures 5.10, 5.11, 5.12) and vorticity (Figures 5.13, 5.14, 5.15) fields we focused our analysis at the same sliced plane considered in the description of reference solution (Internal, Impingement, and Bag plane).

At the systolic peak, velocity and vorticity fields presents very small differences between the simulations (see Figures 5.10, 5.13). Some marginal differences can be noticed during the deceleration phase (see Figures 5.11, 5.14), while greater differences can be seen going to the diastolic phase. At the diastolic peak the differences are amplified and become significant (see Figures 5.12, 5.15). Moreover, the vorticity field patterns with the DNS finer mesh are better captured. In particular, vortices in simulations with LES models seem to be more compact and less dispersed with respect to the DNS-solution (see Figure, 5.15). Moreover, the LES simulations seem to be a little bit more dissipative then the DNS one. This dissipation may be due to the turbulent viscosity that take into account the unresolved scales. Lastly, almost no differences can be noticed between the σ-static and σ-dynamic simulations.

Similar considerations can be done for the WSS (Figures 5.16, 5.17, 5.18). WSS reaches its maximum values at the mid deceleration point (see Figure 5.16). From Figure 5.16, we observe large values in the impingement region. Between the DNS and the LES simulations, almost no difference can be seen during the systolic peak (Figure 5.16), while some differences are present at the mid deceleration point (Figure 5.17). Going to the diastolic phase, differences in WSS patterns become remarkable.

The differences around the diastolic phase could be explained by the presence of transitional fluctuations that arise during deceleration and diastolic phases. Indeed, the primary vortex burst occurs during these phases of the cardiac cycle. The vortex burst leads to a disturbed flow and thus to turbulent transitional flow that produces a fluctuating velocity field.

Notwithstanding these differences, in this first comparison, the DNS and the LES simulations capture almost the same features in the blood fluid dynamics inside the aneurysmatic sac.

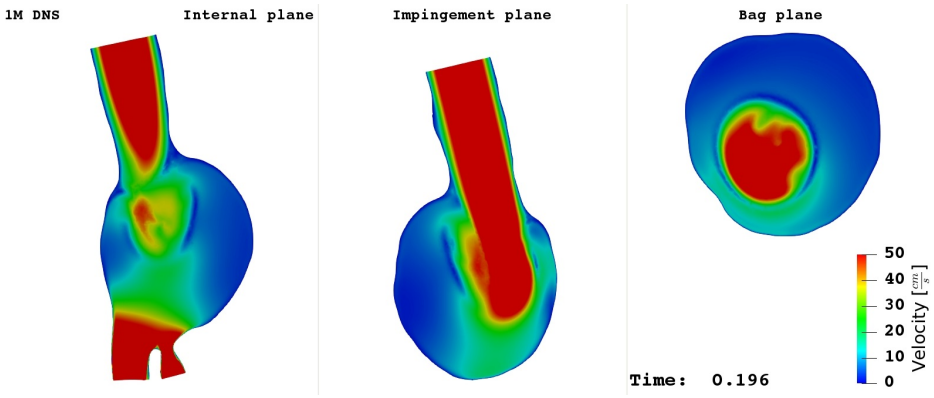

(a) DNS.

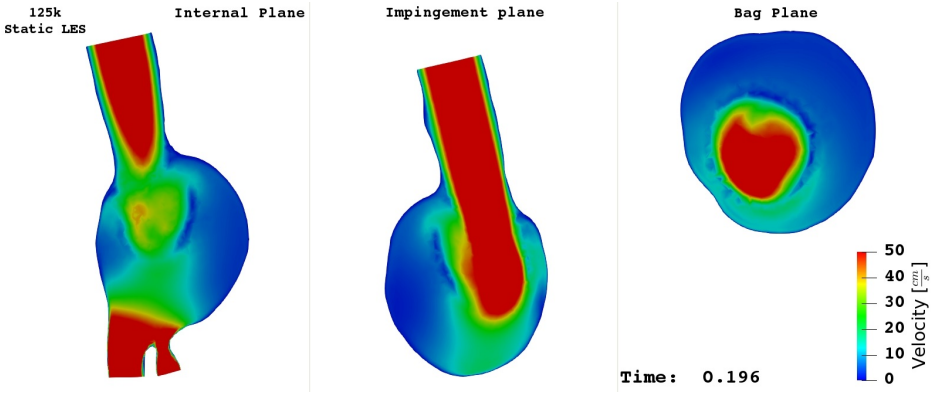

(b) Static-σ.

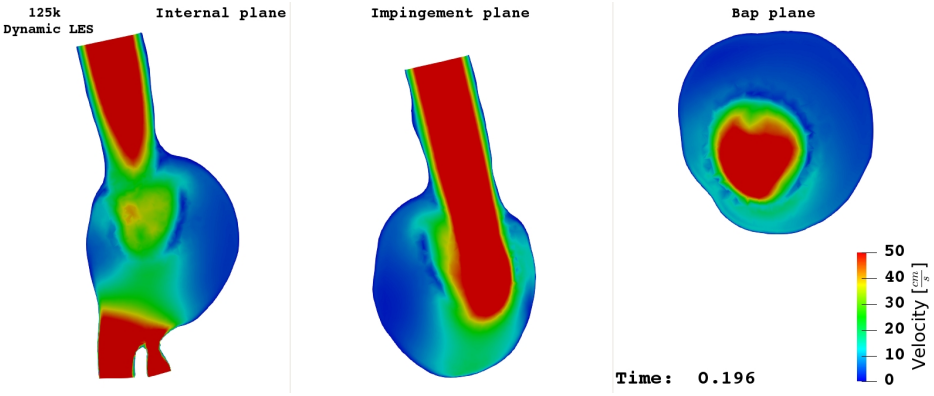

(c) Dynamic-σ.

Figure 5.10: Velocity field at the Systole on Internal, Impingement, and Bag plane in DNS (a), Static-σ (b), and Dynamic-σ (c) simulation.

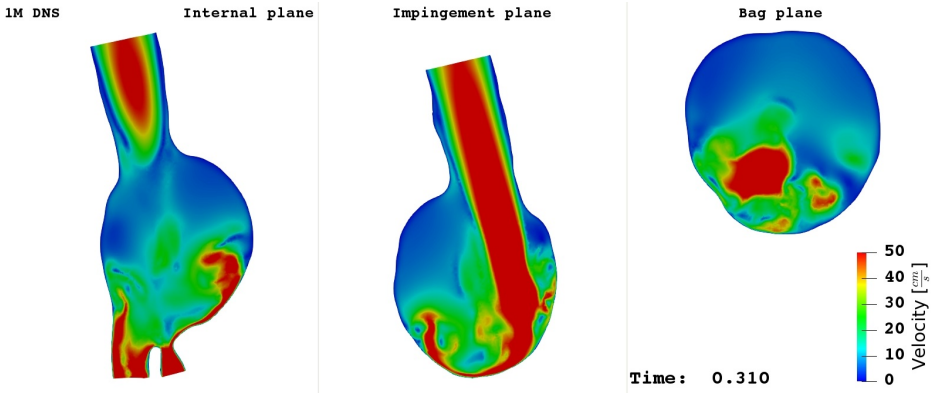

(a) DNS.

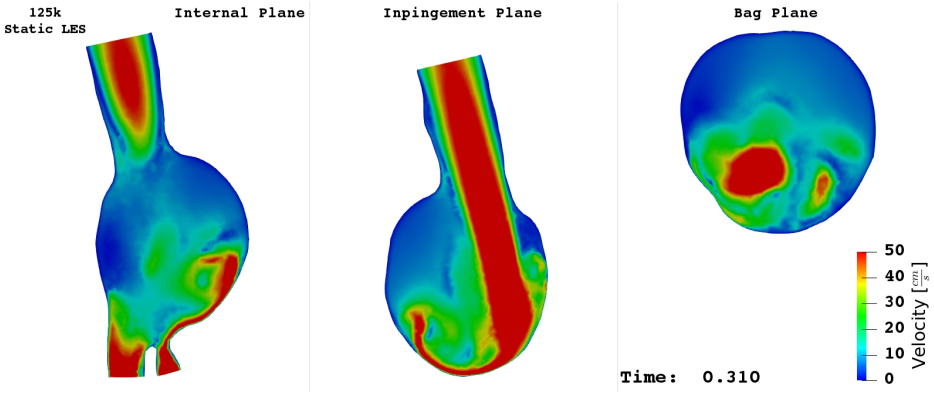

(b) Static-σ.

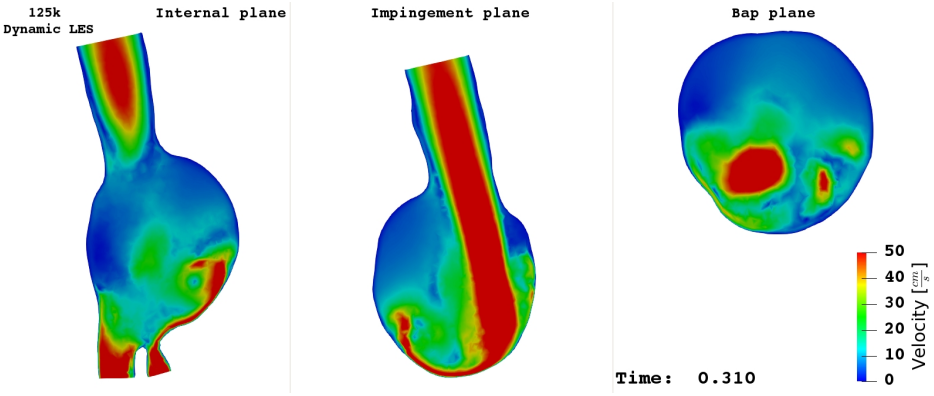

(c) Dynamic-σ.

Figure 5.11: Velocity field at Mid deceleration point on Internal, Impingement, and Bag plane in DNS (a), Static-σ (b), and Dynamic-σ (c) simulation.

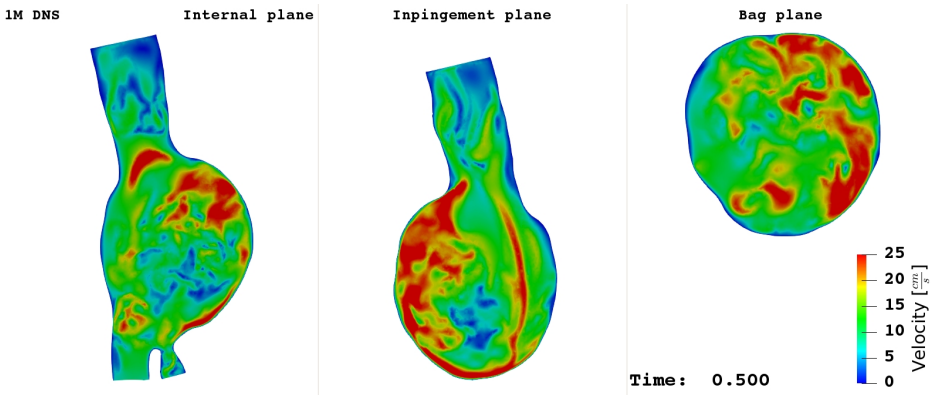

(a) DNS.

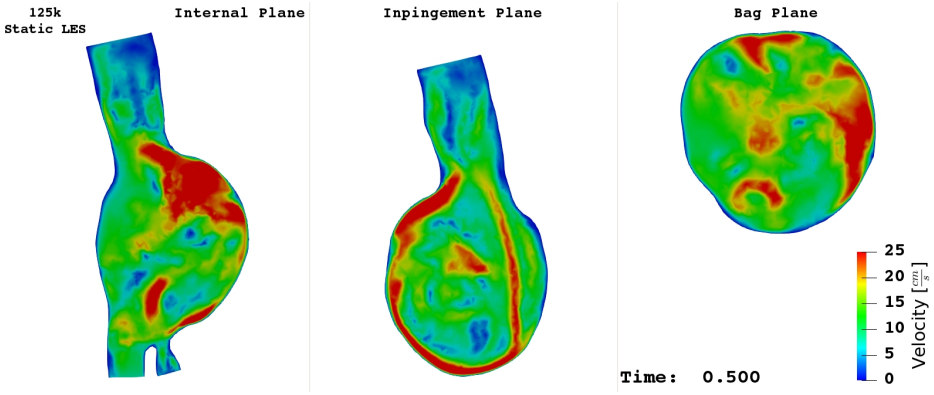

(b) Static-σ.

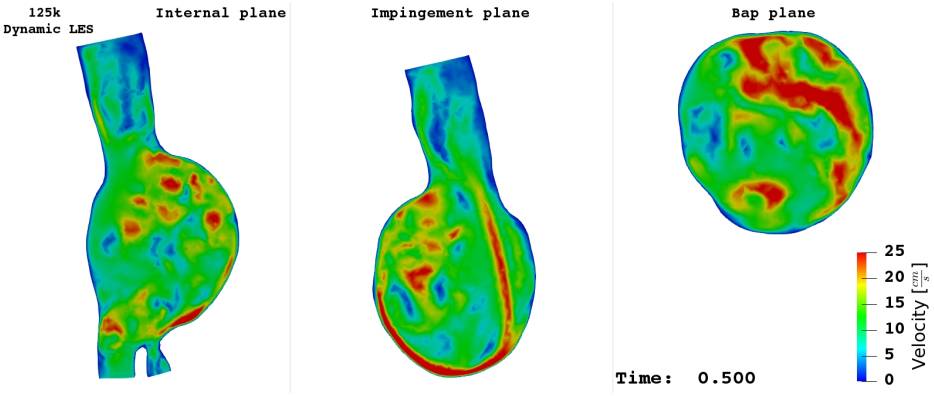

(c) Dynamic-σ.

Figure 5.12: Velocity field at Diastole on Internal, Impingement, and Bag plane in DNS (a), Static-σ (b), and Dynamic-σ (c) simulation. Notice that the halved colorbar with respect to the Figure at the Systole and Mid-deceleration point.

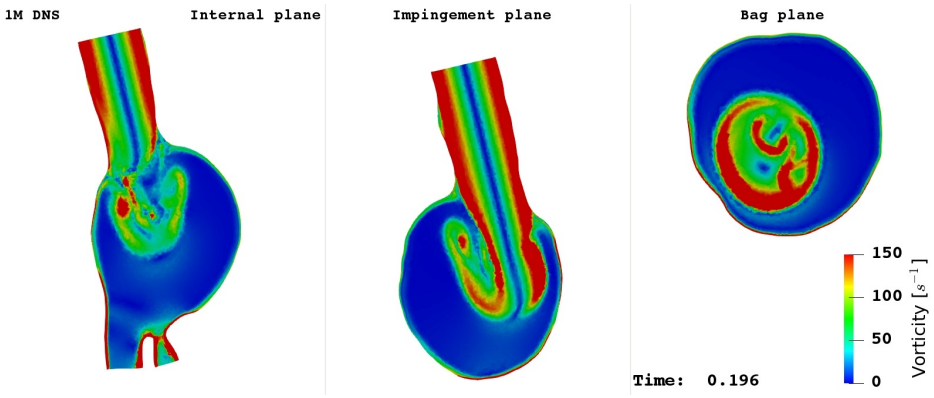

(a) DNS.

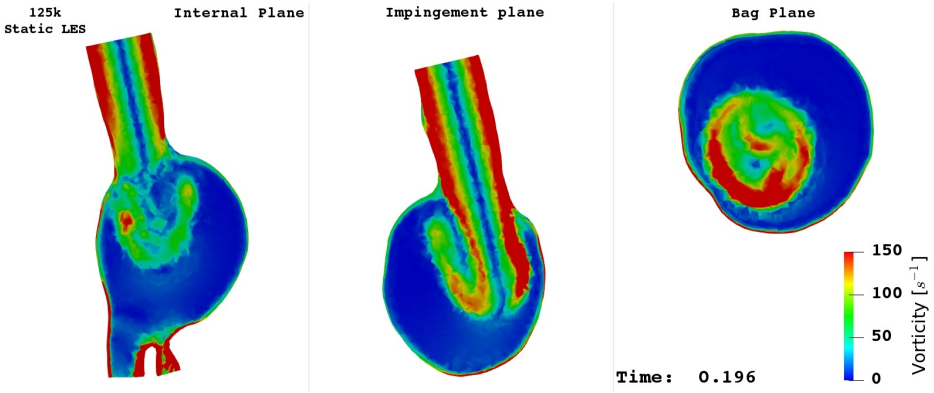

(b) Static-σ.

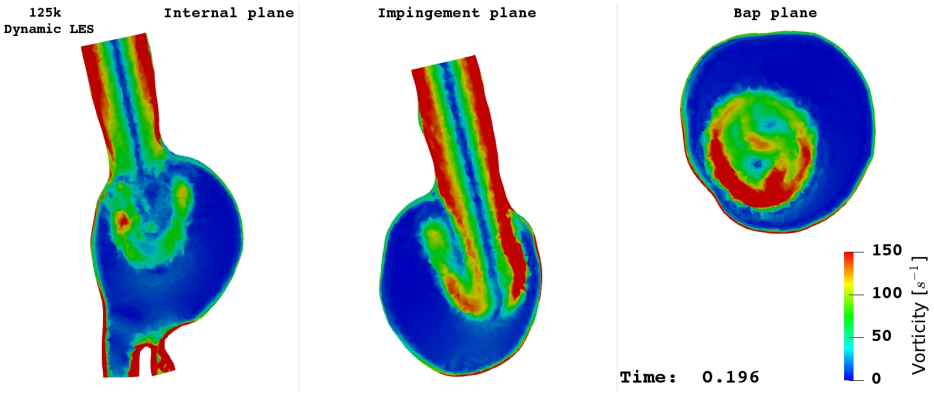

(c) Dynamic-σ.

Figure 5.13: Vorticity field at Systole on Internal, Impingement, and Bag plane in DNS (a) Static-σ (b) and Dynamic-σ (c) simulation.

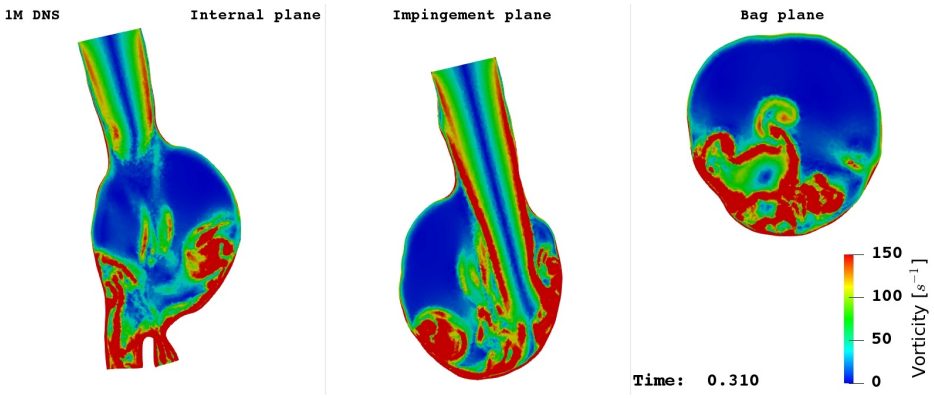

(a) DNS.

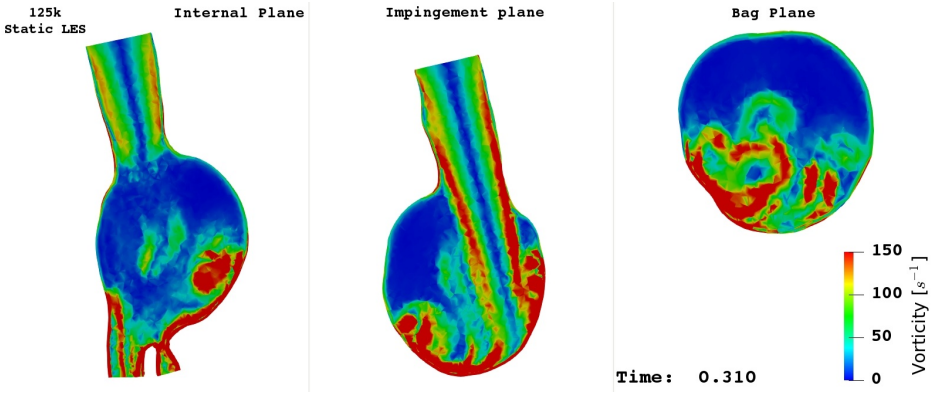

(b) Static-σ.

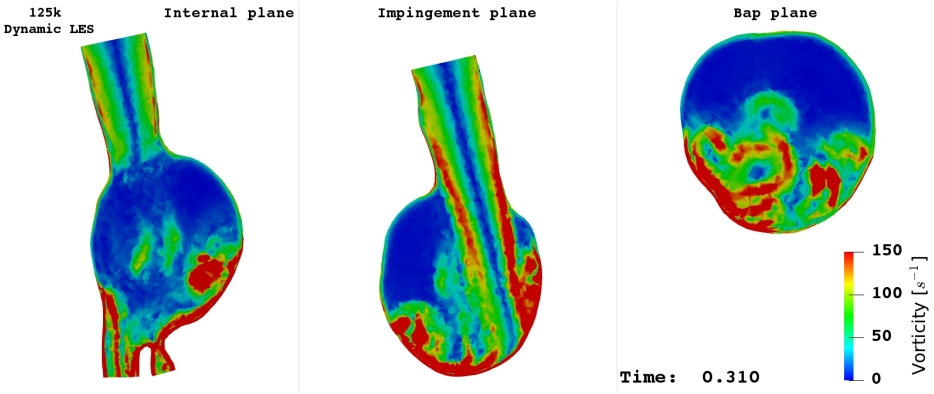

(c) Dynamic-σ.

Figure 5.14: Vorticity field at Mid deceleration point on Internal, Impingement, and Bag plane in DNS (a), Static-σ (b), and Dynamic-σ (c) simulation.

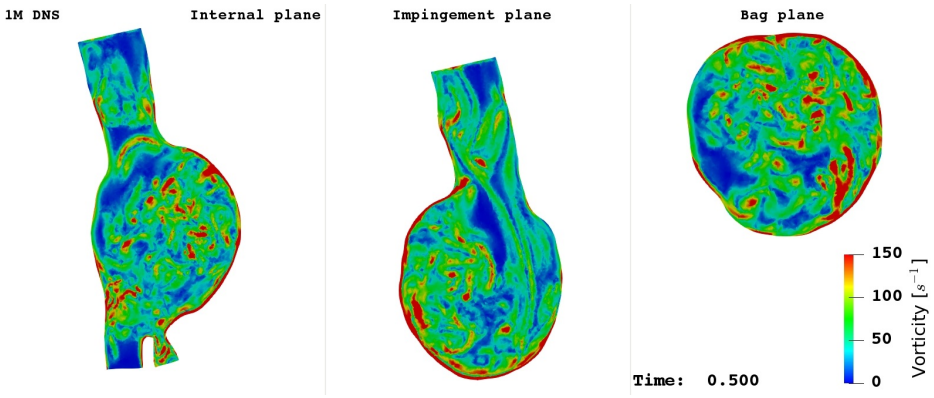

(a) DNS.

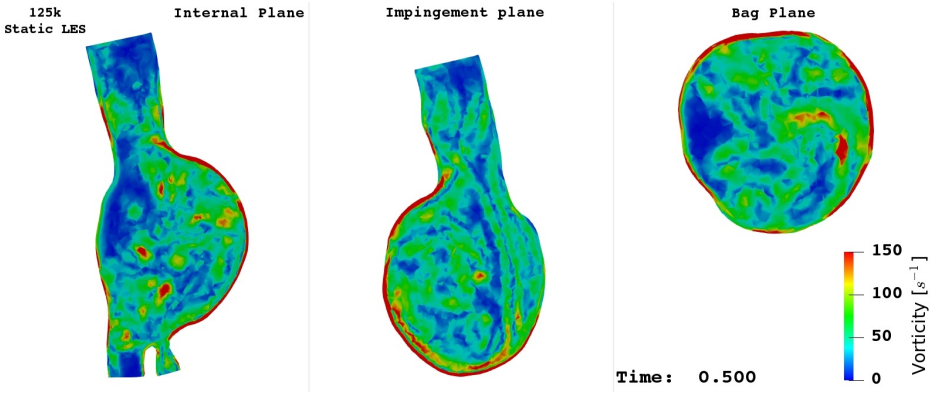

(b) Static-σ.

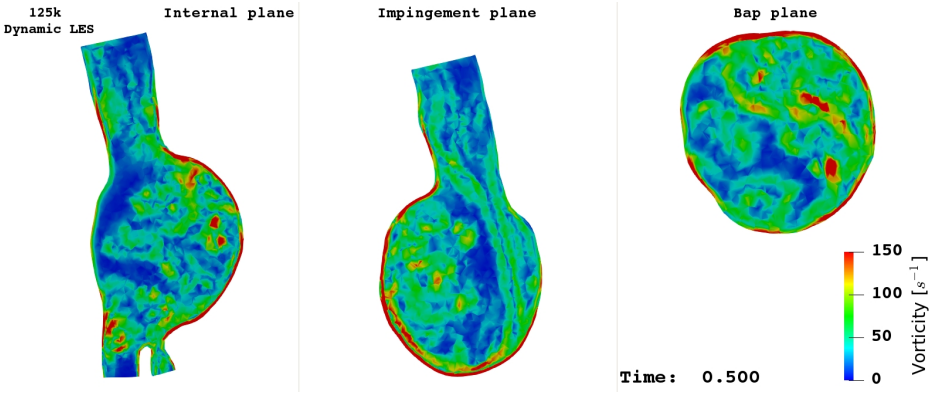

(c) Dynamic-σ.

Figure 5.15: Vorticity field at Diastole on Internal, Impingement, and Bag plane in DNS (a), Static-σ (b), and Dynamic-σ (c) simulation.

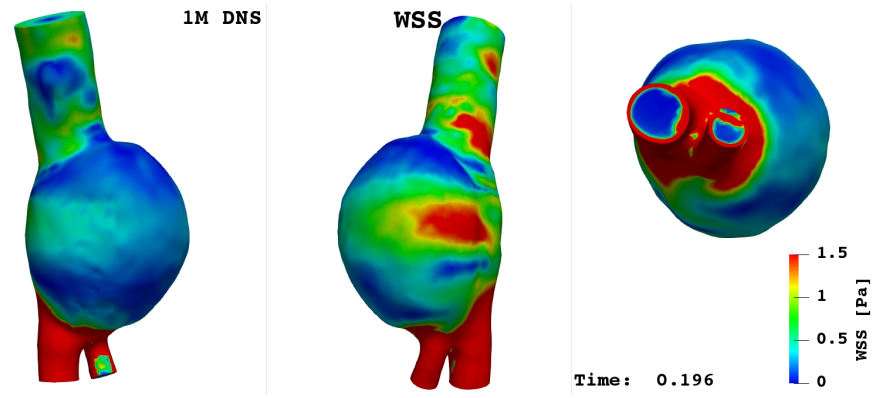

(a) DNS.

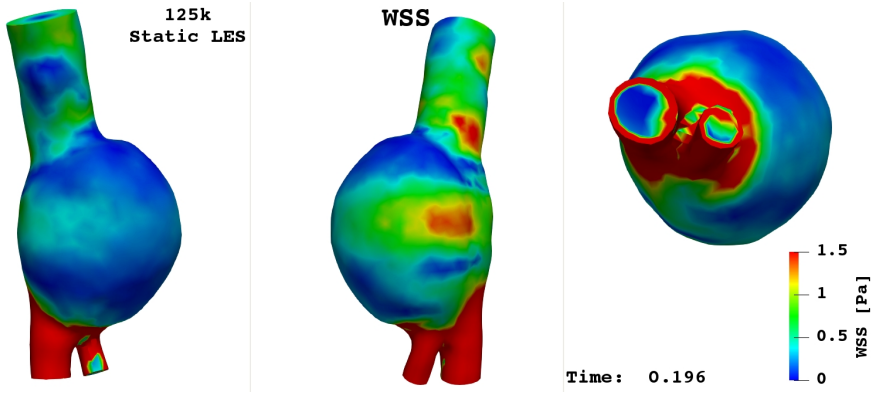

(b) Static-σ.

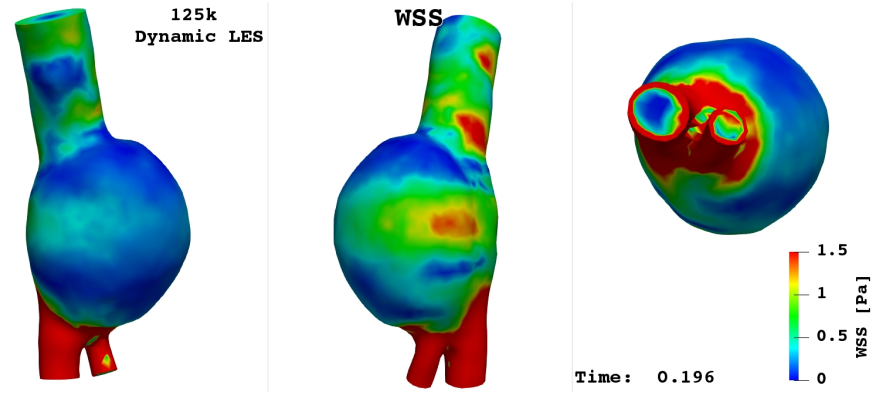

(c) Dynamic-σ.

Figure 5.16: Wall Shear stress (for different views) at Systole in DNS (a), Static-σ (b), and Dynamic-σ (c) simulation.

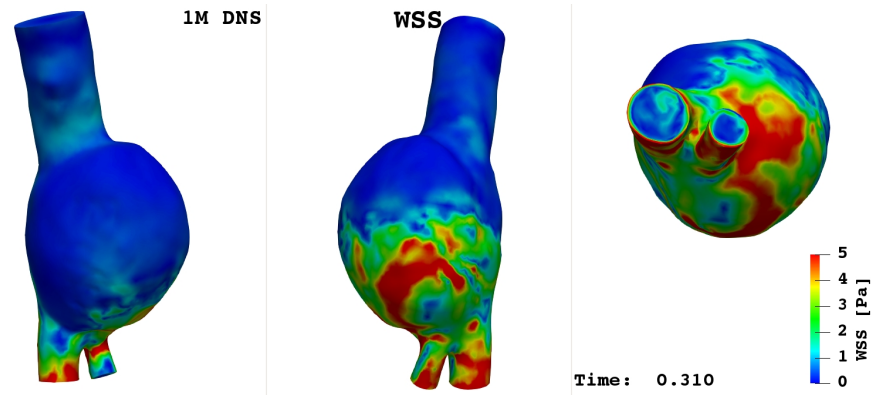

(a) DNS.

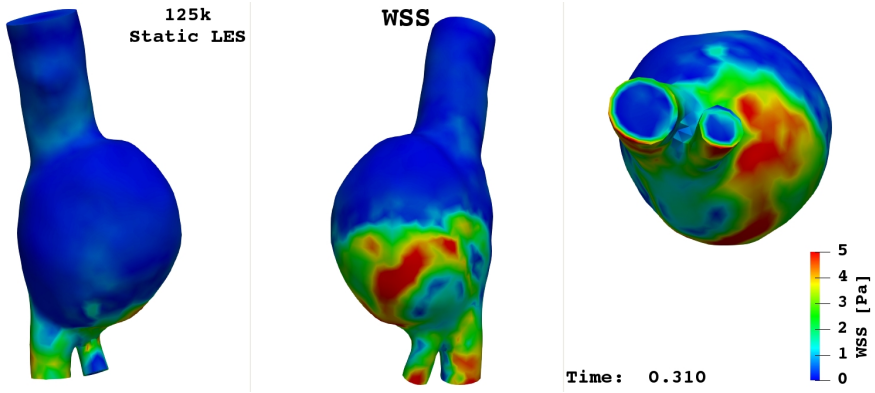

(b) Static-σ.

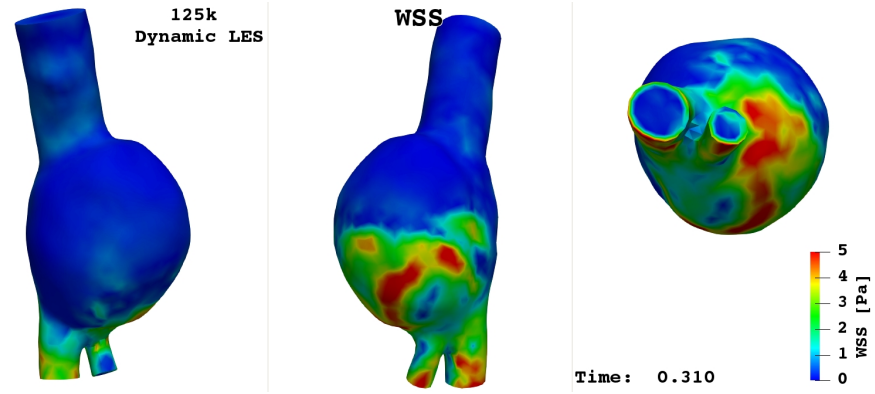

(c) Dynamic-σ.

Figure 5.17: Wall Shear stress (for different views) at Mid deceleration point in DNS (a), Static-σ (b), and Dynamic-σ (c) simulation.

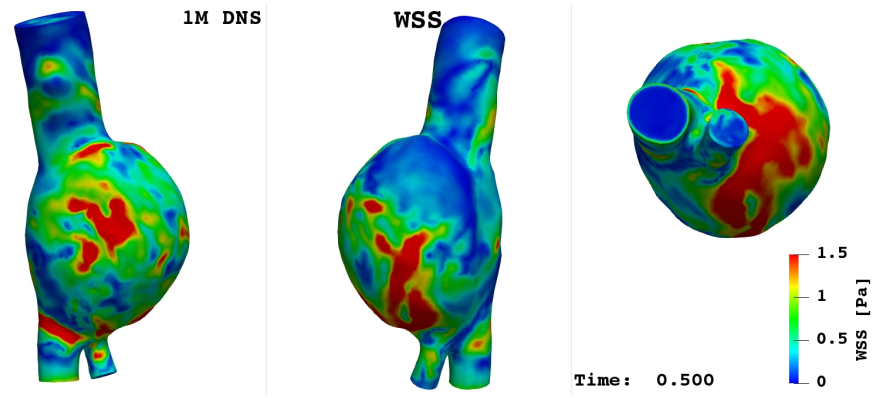

(a) DNS.

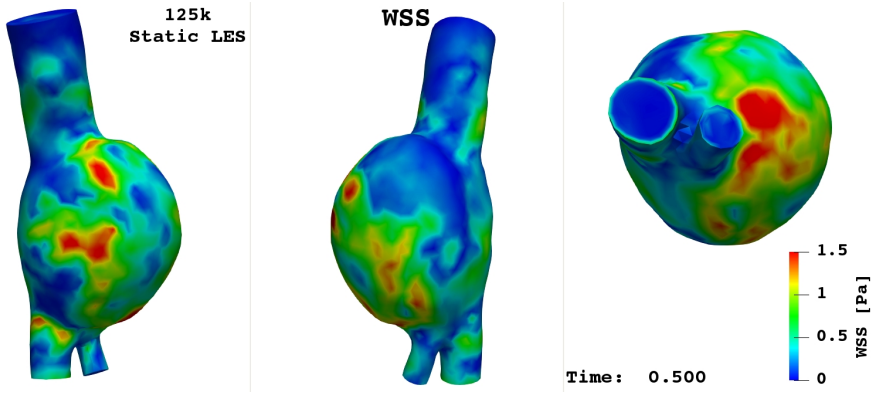

(b) Static-σ.

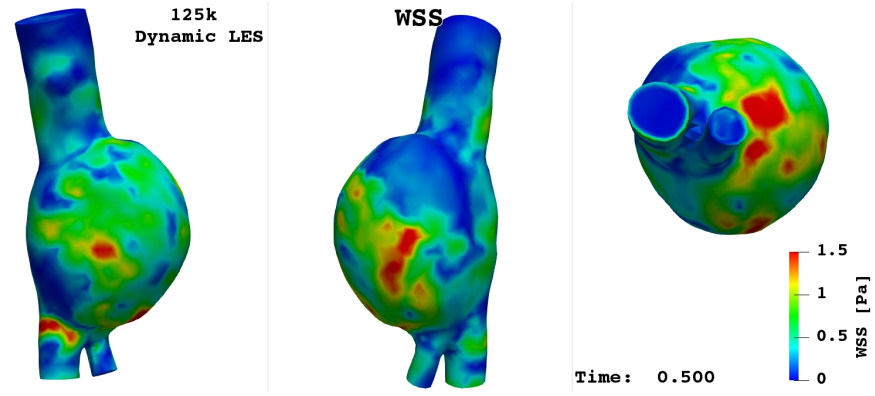

(c) Dynamic-σ.

Figure 5.18: Wall Shear stress (for different views) at Diastole in DNS (a), Static-σ (b). and Dynamic-σ (c) simulation.

To better investigate the blood dynamics and in particular the transitional effects in the AAA geometry, we introduce the following operators and post-processed quantities:

- *Ensemble-Average*: given a quantity $f(t, \mathbf{x})$, we define its ensemble-average as

$$< f(t, \mathbf{x}) >= \frac{1}{N_c} \sum_{i=1}^{N_c} f\big(\mathbf{x}, t + (i-1)T_{hb}\big).$$

  This allows us to remove from the field of interest the random, zero-time-mean fluctuations due to the transitional effects appearing at each heartbeat. In this thesis, we consider the ensemble-average of the velocity field along a line in the Impingement plane (see Figure 5.24). Six cardiac cycles were simulated, $N_c = 6$.

- *TAWSS*, Time Averaged Wall Shear Stress: the *TAWSS* is the integral over some period (in particular we consider the interval $[T_{hb}, 3T_{hb}]$) of the magnitude of the WSS

$$TAWSS = \frac{1}{2T_{hb}} \int_{T_{hb}}^{3T_{hb}} |\mathbf{WSS}| dt$$

- *Q-criterion*: the scalar field Q is defined as

$$Q(t, \mathbf{x}) = \frac{1}{2} \left[\sum_{i,j} \Omega_{ij}^2(t, \mathbf{x}) - S_{ij}^2(t, \mathbf{x}) \right],$$

  where $\mathbf{\Omega}$, $\mathbf{S}$ are the skew-symmetric and the symmetric part of the velocity gradient tensor, respectively: $\mathbf{\Omega} = \frac{\nabla \mathbf{u} - (\nabla \mathbf{u})^T}{2}$, $\mathbf{S} = \frac{\nabla \mathbf{u} + (\nabla \mathbf{u})^T}{2}$. The *Q-criterion* consists in analyzing the iso-contours of the positive part of Q with the aim of visualizing the coherent vortex structures. Indeed, positive values of Q indicate locations where rotations dominates over strain and shear. This allows us to identify regions where vortical structures are present. In particular, we plot the iso-contours corresponding to $Q \geq 5000$ (see Figures 5.20, 5.21, 5.22) and color them according to the velocity magnitude.

- *Global Kinetic Energy*, $K(t)$, defined as the ensemble average of the total Kinetic Energy:

$$K(t) = \frac{1}{2} \rho \int_\Omega \frac{1}{M} \sum_{i=1}^{N_c} |\mathbf{u}(t + (i-1)T_{hb}, \mathbf{x})|^2 d\Omega.$$

These quantities give an insight into the main characteristics of the periodic blood flow. In particular, by studying them, we can identify the regions where the flow experiences the highest variability among different cycles, which can be an indicator of transition to turbulence.

In figure (5.19) we show the TAWSS patterns which are similar for all the simulations. The regions with the most pronounced differences are the front and the distal parts of the AAA bulge wall (see pictures in the middle in Figures 5.19). Nonetheless, the LES simulations seem to underestimate the $TAWSS$, all the simulation shown the same patterns. In particular the dynamic-σ underestimates the $TAWSS$ with respect to the static-σ simulation.

In Figures 5.20, 5.21, 5.22 we plot the vortical structures identified by means of the *Q-criterion*. In all the simulation (DNS and LES) we have the formation of a vortex ring at the systolic peak (see Figure 5.20) which impinges the AAA sac at the mid deceleration phase (see Figure 5.21) and, after the breakage, partially exits through the iliac outlets (see Figure 5.22), as also observed in [20]. The DNS is able to capture more coherent structure with the respect of LES models, especially in the Diastolic peak (see Figure 5.22). This greater resolution power of the DNS for the *Q-criterion* can be explained recalling the enstrophy spectrum of turbulent flows. The enstrophy, Z, can be described as the integral of the square of the vorticity

$$Z(\omega) = \frac{1}{2}\int_{\Omega} \omega^2 \, d\Omega.$$

In K41 theory the enstrophy spectrum goes like

$$Z(k) = E(k)k^2 \sim k^{1/3},$$

where we recalled that in K41 the energy spectrum goes like $k^{-5/3}$. So, in doing the LES models filtering operation, we are not considering the last part of the enstrophy spectrum which is a an increasing function of k. Hence, the *Q-criterion* of the DNS, which is a quantity directly related to the vorticity, is able to capture more coherent structures particularly in the diastolic peak. This more resolution power of the DNS can be seen also looking at the vorticity field in the diastolic peak (see Figure 5.15).

In Figure 5.23a we report the time evolution of the Kinetic Energy over six heartbeats for all the simulations (DNS, σ-static, and σ-dynamic). In Figure 5.23b we show the Global kinetic energy over the mean period. We observe that, the peak value is reached during the mid-deceleration phase ($t \sim 0.2 - 0.3s$). All the simulations are in perfect agreement, with the static-σ simulation more close to the DNS particularly after the systolic peak.

In Figure 5.24 we report the Ensemble Average Velocity magnitude along a line in the Impingement plane, at systolic peak (Figure 5.24a), mid deceleration point (Figure 5.24b), and Diastolic peak (Figure 5.24c). In the systolic phase there is a very good agreement between the simulations (see Figure 5.24a). This is not surprising since at this location we are in laminar regime. Also at the mid deceleration point (where the transitional effects are relevant) we can observe agreement between the LES models and the DNS-reference simulation (see Figure 5.24b). During the Diastolic peak there are some difference. Notwithstanding the ensemble average operation, the diastolic peak still presents significant fluctuations for all the simulations. This means that six heartbeats are not enough to remove most of the fluctuations. A better investigation should be done making the ensemble average over more than six heartbeats. Notwithstanding these differences at the diastole, all the simulations seem to show the same trend (see Figure 5.24c).

From this further analysis we conclude that the DNS and the LES models show the same features in the transition of turbulence inside the AAA geometry which occur at the mid deceleration phase. In particular, we observed that all the reported quantities of interest, related to the formation of transitional effects, are higher during the mid deceleration phase.

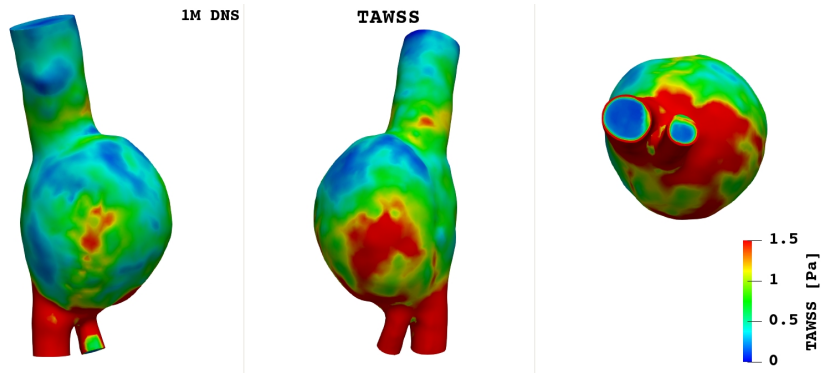

(a) DNS.

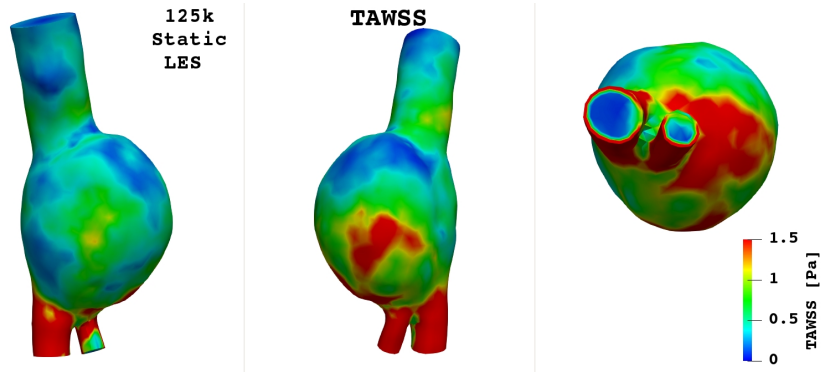

(b) Static-σ.

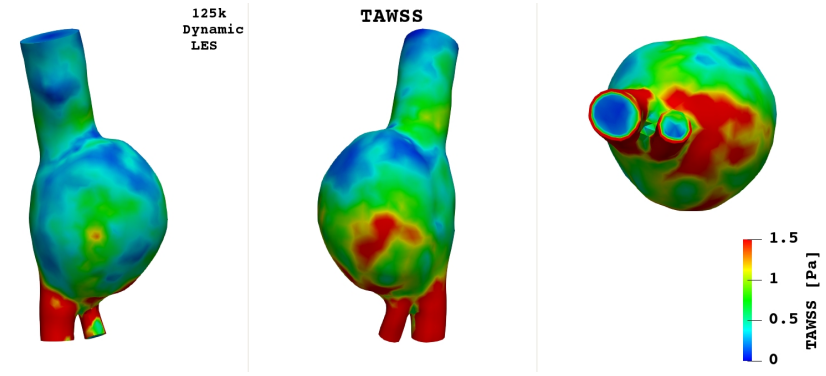

(c) Dynamic-σ.

Figure 5.19: Time Average Wall Shear stress (for different views) between $[T_{hb}, 3T_{hb}]$ in DNS (a), Static-σ (b), and Dynamic-σ (c) simulation.

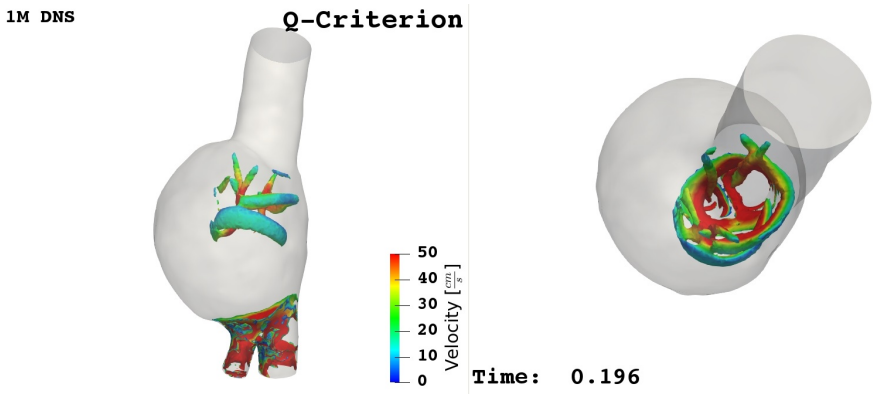

(a) DNS.

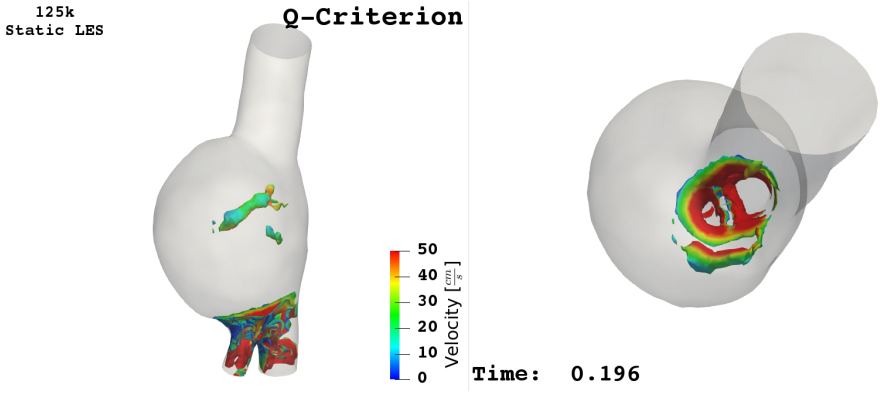

(b) Static-σ.

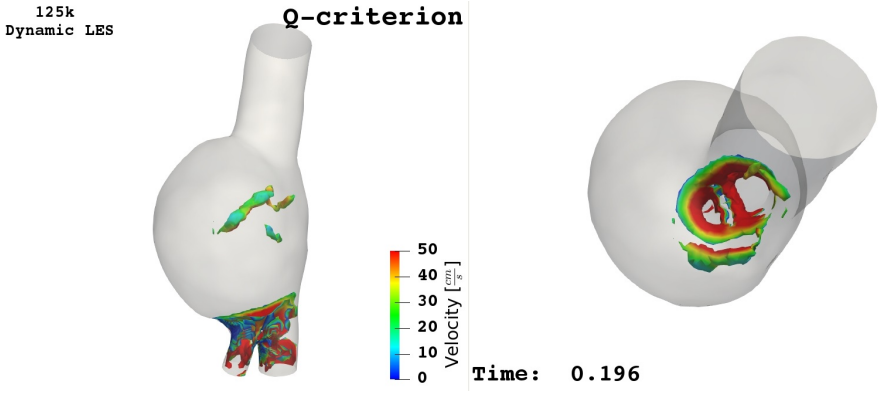

(c) Dynamic-σ.

Figure 5.20: Q-criterion (different views), colored by velocity, at Systole in DNS (a), Static-σ (b), and Dynamic-σ (c) simulation.

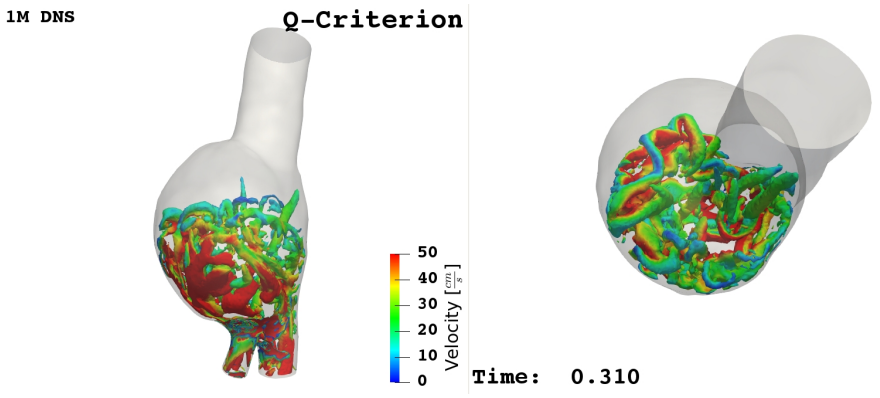

(a) DNS.

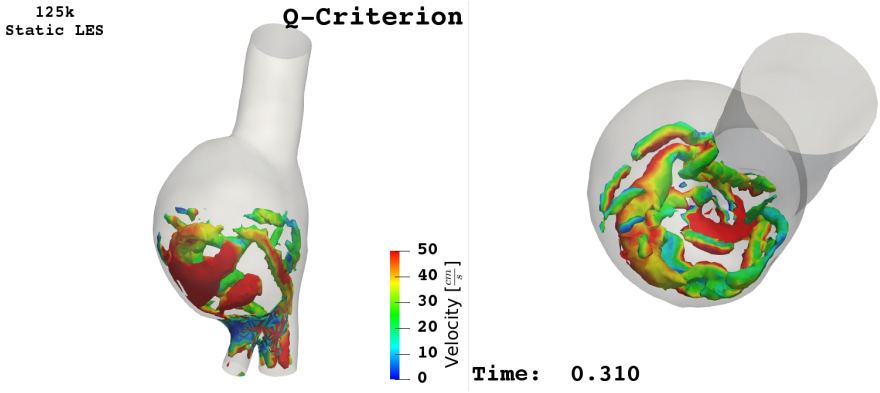

(b) Static-σ.

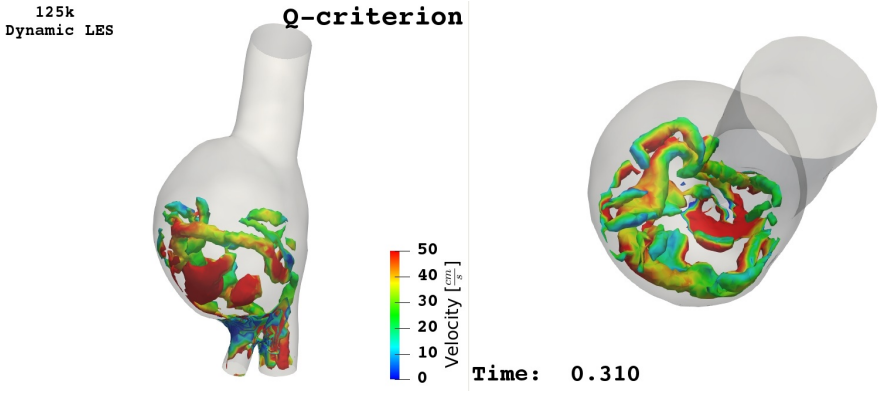

(c) Dynamic-σ.

Figure 5.21: Q-criterion (different views), colored by velocity, at Mid deceleration point in DNS (a), Static-σ (b), and Dynamic-σ (c) simulation.

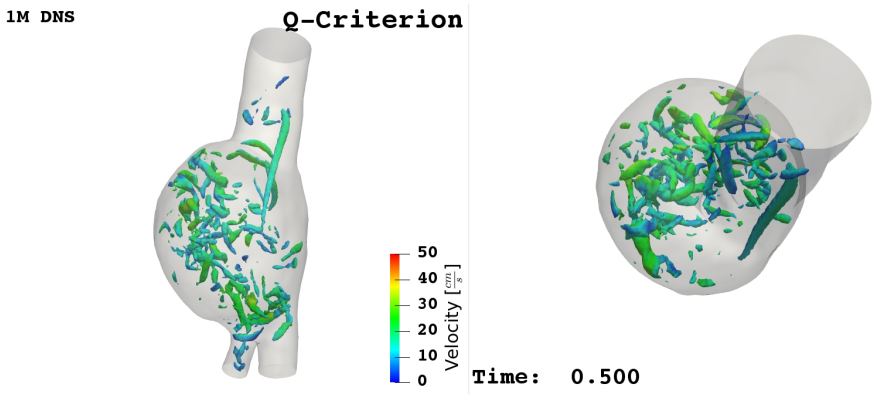

(a) DNS.

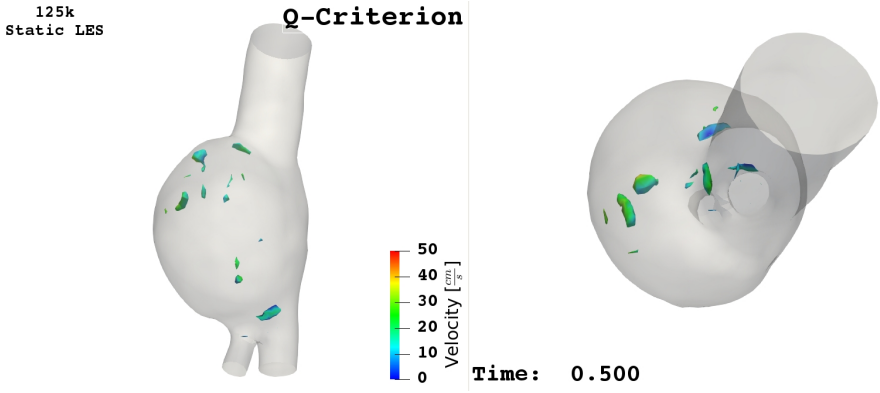

(b) Static-σ.

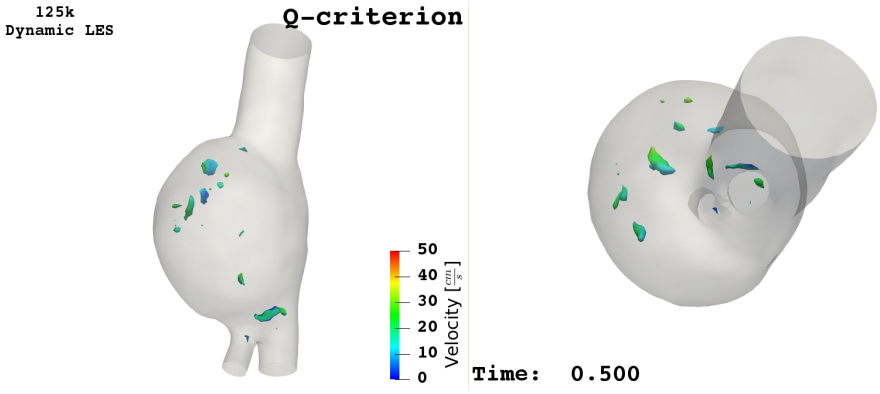

(c) Dynamic-σ.

Figure 5.22: Q-criterion (different views), colored by velocity, at Diastole in DNS (a), Static-σ (b), and Dynamic-σ (c) simulation.

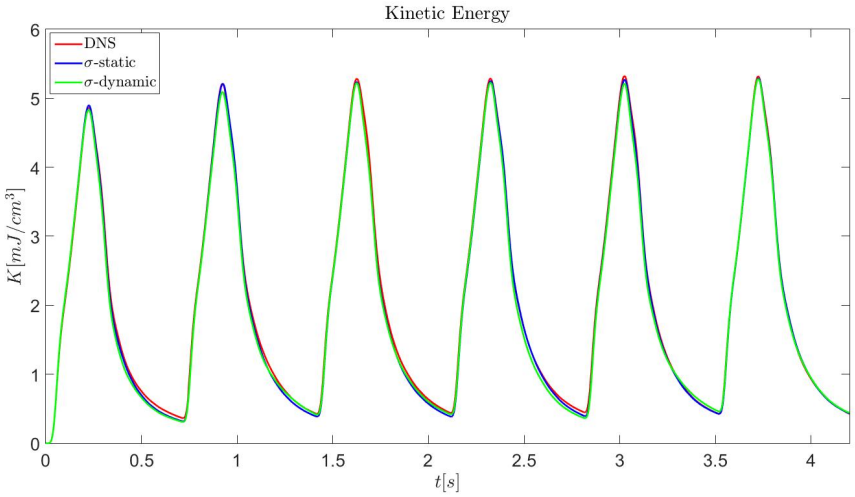

(a) Kinetic Energy on $[0, 6T_{hb}]$

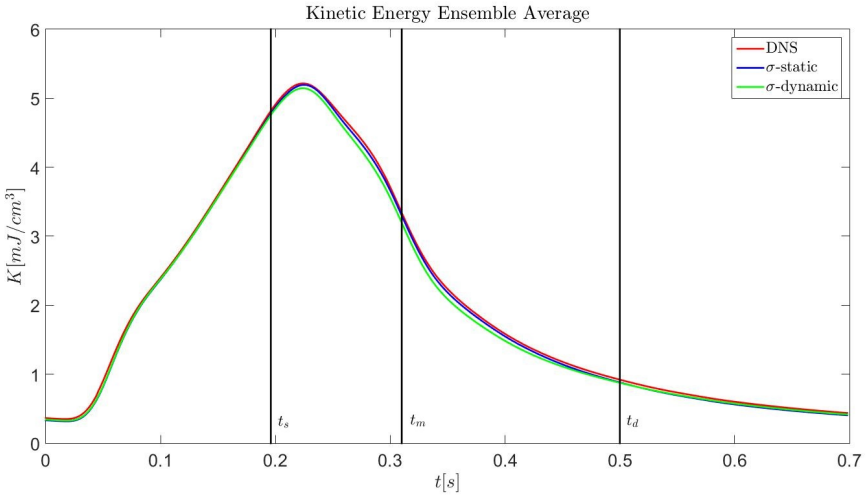

(b) Ensemble Average Kinetic Energy.

Figure 5.23: Kinetic Energy (a) and Global Kinetic Energy (b) for DNS (in red), Static-σ (in blue), and Dynamic-σ (in black) simulation.

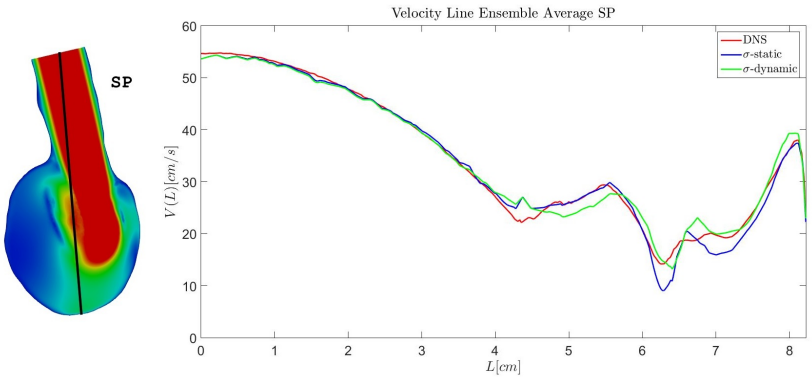

(a) Systole.

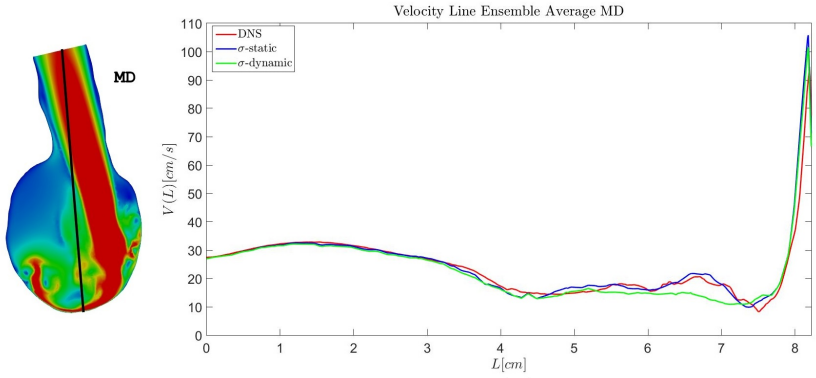

(b) Mid deceleration point.

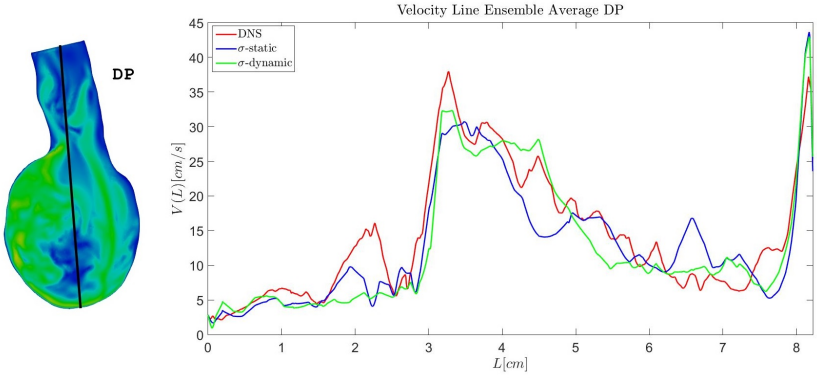

(c) Diastole.

Figure 5.24: Ensemble Average Velocity magnitude at Systole (a), Mid deceleration point (b), and Diastole(c) along a line (shown in black) on the Impingement plane for DNS (in red), Static-σ (in blue), and Dynamic-σ (in black) simulation.

5.5 Turbulent Viscosity

We observed that the use of LES models leads to differences with respect to the DNS-no model simulation after the mid deceleration point. This discrepancy is due to the fluctuating process which should be included in the turbulent viscosity term related to the LES model. For this reason, in the σ-static simulation we investigated, where and when the turbulent viscosity ν_{sgs} is active.

In Figure 5.26 we report the ratio between the subgrid-scale viscosity and the molecular one ($\frac{\nu_{sgs}}{\nu}$) along the usual sliced plane (Internal, Impingement, and Bag plane) at systolic peak (Figure 5.26a), mid deceleration point (Figure 5.26b), and diastolic peak (Figure 5.26c). The subgrid-scale viscosity reaches values up to five times the molecular one.

In Figure 5.27 we visualize, on the Impingement plane, the velocity field (on the left) and the turbulent viscosity (on the right), at the systole (Figure 5.27a), mid deceleration point (Figure 5.27b), and diastole (Figure 5.27c). From these Figures we can observe how the LES model correctly turns off when the shear layer enters in the AAA bulge (see Figure 5.27a), while it activates when the shear layer, impacting on the aneurysmatic wall, begins to produce vortical structures (see Figures 5.27b). Turbulent viscosity still remains active also during the diastolic phase, when highly fluctuating velocity field is present in the AAA geometry (see Figure 5.27c).

Figure 5.28 shows the contour surface of the turbulent viscosity ($\frac{\nu_{sgs}}{\nu} \geq 3$) at the systolic peak (Figure 5.28a), mid deceleration point (Figure 5.28b), and diastolic peak (Figure 5.28c). Regions with large turbulent viscosity reach the maximal filling, inside the aneurysmatic bulge, at the mid deceleration point (see Figure 5.28b).

In Figure 5.29 we report the turbulent viscosity ($\frac{\nu_{sgs}}{\nu}$) along the streamlines at the systolic peak (Figure 5.29a), mid deceleration point (Figure 5.29b), and diastolic peak (Figure 5.29c). We can observe how turbulent viscosity is concentrated along some vortical streamline structures, in particular those near the impingement zone (Figure 5.29b, 5.29c).

In Figure 5.30 we report the ensemble average turbulent viscosity ($\frac{\nu_{sgs}}{\nu}$) along the Impingement plane line (see Figure 5.24) for the σ-static and σ-dynamic simulation, at the systolic peak (Figure 5.30a), mid deceleration point (Figure 5.30b), and diastolic peak (Figure 5.30c). There is a marked difference between the σ-static and σ-dynamic turbulent viscosity, mainly because the dynamic ν_{sgs} can take negative values, which correspond to the backscatter phenomena. In fact, the backscatter percentage in the σ-dynamic simulation oscillates around the 45% (see Figure 5.25), in agreement with reported values in turbulent flows for the plane channel flow [105].

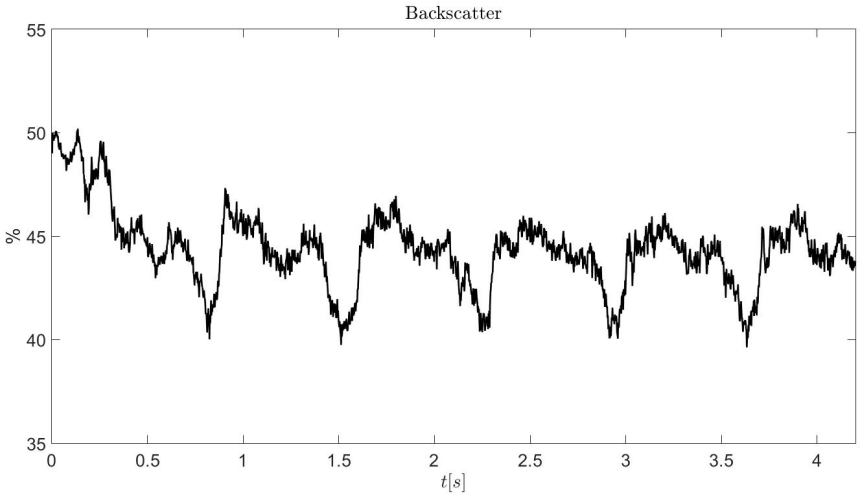

Figure 5.25: Backscatter percentage in the Dynamic-σ simulation.

Lastly, in Figure 5.31 we display the values of the C_σ coefficient, related to the turbulent viscosity, for the σ-static and σ-dynamic simulation. The dynamic C_σ coefficient is a very variable function of space and time, in particular during the systole (see Figure 5.31a). As we can see from Figure 5.31, six heartbeats are not enough to capture the average trend of C_σ. Moreover, these highly fluctuating values of C_σ could destabilize the solution destroying the numerical stability. Fortunately, in our case, after the systolic peak C_σ oscillates between a less wide range of values (see Figure 5.31b-5.31c).

From the turbulent viscosity analysis we found that the LES model is active, in particular during the mid-deceleration and early diastolic phases, with the subgrid-scale viscosity reaching values up to five times greater than those of the molecular viscosity. The regions with large values of the subgrid-scale viscosity are those where the flow is disturbed (high fluctuations of the velocity magnitude). On the other hand, the LES model switches itself essentially off in the laminar regions, unlike the Smagorinsky model, for example (as mentioned in Section 2.5). This confirms the suitability of the $\sigma-$LES models in this context, being able to turn on only where and when needed.

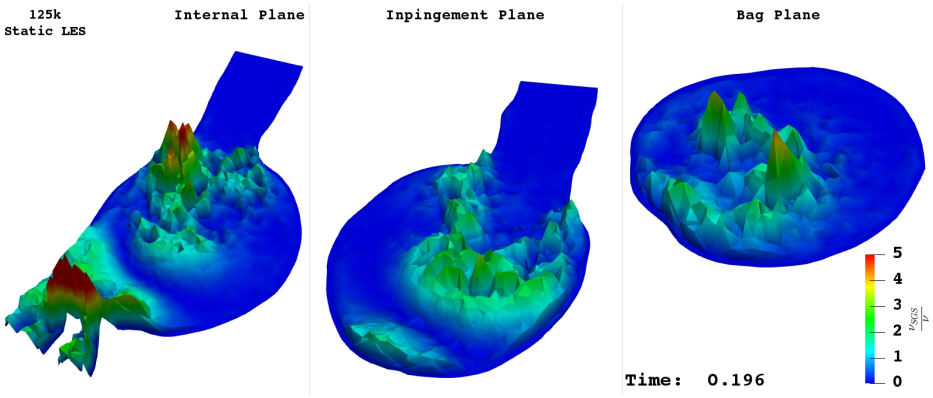

(a) Systole.

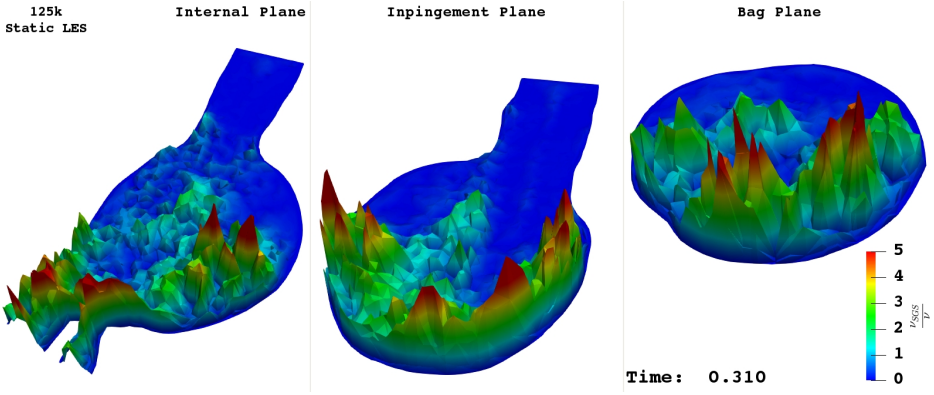

(b) Mid deceleration point.

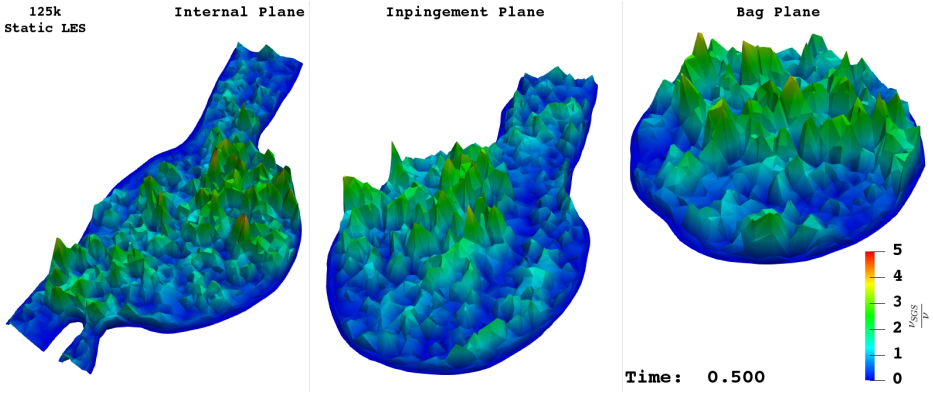

(c) Diastole.

Figure 5.26: Turbulent viscosity ($\frac{\nu_{sgs}}{\nu}$) at Systole (a), Mid deceleration point (b), and Diastole(c) on the Internal, Impingement, and Bag plane for the Static-σ simulation.

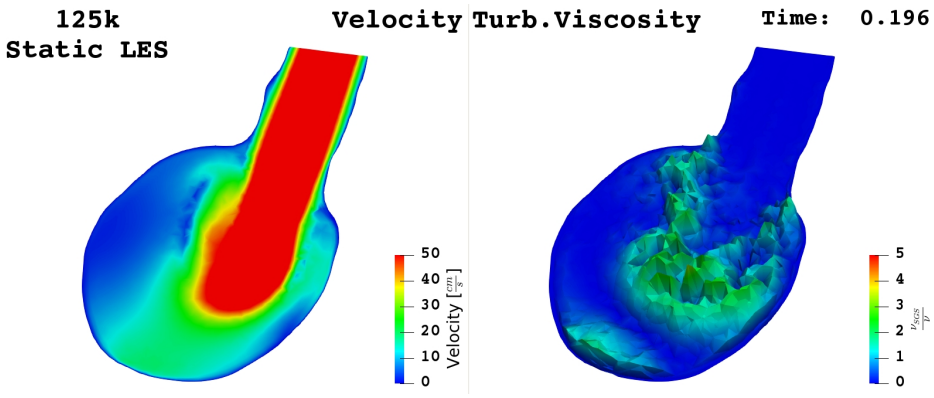

(a) Systole.

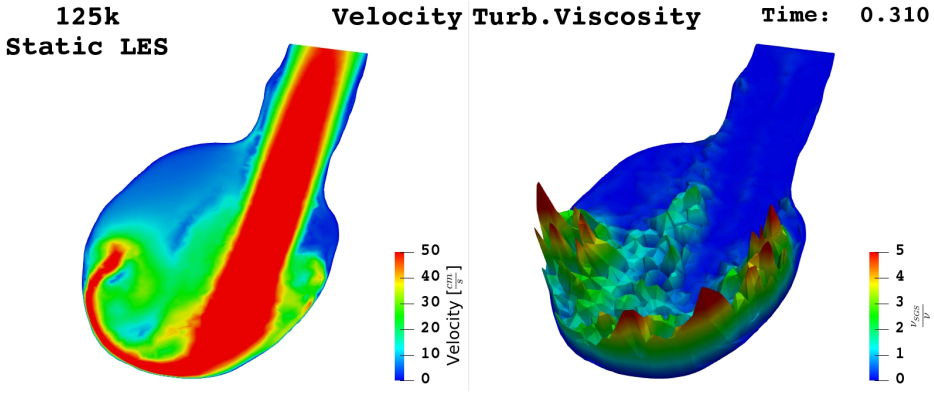

(b) Mid deceleration point.

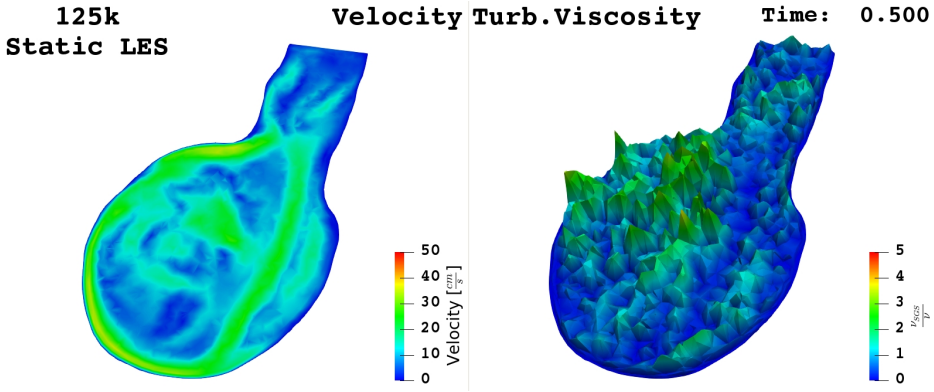

(c) Diastole.

Figure 5.27: Velocity field (on the left) and Turbulent viscosity (on the right) on the Impingement plane at Systole (a), Mid deceleration point (b), and Diastole(c) for the Static-σ simulation.

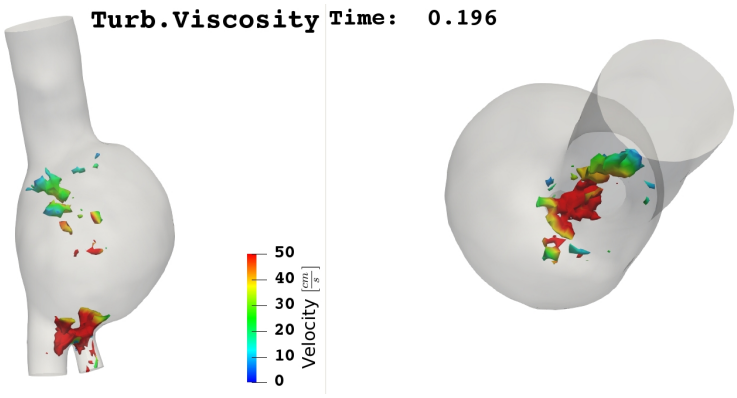

(a) Systole.

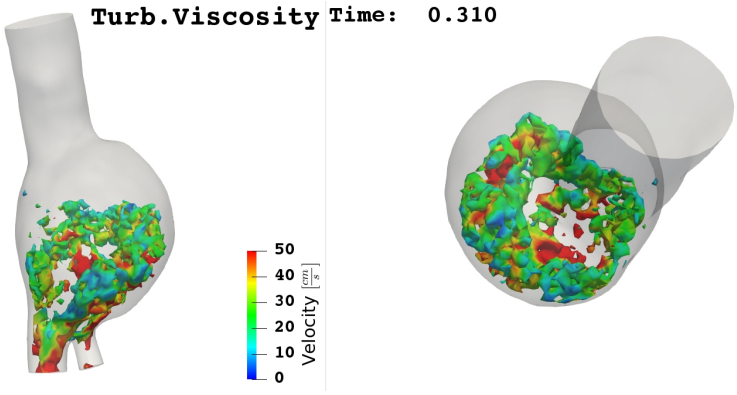

(b) Mid deceleration point.

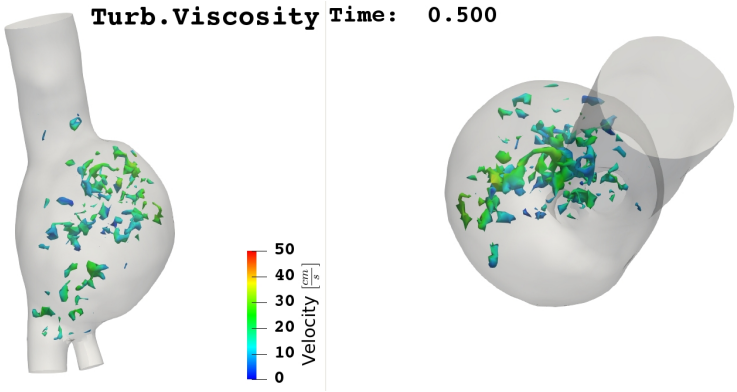

(c) Diastole.

Figure 5.28: Turbulent viscosity iso-surface ($\frac{\nu_{sgs}}{\nu} \geq 3$), colored by velocity, for the Static-σ simulation.

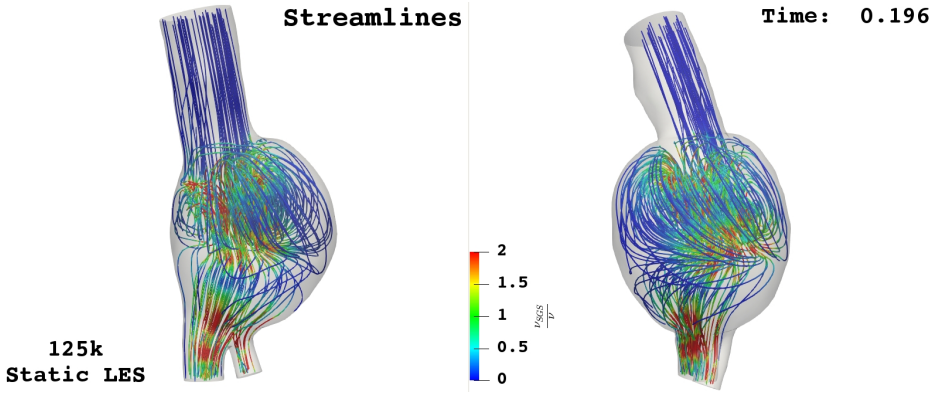

(a) Systole.

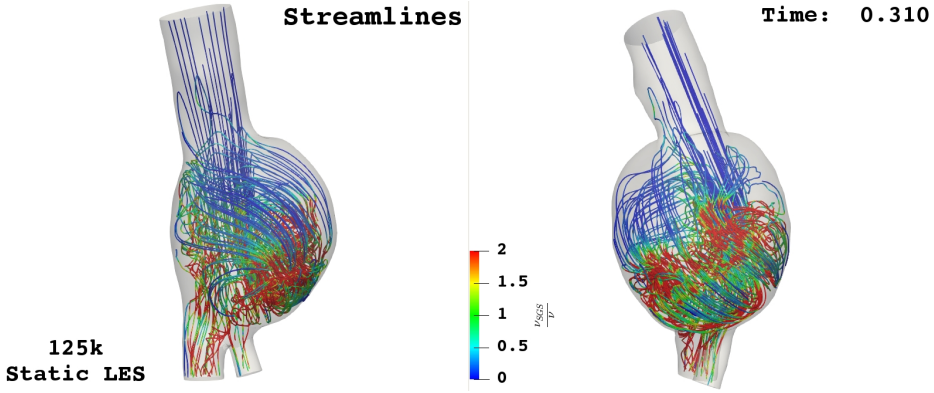

(b) Mid deceleration point.

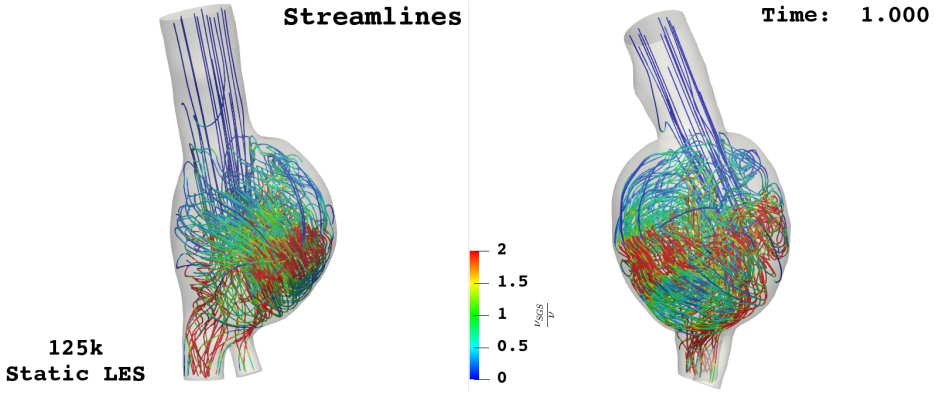

(c) Diastole.

Figure 5.29: Turbulent viscosity ($\frac{\nu_{sgs}}{\nu}$) along the streamlines at Systole (a), Mid deceleration point (b), and Diastole(c) for the Static-σ simulation.

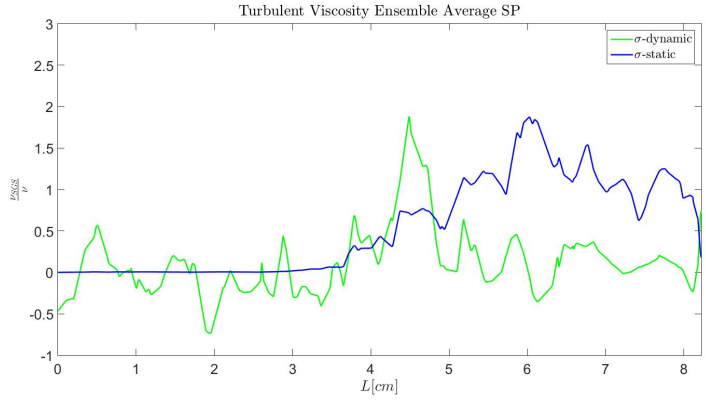

(a) Systole.

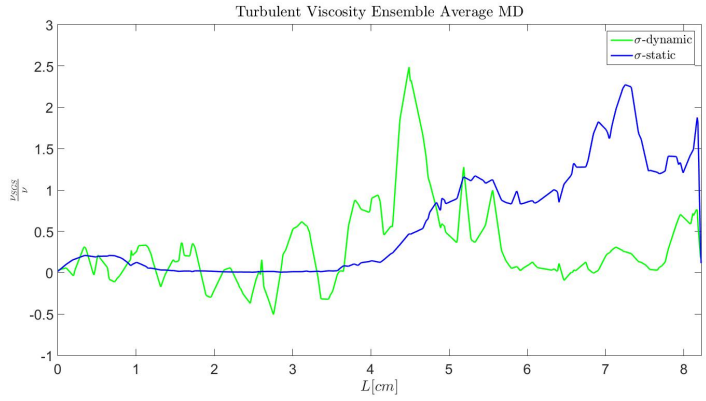

(b) Mid deceleration point.

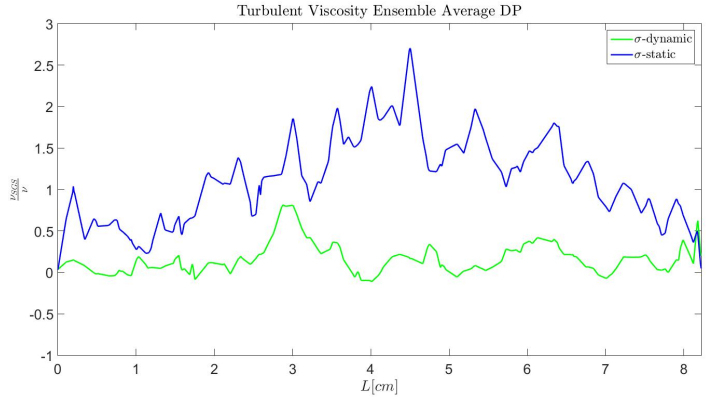

(c) Diastole.

Figure 5.30: Ensemble Average Turbulent viscosity ($\frac{\nu_{sgs}}{\nu}$) at Systole (a), Mid deceleration point (b), and Diastole(c) along the Impingement plane line for Static-σ (in blue), and Dynamic-σ (in black) simulation.

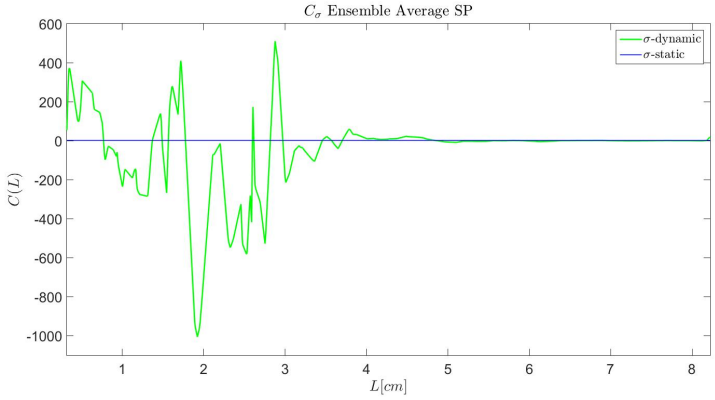

(a) Systole.

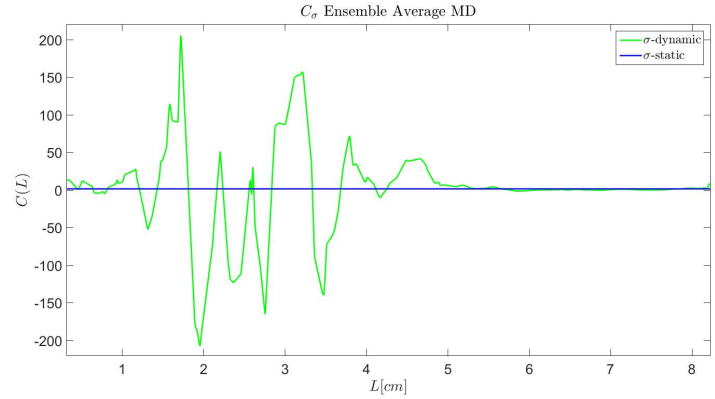

(b) Mid deceleration point.

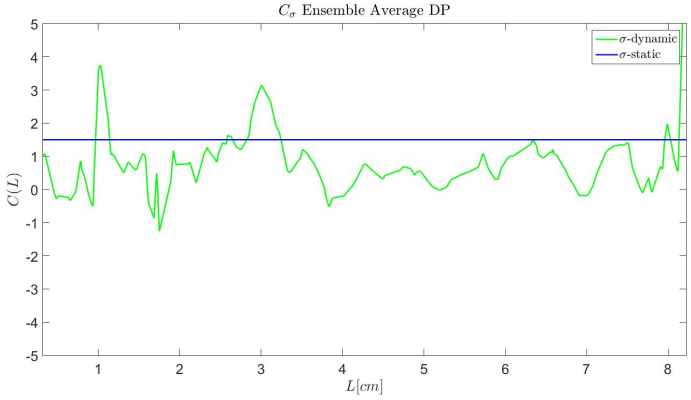

(c) Diastole.

Figure 5.31: Ensemble Average for the costant C_{sigma} at Systole (a), Mid deceleration point (b), and Diastole(c) along the Impingement plane line for Static-σ (in blue), and Dynamic-σ (in black) simulation.

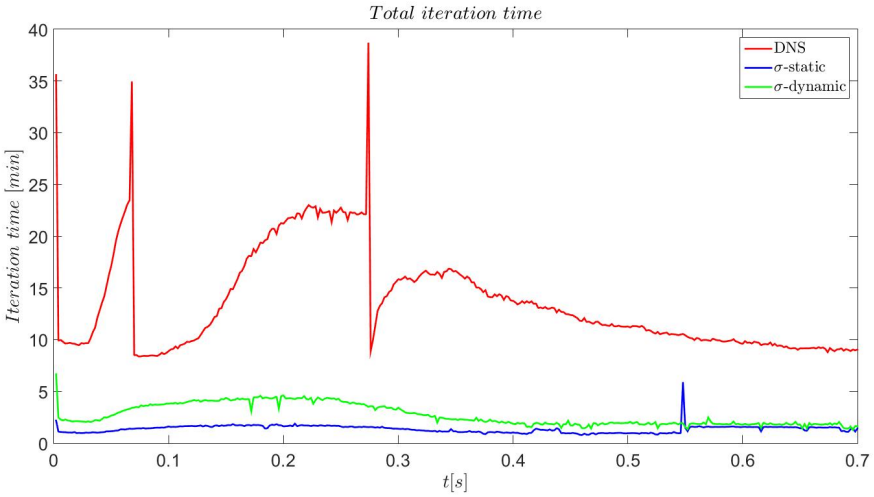

Figure 5.32: Total Iteration time for all the simulations.

5.6 Computational costs

Figure 5.32 shows the total iteration time, which is the time that the code needs to complete one time step (updating the NS matrix, computing the preconditioner, if needed, and solving the linear system) for the first heartbeat $(0 - 0.7s)$.

The spikes in Figure 5.32 correspond to the recalculation of the preconditioner. We chose to reuse the preconditioner of the previous time step if the linear system is solved in certain number of iteration, while it is recalculated if exceed this threshold.

In Figure 5.32 the total iteration time for the DNS simulation is about ten times bigger than those of static-σ and dynamic-σ. While, the total iteration time for the dynamic-σ is doubled with respect to the static-σ. Below, we report the mean total iteration time, $< t >$, and the total time to complete an heartbeat, T, for each simulation.

- $< t >_{DNS} \sim 13.6\, min \Longrightarrow T_{DNS} \sim 79.5\, hrs$;
- $< t >_{SS} \sim 1.36\, min \Longrightarrow T_{SS} \sim 7.9\, hrs$;
- $< t >_{DS} \sim 2.7\, min \Longrightarrow T_{DS} \sim 15.8\, hrs$.

From these results it is evident how a LES turbulence modeling approach strongly reduces the computational cost with respect to a DNS.

Appendix

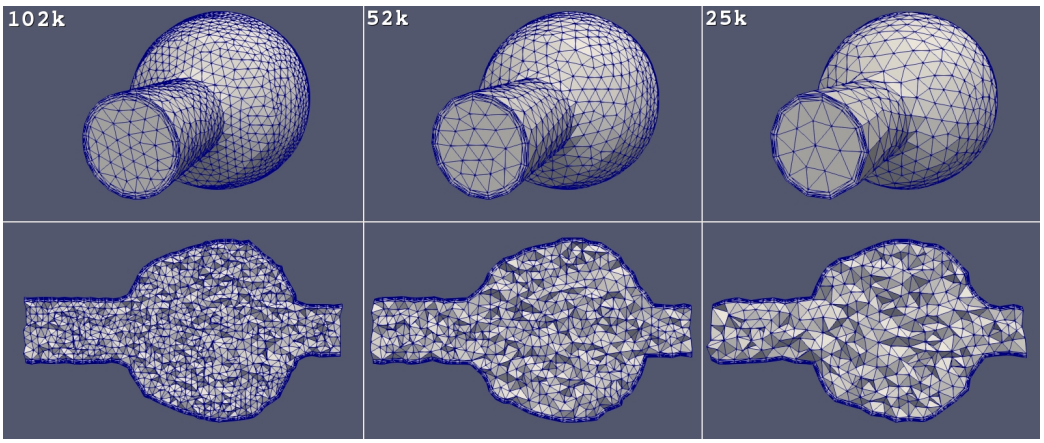

Figure 5.33: Meshes for different h.

5.7 LES Grid convergence study

We studied the behavior of the static-σ LES model for a grid refinement. We created an artificial surface similar to a real AAA geometry. Using the VMTK library, the built on purpose surface was turned into volumetric meshes of linear tetrahedra for different characteristic space discretization parameter. We obtained the following meshes (see Figure 5.33):

I $25K$ tetrahedra corresponding to $h = 0.55cm$;

II $52K$ tetrahedra corresponding to $h = 0.416cm$;

III $102K$ tetrahedra corresponding to $h = 0.32cm$.

In all the meshes we selected 3 boundary layers of thickness $s_{BL} = 0.13cm$ with ratio of $\delta s = 0.7$ between two successive layers. At the inlet we imposed

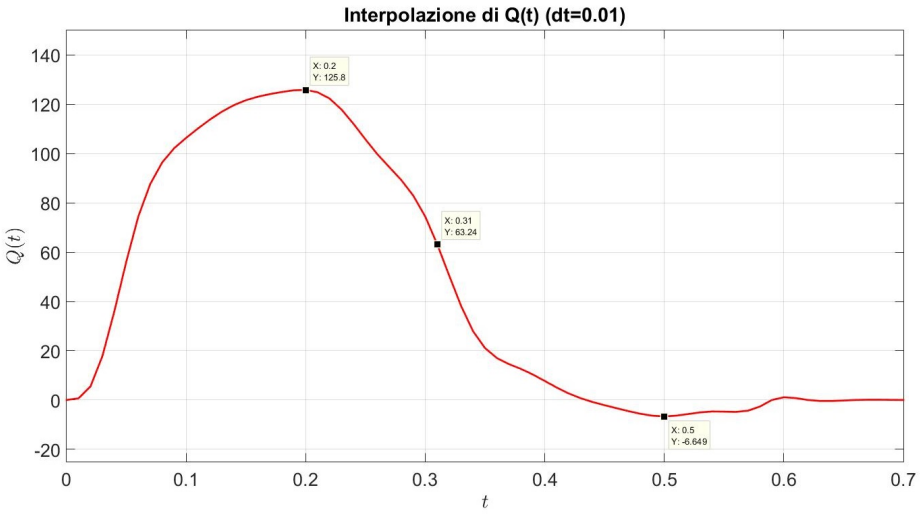

Figure 5.34: Meshes for different h.

a parabolic in space velocity profile with a time variation flow rate $Q(t)$ shown in Figure 5.34. At the outlet we prescribed the usual Robin non linear boundary condition characteristic of the Backflow stabilization, while on the lateral surface we imposed a zero velocity profile.

We used a BDF2 in time discretization with a $\delta t = 0.01s$ in combination with a $\mathbb{P}_2 - \mathbb{P}_2$ space discretization.

In Figure 5.35a we report the ratio between the turbulent viscosity and the molecular one ($\frac{\nu_{sgs}}{\nu}$) in the sliced middle plane for different mesh refinements ($25K$, $52K$, $102K$), at the systole (Figure 5.35a), mid deceleration point (Figure 5.35b), and diastole (Figure 5.35c) of the signal $Q(t)$ (see Figure 5.34).

Figure 5.36 shows the contour-surface of turbulent viscosity ($\frac{\nu_{sgs}}{\nu} \geq 4$) colored by velocity, at the systole (Figure 5.36a), mid deceleration point (Figure 5.36b), and diastole (Figure 5.36c), for different mesh refinements ($25K$, $52K$, $102K$).

Observing the Figures 5.35, 5.36, we can say that the contribution of the subgrid-scale modeling is, as expected, greater for the coarsest mesh in order to account for the higher frequency cutoff (introduced by the implicit filter). For a grid refinement the contribution of turbulent viscosity is smaller with respect to a coarser grid.

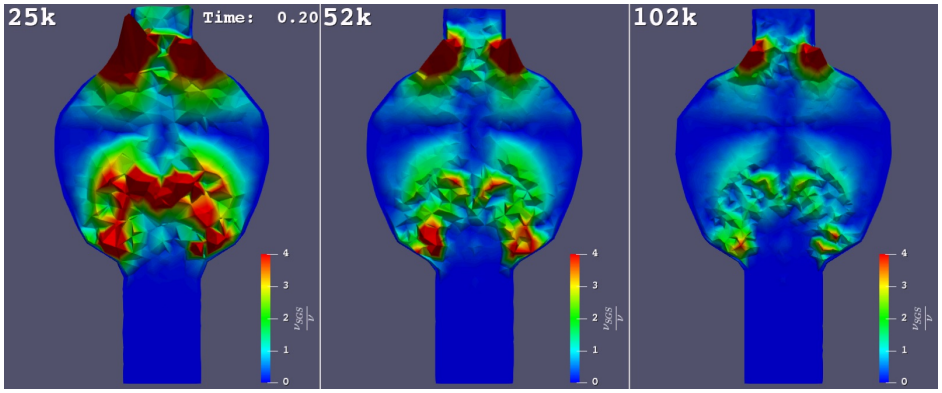

(a) Systolic peak.

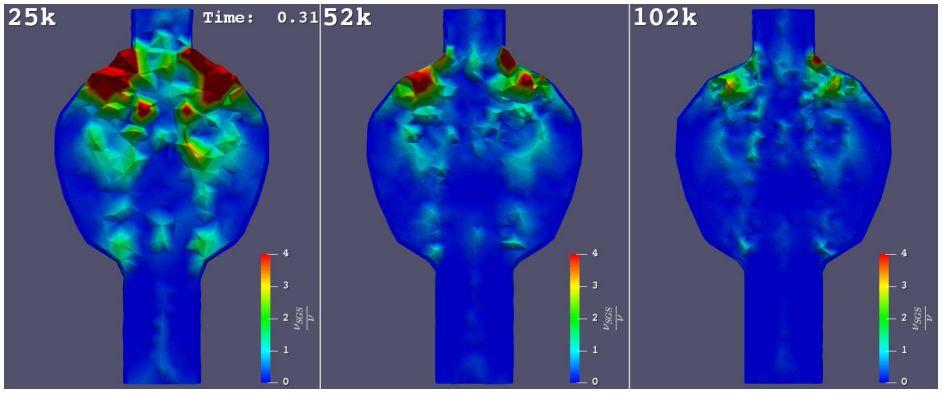

(b) Mid deceleration point.

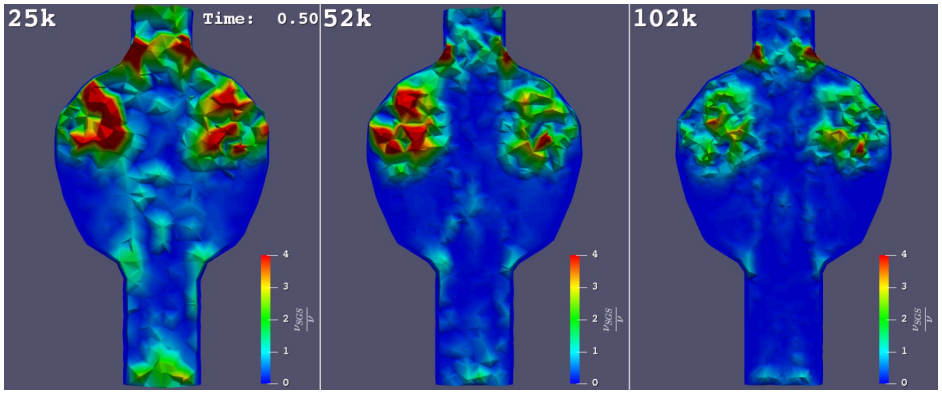

(c) Diastolic peak.

Figure 5.35: Turbulent viscosity, $\frac{\nu_{sgs}}{\nu}$, in the middle plane at the Systole (a), Mid deceleration point (b), and Diastole (c), for different mesh refinements ($25k$, $52k$, $102k$).

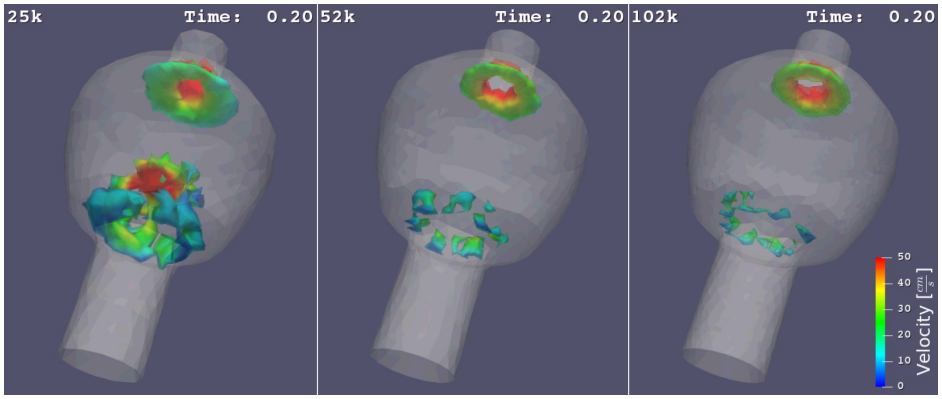

(a) Systolic peak.

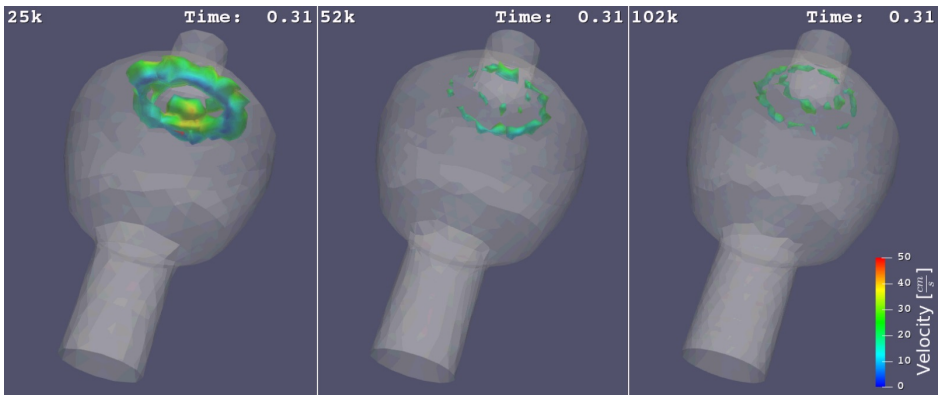

(b) Mid deceleration point.

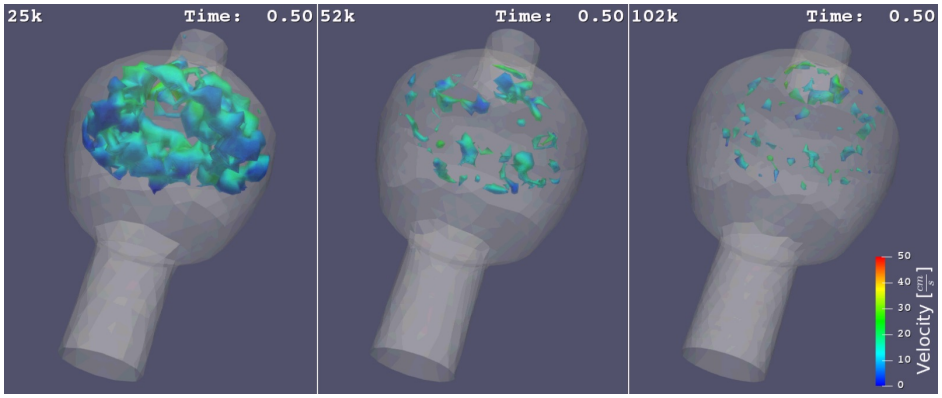

(c) Diastolic peak.

Figure 5.36: Turbulent viscosity iso-surface, $\frac{\nu_{sgs}}{\nu} \geq 4$, at the Systole (a), Mid deceleration point (b), and Diastole (c), for different mesh refinements ($25k$, $52k$, $102k$).

Conclusion

In this thesis, Large Eddy Simulation σ-models (static and dynamic) have been used to study the transition to turbulence in Abdominal Aortic Aneurysms.

During the work of this thesis we implemented in `LIFEV` a complete version of SUPG-PSPG able to show less numerical dissipation with respect to the steady old version. This new version will help future numerical studies.

We compared the LES simulations with a reference solution obtained at high resolution without any turbulent model, that we called DNS. The considered LES models are capable to turn on in regions where the instabilities and fluctuations occur, i.e. at the mid-deceleration and diastolic phases. The main differences between LES simulations and the DNS one are shown to be during mid-deceleration and diastolic phases. These discrepancies are probably caused by transitional effects during these phases that we found are incorporated in the turbulence viscosity of LES models.

The static-σ and the dynamic-σ simulations shows very similar features in any quantity we have analyzed. Some minimal differences are found to be in the diastolic phase. This is probably, but not only, due to the fact that the dynamic σ-model is able to reproduce the backscatter phenomena. In fact, the backscatter percentage of the Dynamic-σ is about the 45%.

Turbulent transitional effects were studied by computing the ensemble average of the velocity magnitude, the *Q-criterion*, evaluating the global kinetic energy, and the Time Average Wall Shear Stress. Also for these quantities of interest there are marked differences around the diastolic phase. However, these differences seem to have a limited impact on the TAWSS.

We studied where and when turbulent viscosity in static σ-model evolves inside the AAA geometry measuring the ratio between the subgrid-scale viscosity and the molecular one. From this analysis we found that LES models are active in particular during the mid deceleration and early diastolic phase, with the turbulent viscosity reaching values up five time greater than those of molecular one.

The results demonstrate the suitability of the considered LES σ-models to describe turbulent transitional effects in the AAA.

Achievements

The achievements of this thesis are summarized in what follows:

1. we implemented in `LIFEV` a complete version of SUPG-PSPG able to shows less numerical dissipation with respect to the steady old version;

2. we studied the contribution of LES σ models in describing the fluid dynamics inside a patient specific AAA. The main differences with respect to a DNS simulation are shown to be during mid-deceleration and diastolic phases;

3. we built an high resolution reference solution based on a simplified shear layer 2D model to estimate the grid size and time discretization parameter needed to capture all the important features of the fluid flow in a AAA. We referred to this simulation as DNS;

4. we post-process the obtained numerical solutions to asses hemodynamic significant quantities, such as TAWSS and vortical structures enduced via the *Q-criterion*;

5. we studied where and when turbulent viscosity in static σ-model evolves inside the AAA geometry measuring the ratio between the subgrid-scale viscosity and the molecular one.

Possible future improvements

Many improvements can be made in future works. In particular:

- We made the assumption of *rigid walls* which represents a first limitation of the present work. Indeed flexible walls could affect the velocity fluctuations and WSS values. Thus, a Fluid-Structure Interaction simulation with LES turbulent model could increase the accuracy of the results presented in this thesis.

- Another approximation introduced is related to the boundary conditions. In absence of measures, we prescribed a parabolic velocity profile with a representative flow rate at the inlet, whereas zero stresses are set at the iliac outlets. These boundaries conditions do not take into account the rest of the cardiovascular system. Hence, the prescription of patient-specific velocity data could provide more accurate results.

- As we have seen, for most of the ensemble average quantities evaluated, six heartbeats are not enough to remove most of the fluctuations, and to capture the average trends. We need to perform many more heartbeats in order to access at smooth average trends.

- In order to further validate the suitability of LES σ-models we can compare these models with other LES approaches, like the Variational Multiscale Large Eddy Simulation (VMS-LES) [61].

List of Figures

List of Tables

Bibliography

[1] S.B. Pope. *Turbulent flows*. Cambridge University Press, 2000.

[2] L. F. Richardson. *Weather prediction by numerical process*. Cambridge University Press, 2007.

[3] K. Sreenivasan, & C. Meneveau, *The fractal facets of turbulence*. Journal of Fluid Mechanics, 173, 357-386, 1986.

[4] L. Valdettato. *Dispense del corso di Teoria, Modellistica e Simulazione della Turbolenza*. A.A. 2007/08 `http://www1.mate.polimi.it/didattica/turbolenza/dispense.html`.

[5] U. Frisch. *Turbulence: the legacy of A.N. Kolmogorov*. Cambridge University Press, 2000.

[6] B.E. Launder D.B. Spalding. *Mathematical models of turbulence*. Academic Press, London, 1972.

[7] P. Sagaut. *Large Eddy Simulation for Incompressible Flows*. Springer, 2006.

[8] S. Z. Zhao, X. Y. Xu, A. D. Hughes, S. A. Thom, A. V. Stanton, B. Ariff, and Q. Long. *Blood flow and vessel mechanics in a physiologically realistic model of a human carotid arterial bifurcation*. Journal of Biomechanics, 33(8):975–984,8 2000.

[9] R. Berne and M. Levy. *Cardiovascular Physiology*. 1997.

[10] L. Formaggia, A. Quarteroni, and A. Veneziani, *Cardiovascular Mathematics - Modeling and simulation of the circulatory system*. Springer-Verlag Milan, 2009.

[11] A. Porpora, P. Zunino, C. Vergara, and M. Piccinelli, *Numerical treatment of boundary conditions to replace lateral branches in hemodynamics*.

International Journal for Numerical Methods in Biomedical Engineering, 28: 1165-1183, 2012.

[12] W. E. Stehbens. *Turbulence of blood flow*. Quarterly journal of experimental physiology and cognate medical sciences, 44(1):110–117, 1959.

[13] P. F. Davies, A. Remuzzi, E. J. Gordon, C. F. Dewey, and M. A. Gimbrone. *Turbulent fluid shear-stress induces vascular endothelial-cell turnover invitro*. Proceedings of the National Academy of Sciences of the United States of America, 83(7):2114–2117, 1986.

[14] M. J. O'Rourke, J. P. McCullough, and S. Kelly. *An investigation of the relationship between hemodynamics and thrombus deposition within patientspecific models of abdominal aortic aneurysm*. Proceedings of the Institution of Mechanical Engineers, Part H: Journal of Engineering in Medicine, 226(7):548–564, 2012.

[15] D. Birchall, A. Zaman, J. Hacker, G. Davies, and D. Mendelow. *Analysis of haemodynamic disturbance in the atherosclerotic carotid artery using computational fluid dynamics*. European Radiology, 16(5):1074–1083, 2006.

[16] F. Ghalichi and X. Deng. *Turbulence detection in a stenosed artery bifurcation by numerical simulation of pulsatile blood flow using the low-Reynolds number turbulence model*. Biorheology, 40(6):637–654, 2003.

[17] RM Lancellotti, C. Vergara, L. Valdettaro, S. Bose, A. Quarteroni *Large eddy simulations for blood dynamics in realistic stenotic carotids*. International Journal for Numerical Methods in Biomedical Engineering; 33:e2868, 2017.

[18] G.G. Ferguson. *Turbulence in human intracranial saccular aneurysms*. Journal of Neurosurgery, 33(5):485–497, 1970.

[19] G.R. Jr Upchurch K.M. Khanafer, J.L. Bull and R. Berguer. *Turbulence significantly increases pressure and fluid shear stress in an aortic aneurysm model under resting and exercise flow conditions*. Annals of Vascular Surgery, 21(1):67–74, 2007.

[20] C. Vergara, D. Le Van, M. Quadrio, L. Formaggia, M.Domain, *Large eddy simulations of blood dynamics in abdominal aortic aneurysms*. Medical Engineering and Physics , Volume 47 , 38 - 46, 2017.

[21] B.C. Brott Y. Ito C.H. Cheng A.M. Shih M. Allon S. Unnikrishnan, T.N. Huynh and A.S. Anayiotos. *Turbulent flow evaluation of the venous needle during hemodialysis.* Journal of Biomechanical Engineering, 7(5):1141–1146, 2005.

[22] X. Teng, B.C. Brott, M. Allon, S.S. Kelpke, J.A. Thompson, R.P. Patel, T.N. Huynh, B.K. Chacko and A.S. Anayiotos, *Effects of venous needle turbulence during ex vivo hemodialysis on endothelial morphology and nitric oxide formation.* Journal of Biomechanical Engineering, 40(10):2158–2166, 2006.

[23] P.D. Stein and N.H. Sabbah. *Turbulent blood flow in the ascending aorta of humans with normal and diseased aortic valves.* Circulation Research, 39(1):58–65, 1976.

[24] W.A. Seed, R. Torii, D. O'Regan, C.A. Kousera, N.B.Wood, and X.Y. Xu, *A numerical study of aortic flow stability and comparison with in vivo flow measurements.* Journal of Biomedical Engineering, 135(011003):1–9, 2013.

[25] J. Zajac, J. Eriksson, P. Dyverfeldt, A.F. Bolger, T. Ebbers,and C. Carlhäll, *Turbulent kinetic energy in normal and myopathic left ventricles.* Journal of Magnetic Resonance Imaging, 41: 1021-1029, 2015

[26] C. Chnafa, S. Mendez, and F. Nicoud. *Image-based large-eddy simulation in a realistic left heart.* Computers & Fluids, 94:173–178, 2014.

[27] V. Gravemeier, A. Comerford, and W.A. Wall. *An algebraic variational multiscale-multigrid method for large-eddy simulation of turbulent pulsatile flows in complex geometries with detailed insight into pulmonary airway flow.* International Journal for Numerical Methods in Fluids, 71(10):1207–1225, 2013.

[28] J. Kim, P. Moin, R. Moser *Turbulence statistics in fully developed channel flow at low Reynolds number.*Journal of Fluid Mechanics; 177:133–66, 1987.

[29] R.D. Moser, J. Kim, N.N. Mansour *Direct numerical simulations of turbulent channel flow up to* $Re_\tau = 590$. Physics Fluids 11:943–5, 1999.

[30] F. Nicoud, F. Ducros *Subgrid-scale modelling based on the square of the velocity gradient tensor.* Flow, Turbulence and Combustion; 62:183–200, 1999

[31] J. Deardorff, *A numerical study of three-dimensional turbulent channel flow at large Reynolds numbers*, Journal of Fluid Mechanics, vol. 41, pp. 453–465, 1970.

[32] R.S. Rogallo and P. Moin. *Numerical Simulation of Turbulent Flows*. Annual Review of Fluid Mechanics, 16:99–137, 1984.

[33] K. Horiuti. *Alignment of eigenvectors for strain rate and subgrid-scale stress tensors*. Direct and large-eddy simulation IV, Geurts, Friedrich and Mactais eds.), Kluwer, 2001.

[34] B. Tao J. Katz C. Meneveau. *Geometry and scale relationships in high reynolds number turbulence determined from three-dimensional holographic velocimetry*. Physics Fluids, 12(5):941–944, 2000.

[35] B. Tao J. Katz C. Meneveau. *Statistical geometry of subgrid-scale stresses determined from holographic piv measurements*. Journal of Fluid Mechanics, 457:35–78, 2002.

[36] J. Smagorinsky, *General circulation experiments with the primitive equations: I. The basic experiment*, Monthly weather review, vol. 91, pp. 99–164, 1963.

[37] R.A. Clark J.H. Ferziger W.C. Reynolds. *Evaluation of subgrid-scale models using an accurately simulated turbulent flow*. Journal of Fluid Mechanics, 91(1):1–16, 1979.

[38] F. Nicoud, H. B. Toda, O. Cabrit, S. Bose, and J. Lee, *Using singular values to build a subgrid-scale model for large eddy simulations*, Physics of Fluids, vol. 23, no. 8, p. 085106, 2011.

[39] M. Germano, U. Piomelli, P. Moin, and W. Cabot, *A dynamic subgrid-scale eddy viscosity model*, Physics of Fluids A, vol. 3, no. 7, pp. 1760–1765, 1991.

[40] G. Wollenek G. Maurer H. Baumgartner D. Bonderman, E. Gharehbaghu-Schnell and I. M. Lang. *Mechanisms underlying aortic dilatation in congenital aortic valve malformation*. Circulation, 99:2138–2143, 1999.

[41] S. T. Bose D. You and P. Moin. *Grid-independent large-eddy simulation of compressible turbulent flows using explicit filtering*. Proceedings of the Summer Program - Center for Turbulence Research, pages 203–210, 2010.

[42] A. De Champlain Y. Douville M. King F. Ghalichi, X. Deng and R. Guidoin. *Low Reynolds number turbulence modeling of blood flow in arterial stenoses*. Biorheology, 35(4,5):281–294, 1998.

[43] E. Falk. *Pathogenesis of atherosclerosis*. Journal of American College of Cardiology, 47(8):C7–12, 2006.

[44] E. S. D. Martino, A. Bohra, J. P. V. Geest, N. Gupta, M. S. Makaroun, and D. A. Vorp. *Biomechanical properties of ruptured versus electively repaired abdominal aortic aneurysm wall tissue*. Journal of Vascular Surgery, 43(3):570–576, 2006.

[45] M. Germano, *Turbulence: the filtering approach*, Journal of Fluid Mechanics, vol. 238, pp. 325–336, 1992.

[46] D. Lilly, *A proposed modification of the Germano subgrid-scale closure method,*, Physics of Fluids A, vol. 4, no. 3, pp. 633–635, 1992.

[47] Y. Zang, R.L. Street, and J.R. Koseff. *A dynamic mixed subgrid-scale model and its application to turbulent recirculating flows*. Physics of Fluids A, 5(12):3186–3196, 1993.

[48] P. H. B. Toda, *LES modeling and experimental study of wall-bounded flows in complex geometries*. PhD thesis, Universite Montpellier II, 2011.

[49] A. Quarteroni, *Modellistica numerica per problemi differenziali* 6ed Springer, 2016.

[50] F. Brezzi and M. Fortin. *Mixed and hybrid finite element methods*. Springer Verlag, 1991.

[51] T. E. Tezduyar. *Stabilized finite-element formulations for incompressible-flow computations*. Advances in Applied Mechanics, Vol 28, 28:1–44, 1992.

[52] L. Tobiska and G. Lube. *A modified streamline-diffusion method for solving the stationary navier-stokes equations*. Numer. Math., 59:13–29, 1991.

[53] E. Hairer, S.P. Norsett, and G. Wanner. *Solving ordinary differential equations: Nonstiff problems*. Springer Series in Comput. Math. Springer, 1993.

[54] A. Quarteroni, R. Sacco, and F. Saleri. *Numerical mathematics*. Springer Berlin, 2000.

[55] Quarteroni A., Manzoni A., and Vergara C. *The cardiovascular system: Mathematical modeling, numerical algorithms, clinical applications*. mox-report no. 38/2016.

[56] W. Gropp, B. Smith, P. Bjorstad, *Domain decomposition: Parallel multilevel methods for elliptic partial differential equations*. Computers & Mathematics with Applications, 33(4):132, feb 1997.

[57] S.Stella, *Computational study of the influence of the pressure guide wire on the coronary pressure*, master degree Thesis, Università degli studi di Trento, dipartimento di Matematica 2017.

[58] A. Quarteroni and A. Valli, *Numerical approximation of partial differential equations*. Springer, 1994.

[59] V. Johm and W. Layton, *Analysis of numerical errors in large eddy simulation*, SIAM Journal on Numerical Analysis, vol. 40(3), pp. 995–1020, 2002.

[60] A.N. Brooks and T.J.R. Hughes. *Streamline upwind / Petrov-Galerkin formulations for convection dominated flows with particular emphasis on the incompressible Navier-Stokes equation*. Cmame, 32:199–259, 1982.

[61] D. Forti, L. Dedè, *Semi-implicit BDF time discretization of the Navier–Stokes equations with VMS-LES modeling in a High Performance Computing framework*, Computers & Fluids 117, p. 168-182, 2015.

[62] T.E. Tezduyar, S. Mittal, S.E. Ray, and R. Shih. *Incompressible flow computations with stabilized bilinear and linear equal-order-interpolation velocity-pressure elements*. Cmame, 95:221–242, 1992.

[63] A.E. Tejada-Martinez and K. E. Jansen. *On the interaction between dynamic model dissipation and numerical dissipation due to streamline upwind/petrov-galerkin stabilization*. Computer Methods in Applied Mechanics and Engineering, 194:1225–1248, 2005.

[64] T. Tezduyar and S. Sathe *Stabilization parameters in SUPG and PSPG formulations* Journal of Computational and Applied Mechanics, Vol. 4., No. 1., pp. 71–88, 2003.

[65] K. Jansen, *A stabilized finite element method for computing turbulence*, Computer Methods in Applied Mechanics and Engineering, vol. 174, pp. 299–317, 1999.

[66] M. E. Moghadam, Y. Bazilevs, T.-Y. Hsia, I. E. Vignon-Clementel, A. L. Marsden, and M. C. H. Allianc. *A comparison of outlet boundary treatments for prevention of backflow divergence with relevance to blood flow simulations*. Computational Mechanics, 48(3):277–291, 2011.

[67] C. Bertoglio and A. Caiazzo. *A tangential regularization method for backflow stabilization in hemodynamics*. Journal of Computational Physics, 261:162–171, 2014.

[68] C. Bertoglio and A. Caiazzo. *A Stokes-residual backflow stabilization method applied tophysiological flows*. Journal of Computational Physics, 313:260–278, 2016.

[69] D. Le Van *Fluid Dynamics in an Abdominal Aortic Aneurysm with Large Eddy Simulation and Backflow Stabilization*, master degree Thesis, Politecnico di Milano, Scuola di Ingegneria Industriale e dell'Informazione, Corso di Laurea Magistrale in Ingegneria Aeronautica, 2016.

[70] M. Ismail, V. Gravemeier, A. Comerford, and W. A. Wall. *A stable approach for coupling multidimensional cardiovascular and pulmonary networks based on a novel pressure-flow rate or pressure-only Neumann boundary condition formulation*. International Journal for Numerical Methods in Biomedical Engineering, 30(4):447–469, 2014.

[71] V. Gravemeier, A. Comerford, L. Yoshihara, M. Ismail, and W. A. Wall. *A novel formulation for Neumann inflow boundary conditions in biomechanics*. International Journal for Numerical Methods in Biomedical Engineering, 28(5):560–573, 2012.

[72] A. Veneziani, C. Vergara, *Flow rate defective boundary conditions in haemodynamics simulations*. International Journal for Numerical Methods in Fluids, 47: 803-816, 2005.

[73] I. Campbell, J. Ries, S. Dhawan, A. Quyyumi, W. Taylor, and J. Oshinski, *Effect of inlet velocity profiles on patient-specific computational fluid dynamics simulations of the carotid bifurcation*, Journal of Biomechanical Engineering, vol. 134(5), p. 051001, 2012.

[74] M. Piccinelli, C. Vergara, L. Antiga, L. Forzenigo, P. Biondetti, and M. Domanin. *Impact of hemodynamics on lumen boundary displacements in abdominal aortic aneurysms by means of dynamic computed tomography and computational fluid dynamics*. Biomechanics and Modeling in Mechanobiology, 12(6):1263–1276, 2013.

[75] A. S. Les, J. J. Yeung, G. M. Schultz, R. J. Herfkens, R. L. Dalman, and C. A. Taylor. *Supraceliac and infrarenal aortic flow in patients with abdominal aortic aneurysms: mean flows, waveforms, and allometric scaling relationships*. Cardiovascular engineering and technology, 1(1):39–51, 2010.

[76] L. Antiga and D. Steinman. *The vascular modeling toolkit*. `http://www.vmtk.org`.

[77] R. Betchov and A. Szewczyk, *Stability of a shear layer between parallel streams*, Physics of Fluids, vol. 6, no. 10, pp. 1391–1396, 1963.

[78] H. Schlichting, *Boundary Layer Theory*, McGraw-Hill Book Company, Inc., New York, 1963.

[79] R.M. Lancellotti, *Large eddy simulations in haemodyncamics: models and applications*, Politecnico di Milano department of Mathematics PhD Thesis, 2015.

[80] Z. SongNian, H. Fei. *Turbulence question: How do view "the homogenous and isotropic turbulence?*. Sci Sin-Phys Mech Astron, 45(2): 24701-024701, 2015

[81] D. Hatziavramidis, H. Ku, *Solutions of the two-dimensional navier-stokes equations by chebyshev expansion methods*. Computers & Flu- ids, 13:99-113, 1985.

[82] J. M. Paulus. *Platelet size in man*. Blood, 46(3):321–336, 1975.

[83] R. I. Handin, S. E. Lux, and T. P. Stossel. *Blood: principles and practice of hematology*, volume 1. Lippincott Williams & Wilkins, 2003.

[84] M. L. Turgeon. *Clinical hematology: theory and procedures*. Lippincott Williams & Wilkins, 2005.

[85] K. Perktold and D. Hilbert. *Numerical simulation of pulsatile flow in a carotid bifurcation model*. Journal of biomedical engineering, 8(3):193–199, 1986.

[86] J Chen, X-Y Lu, and W Wang. *Non-newtonian effects of blood flow on hemodynamics in distal vascular graft anastomoses*. Journal of Biomechanics, 39:1983–1995, 2006.

[87] K. W. Johnston, R. B. Rutherford, M. D. Tilson, D. M. Shah, L. Hollier, and J. C. Stanley. *Suggested standards for reporting on arterial aneurysms.* Journal of Vascular Surgery, 13(3):452–458, 1991.

[88] J. C. Lasheras. *The biomechanics of arterial aneurysms*, volume 39 of Annual Review of Fluid Mechanics, 2007.

[89] C. Fleming, E. Whitlock, T. Beil, F. Lederle. *Screening for abdominal aortic aneurysm: a best-evidence systematic review for the U.S. preventive services task force.*Annals of Internal Medicine;142(3):203–11, 2005.

[90] E. Bagci, Y. Vodovotz, T. Billiar, B. Ermentrout, I. Bahar *Computational insights on the competing effects of nitric oxide in regulating apoptosis.* PLOS One;3(5):e2249, 2008.

[91] C. Asbury, J. Ruberti, F. Bluth, R. Peattie. *Experimental investigation of steady flow in rigid models of abdominal aortic aneurysms.* Annals of Biomedical Engineering;23(1):29–39, 1995.

[92] A. Les, S. Shadden, C. Figueroa, J. Park, M. Tedesco, R. Herfkens, et al. *Quantification of hemodynamics in abdominal aortic aneurysms during rest and exercise using magnetic resonance imaging and computational fluid dynamics.* Annals of Biomedical Engineering;38(4):1288–313, 2010.

[93] R. C. Darling, C. R. Messina, D. C. Brewster, and L. W. Ottinger. *Autopsy study of unoperated abdominal aortic aneurysms. the case for early resection.* Circulation, 56(3 Suppl):161–164, 1977.

[94] K. Singh, K. H. Bonaa, B. K. Jacobsen, L. Bjork, and S. Solberg. *Prevalence of and risk factors for abdominal aortic aneurysms in a population-based study: the tromso study.* American Journal of Epidemiology, 154(3):236–244, 2001.

[95] D. Mozaffarian, E.J. Benjamin, A.S. Go, D.K. Arnett, M.J. Blaha, M. Cushman, S.R. Das, S. de Ferranti, J.-P. Despr´es, H.J. Fullerton, V.J. Howard, M.D. Huffman, C.R. Isasi, M.C. Jim´enez, S.E. Judd, B.M. Kissela, J.H. Lichtman, L.D. Lisabeth, S. Liu, R.H.Mackey, D.J.Magid, D.K.McGuire, E.R.Mohler, C.S.Moy, P.Muntner, M.E. Mussolino, K. Nasir, R.W. Neumar, G. Nichol, L. Palaniappan, D.K. Pandey, M.J. Reeves, C.J. Rodriguez, W. Rosamond, P.D. Sorlie, J. Stein, A. Towfighi, T.N. Turan, S.S. Virani, D. Woo, R.W. Yeh, and M.B. Turner. *Heart disease and stroke statistics—2016 update.* Circulation, 132, 2015.

[96] E. Choke, G. Cockerill, W.R.W Wilson, S. Sayed, J. Dawson, I. Loftus, M.M. Thompson, *A review of biological factors implicated in abdominal aortic aneurysm rupture*. European Journal of Vascular and Endovascular Surgery 30, 227–244, 2005.

[97] F.A. Lederle, G.R. Johnson, S.E. Wilson, *Aneurysm Detection and Management Veterans Affairs Cooperative Study: abdominal aortic aneurysm in women*. Journal of Vascular Surgery 34, 122–126, 2001.

[98] F.A. Lederle, G.R. Johnson, S.E. Wilson, E.P. Chute, F.N. Littooy, D. Bandyk, W.C. Krupski, G.W. Barone, C.W. Acher, D.J. Ballard, *Prevalence and associations of abdominal aortic aneurysm detected through screening. Aneurysm Detection and Management (ADAM) Veterans Affairs Cooperative Study Group*. Annals of Internal Medicine 126, 441–449. 1997.

[99] E. Bluth, S. Murphey, L. Hollier, M. Sullivan, *Color flow doppler in the evaluation of aortic aneurysms*. International Angiology; 9(1):8–10, 1990.

[100] T. Yip, S. Yu, *Cyclic transition to turbulence in rigid abdominal aortic aneurysm models*. Fluid Dynamics Research ;29(2):81–113, 2001.

[101] T. Fukushima, T. Matsuzawa, T. Homma, *Cyclic transition to turbulence in rigid abdominal aortic aneurysm models*. Biorheology;26(2):109–30, 1988.

[102] R. Peattie, T. Riehle, F. Bluth, *Pulsatile flow in fusiform models of abdominal aortic aneurysms: flow fields, velocity patterns and flow-induced wall stresses*. Journal of Biomechanical Engineering; 126(4):438–46, 2004.

[103] D. Giddens, C. Zarins, S. Glagov, *Response of arteries to near-wall fluid dynamic behavior*. Applied Mechanics Reviews 1990;43(5S):S98–S102, 1990.

[104] C. J. Egelhoff, R. S. Budwig, D. F. Elger, T. A. Khraishi, and K. H. Johansen. *Model studies of the flow in abdominal aortic aneurysms during resting and exercise conditions*. Journal of Biomechanics, 32(12):1319–1329, 1999.

[105] A. Abbà, C. Cercignani, and L. Valdettaro. *Analysis of subgrid scale models*. Computers and Mathematics with applications, 46:521–535, 2003.

Ringraziamenti

Si conclude oggi questo nuovo capitolo della mia vita iniziato due anni e mezzo fa. Molte cose sono cambiate e molte sono sicuro che cambieranno nei prossimi mesi.

Desidero ringraziare i Professori Luca Dedè, Lorenzo Valdettaro e Christian Vergara per avermi dato l'opportunità di lavorare su questo splendido progetto. Vi ringrazio per avermi dato sempre degli ottimi consigli nei momenti di difficoltà, che si sono presentati, e per avermi spronato ad andare avanti nel lavoro di tesi, sempre con molta calma e pazienza. Siete stati molto disponibili e, nonostante i vostri innumerevoli impegni lavorativi, mi avete concesso sempre un po' del vostro tempo, quando se ne presentava il bisogno.

Un ringraziamento particolare va al Dottor Simone Stella per i pomeriggi passati insieme a lavorare sul codice. Spero che il futuro ci permetta di collaborare di nuovo insieme.

Desidero ringraziare, inoltre, il Professore Sebastiano Bernuzzi. Sicuramente questa "passione" per le equazioni di Navier-Stokes è venuta fuori dalla tesina che ho svolto a fine del suo corso di Fisica Computazionale.

Grazie alla Professoressa Alessandra Aimi e al Professor Mauro Diligenti, per avermi concesso fin da subito la vostra fiducia. E' passato ormai più di un anno dal nostro primo incontro. Da quella chiacchierata mi avete aiutato a capire cosa c'era nel mio futuro (che al tempo, era ancora molto nebuloso). Grazie ai vostri preziosi consigli, mi sono ritrovato su un "treno" diretto a Milano. Ad aspettarmi al MOX quel giorno c'era il Professor Lorenzo Valdettaro. Da lì è iniziata la mia storia.

Desiro ringraziare la Professoressa Laura Romanò per il tempo che mi ha dedicato e per avermi dato la possibilità di partecipare attivamente durante la due Notti dei Ricercatori a Parma.

Grazie ai ragazzi di Fisica che hanno condiviso con me una parte di questo percorso di studi: Emidio, Marco, Paolo, Frank, Alberto, Davide e Gorro.

Una menzione particolare va all'Inzani Volley Parma in cui ho trascorso tre stagioni sportive. Siete stati e siete per me come una seconda Famiglia.

Speriamo che questa "ultima" annata si possa concludere nel migliore dei modi possibili.

La lontananza da casa mi ha fatto apprezzare l'unica cosa che credo non cambierà mai nella mia vita: l'affetto della mia Famiglia e in particolar modo dei miei genitori e di mio fratello Mirko. Grazie di essere sempre stati presenti nella mia vita, anche quando le cose non andavano. "Non possiamo connettere i punti della nostra vita guardando in avanti, possiamo solo collegarli guardando indietro". Voi mi avete sempre aiutato con fiducia a credere che i punti in qualche modo si sarebbero connessi lungo la strada del mio tortuoso percorso. Se ripenso alle scelte fatte, molte sbagliate e poche giuste probabilmente, voi siete state le uniche persone che mi sono sempre state accanto. Molte cose sono quantificabili in natura. Tuttavia, l'affetto e l'amore per la Famiglia non credo si possano quantificare o spiegare a parole, ma possono essere solo vissute e assaporate ogni giorno della nostra vita.